Infrared Time-Correlated Single-Photon Counting

Ryan Ellis Warburton

Thesis submitted for the Degree of Doctor of Philosophy

Heriot-Watt University

School of Engineering and Physical Sciences

July 2008

Abstract

This Thesis investigates near infrared (λ ~ 1550 nm) time-correlated single-photon counting, studying the single-photon detectors and some of the potential application areas.

Custom designed and fabricated InGaAs/InP single-photon avalanche diode detectors were characterised. Our devices yielded single-photon detection efficiencies of ~10 %, timing jitter of 200 ps, and noise equivalent power comparable to the best commercially available avalanche photodiodes operated in Geiger-mode.

The afterpulsing phenomenon which limits the maximum count rate of InGaAs/InP single-photon avalanche diodes has been investigated in detail and activation energies calculated for the traps that cause this problem. This was found to be ~250 meV for all the devices tested, despite their differing structures and growth conditions, and points to the InP multiplication region as the likely location of the traps.

Ways of reducing the effects caused by the afterpulsing phenomenon were investigated and sub-Geiger mode operation was studied in detail. This approach enabled free-running, afterpulsing-free operation at room temperature of an InGaAs/InP single-photon avalanche diode detector for the first time.

Finally, time-of-flight photon counting laser ranging was performed using both single-photon avalanche diodes and superconducting nanowire single-photon detectors. The use of the latter resulted in a surface to surface depth resolution of 4 mm being achieved at low average laser power at an eye-safe wavelength of 1550 nm.

Acknowledgements

Firstly, I'd like to thank my supervisor, Professor Gerald Buller, for his guidance, support and "witty banter" that made the endless days in a dark lab *almost* bearable! A special thanks goes to the rest of the Photon Counting group member, past and present: Dr. Aongus McCarthy, Dr. Robert Collins, Dr. Karen Gordon, Dr. Phil Hiskett, Dr. Veronica Fernandez, Colin Parry, and in particular Dr. Sara Pellegrini whose supervision, assistance and constant support in and out of the lab has helped me to reach the end of this roller-coaster ride as a PhD student.

Throughout the Physics department there are characters that have either helped in some way, or just kept me amused in the office. This motley selection of people who I'd like to call my friends definitely deserves a mention: Richard Moug, Ian Thomson, Spyros Brown, Keith Serrels, Rainer Beck, Derek Bilsland, Dr. Craig Moir and the crèche-office scapegoat Dr. Kevin Cook. I'd also like to thank Dr. Catherine McMillan for the email conversations and her constant encouragement.

Thanks also go out to the various collaborators with whom I have worked: Dr. Mark Itzler from Princeton Lightwave Inc., Dr. Robert Hadfield & Dr. Sae Woo Nam from NIST, Professor John David & Dr. Jo Shien Ng and the rest of the group at the Centre for III-V Technologies at the University of Sheffield.

I'd like to thank my friends out-with the University to prove there is life out there; beyond the 3am finishes, the dark lab and the endless hours of typing, namely: David Amos, Pablo (the Mexican) Zervas, Matt Edwards & Mike Pinkerton of Karnival fame, and Chris Sprought.

Finally, and most importantly, I owe everything to the three people I love the most; my parents for always believing in me and their constant encouragement and, last but certainly not least, Hayley for putting up with me and spurring me on through all this.

Table of Contents

List of Journal Publications by the Candidate

S. Pellegrini, **R.E. Warburton**, L.J.J. Tan, J.S. Ng, A. Krysa, K. Groom, J.P.R. David, S. Cova, M. J. Robertson, and G.S. Buller, *Design and performance of an InGaAs/InP single-photon avalanche diode detector,* IEEE Journal of Quantum Electronics, **42** (4), 397 - 403 (2006)

A.M. Wallace, R. Sung, G.S. Buller, R.D. Harkins, **R.E. Warburton** and R.A. Lamb, *Detecting and characterising returns in a multi-spectral pulsed lidar system*, IEE Proceedings - Vision, Image and Signal Processing, **153** (2), 160 - 172 (2006)

J.A. Timpson, S. Lam, D. Sanvitto, D.M. Whittaker, H. Vink, A. Daraei, P.S.S. Guimareraes, M.S. Skolnick, A.M. Fox, C. Hu, Y-L. D. Ho, R. Gibson, J.G. Rarity, A. Tahraoui, M. Hopkinson, P.W. Fry, S. Pellegrini, K.J. Gordon, **R.E. Warburton**, G.S. Buller, A. Tahraoui, P.W. Fry, and M. Hopkinson, *Single photon sources based upon single quantum dots in semiconductor microcavity pillars*, Journal of Modern Optics, **54** (2 – 3), 453 – 465 (2007)

R.E. Warburton, A. McCarthy, A.M. Wallace, S. Hernandez-Marin, S. Cova, R.A. Lamb, and Gerald S. Buller, *Enhanced Performance Photon-Counting Time-of-Flight Sensor*, Optics Express **15** (2), 423 – 429 (2007)

G.S. Buller, S. Pellegrini, **R.E. Warburton**, L.J.J. Tan, J.S. Ng, A. Krysa, K. Groom, J.P.R. David and S. Cova, *Single-Photon Detection in Quantum Key Distribution*, INVITED PAPER to IEEE-LEOS Newsletter (Oct 2006)

R.E. Warburton, A. McCarthy, A.M. Wallace, S. Hernandez-Marin, R.H. Hadfield, S.W. Nam, and G.S. Buller, *Subcentimeter depth resolution using a single-photon counting time-of-flight laser ranging system at 1550 nm wavelength*, Optics Letters **32** (15), 2266 - 2268 (2007)

G.S. Buller, **R.E. Warburton**, S. Pellegrini, J.S. Ng, J.P.R. David, L.J.J. Tan, A.B. Krysa, and S. Cova, *Single-Photon Avalanche Diode Detectors for Quantum Key Distribution*, INVITED PAPER to IET Optoelectronics Special Issue, **1**, 249 - 254 (2007)

Chapter 1 - Introduction

Time-correlated single-photon counting is a well established statistical sampling technique for measuring weak and fast optical signals. It has been employed in numerous applications such as quantum key distribution (QKD) [1] [2], time-resolved photoluminescence (TRPL) [3] and fluorescence [4], laser ranging (LIDAR) and imaging [5] [6], and optical time domain reflectometry (OTDR) [7].

The increase in interest in these applications, and in particular QKD, has placed an emphasis on an increasing need for single-photon detectors. In the visible range, silicon single-photon avalanche diodes (SPADs) are the favoured choice due to their high single-photon detection efficiency (SPDE), low dark count rate (DCR), low afterpulsing and high maximum count rates. Beyond the Si cut-off (wavelength ~ 1 μm) the situation is not so favourable. To accomplish single-photon detection in a semiconductor structure, a material with a narrow bandgap must be used. InGaAs is most commonly used as the absorber (in both SPADs and photomultiplier tubes alike). Inherently, the number of thermally generated carriers present in a narrow bandgap material compared to Si results in a much higher DCR. Normally, InGaAs detectors are cooled for this reason in order to try and attain a DCR similar to that afforded by Si SPADs.

Near infrared single-photon detection is of interest since, although QKD can be accomplished at shorter wavelengths compatible with Si SPADs [2], it is preferable to work in the low attenuation windows of standard optical fibres – 1.3 μm & 1.55 μm. Also, applications such a laser ranging benefit from decreased attenuation through air as well as less solar background radiation at these wavelengths.

This thesis investigates infrared time-correlated single-photon counting (TCSPC) and its applications:

Chapter 2 details the TCSPC technique along with a full review of the current state of single-photon detectors, at both visible wavelengths and near infrared.

Chapter 3 reviews some of the previous work accomplished on InGaAs/InP SPADs and commercial APDs operated in Geiger mode. SPDE, DCR, noise equivalent power (NEP), and photon-timing jitter are reported as the key figures of merit for single-photon detectors. Results of the characterisation of commercially available SPADs

from Princeton Lightwave Inc. are also detailed along with a full comparison between those fabricated within the research programme that funded part of the work reported in this Thesis.

The afterpulsing phenomenon is explained in Chapter 4. The time correlated carrier counting method (TCCCM) is then introduced and its advantages for characterising SPAD afterpulsing described. The TCCCM is used to analyse the full SPAD structure, test structures, and commercial APDs operated in Geiger mode. In the last part of the Chapter, the possible causes for the afterpulsing phenomenon are discussed.

Chapter 5 deals with ways of reducing the effects of the afterpulsing phenomenon including novel gating techniques which reduce the charge flowing through the device. Another method whereby a sub-bandgap wavelength laser is used to ionise the trapped carriers is also presented. Finally, an InGaAs/InP SPAD is utilised in the so-called "sub-Geiger" mode and fully characterised in terms of SPDE, DCR, NEP, timing jitter, afterpulsing, and maximum count rate.

Time-of-flight (TOF) laser ranging is discussed in Chapter 6. Standard methods are presented first including frequency and amplitude modulation, triangulation, and TOF. TOF with photon counting is introduced and a brief history given. A multi-wavelength ranging system is described and is characterised in terms of depth resolution with a standard Si SPAD and again with an improved Si SPAD. Finally, a superconducting nanowire single-photon detector is used with the system to demonstrate single-photon ranging at $\lambda \sim 1550$ nm in daylight.

Chapter 7 summarises the conclusions of each Chapter and reports the possibilities for future work in the fields studied within this Thesis.

1.1 References

[1] C.H. Bennett and G. Brassard, *Quantum cryptography: public key distribution and coin tossing*, Proceedings of the IEEE International Conference on Computers, System, and Signal Processing, Bangalore, India, 175 - 179 (1984)

[2] K.J. Gordon, V. Fernandez, P.D. Townsend, and G.S. Buller, *A Short Wavelength GigaHertz Clocked Fiber–Optic Quantum Key Distribution System*, IEEE Journal of Quantum Electronics, **40** (7), 900 - 908 (2004)

[3] G.S. Buller, S.J. Fancey, J.S. Massa, A.C. Walker, S. Cova, and A. Lacaita, *Time-resolved photoluminescence measurements of InGaAs – InP multiple-quantum-well structures at 1.3 μm wavelengths by use of germanium single-photon avalanche photodiodes*, Applied Optics, **35** (6), 916 - 921 (1996)

[4] B.R. Rae, C. Griffin, J. McKendry, J.M. Girkin, H.X. Zhang, E. Gu, D. Renshaw, E. Charbon, M.D. Dawson, and R.K. Henderson, *CMOS driven micro-pixel LEDs integrated with single photon avalanche diodes for time resolved fluorescence measurements*, Journal of Physics D: Applied Physics, **41** (9), 094011 (2008).

[5] J.S. Massa, A.M. Wallace, G.S. Buller, S.J. Fancey and A.C. Walker, *Laser depth measurement based on time-correlated single photon counting*, Optics Letters, **22** (8), 543 - 545 (1997)

[6] A.M. Wallace, G.S. Buller, and A.C. Walker, *3-D Imaging and ranging by time-correlated single-photon counting*, Computing and Control Engineering Journal, **12** (August), 157 - 168 (2001)

[7] A.L. Lacaita, P.A. Francese, and S. Cova, *Single-photon optical-time domain reflectometer at 1.3 μm with 5 cm resolution and high sensitivity*, Optics Letters, **18** (13), 1110 - 1112 (1993)

Chapter 2 - Time-Correlated Single-Photon Counting: Technique and Review of Single-Photon Detectors

2.1 Introduction

Time-correlated single-photon counting (TCSPC) is a mature statistical sampling technique and is widely used in numerous applications that demand low-light sensitivity and the ability to measure fast optical signals. Although initially used in time-resolved fluorescence and photoluminescence (TRPL) [1] [2], emerging applications such as quantum key distribution (QKD) [3] [4], laser ranging (LIDAR) and imaging [5] [6] [7] [8], and optical time domain reflectometry (OTDR) [9] have driven the need for suitably fast and efficient single-photon detectors for TCSPC. A review of these detectors will be presented in Section 2.3.

2.2 TCSPC technique

The TCSPC method is explained in depth in [10] and [11] although some of the key principles and operating conditions necessary for correct and reliable measurements will be reported herein. The TCSPC technique relies on measuring a sequence of electrical pulses generated by the detection of a stream of single-photons. Each photon in the stream is recorded with respect to its arrival time relative to a fixed reference signal, usually provided by an external clock, as shown in Figure 2.1. In a TCSPC setup, such as that demonstrated in Figure 2.2, these events are often recorded by a photon-counting card which compiles a multitude of these events into histogram form, as demonstrated in Figure 2.3. Practically, this is usually accomplished with a time-to-amplitude converter (TAC) and a multi-channel analyser (MCA) which will be discussed in more detail in Chapter 3.

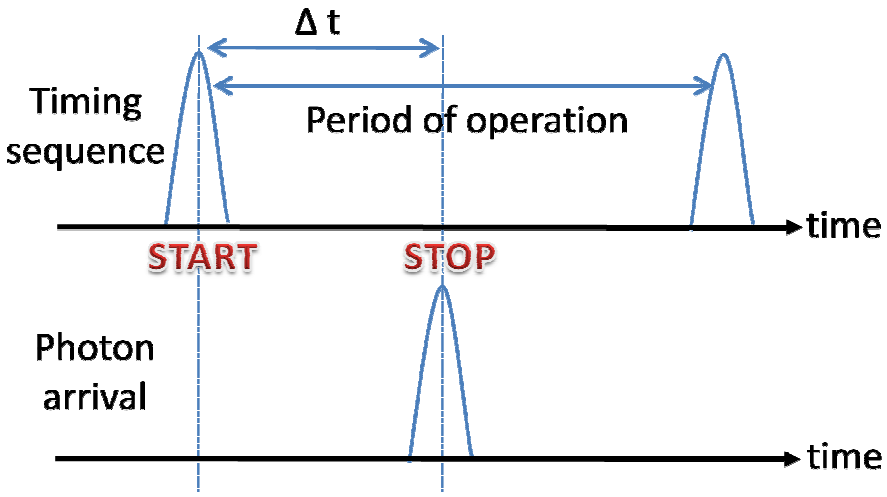

Figure 2.1. Timing sequence for TCSPC operation showing the start signal, usually from an external clock, the stop pulse from the detection of a single-photon and returning to the start after one period of operation. Δt signifies the time difference between start and stop signals.

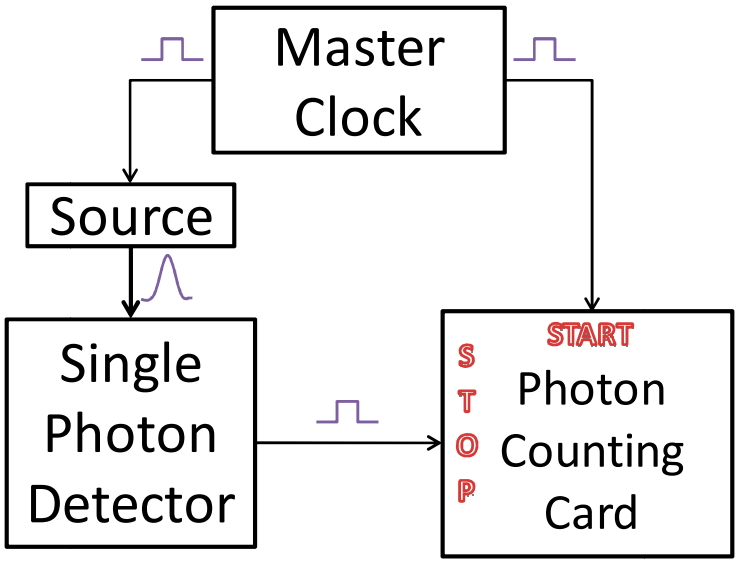

Figure 2.2. A typical TCSPC setup. A master clock sends out a pulse to start the timing process. A synchronous pulse is sent to a laser source and the single-photon stream, which may derive from, for example, photoluminescence or scatter, is detected by a single-photon detector which sends the stop pulse to the single-photon counting apparatus (in this case a PC card the output of which is shown in Figure 2.3).

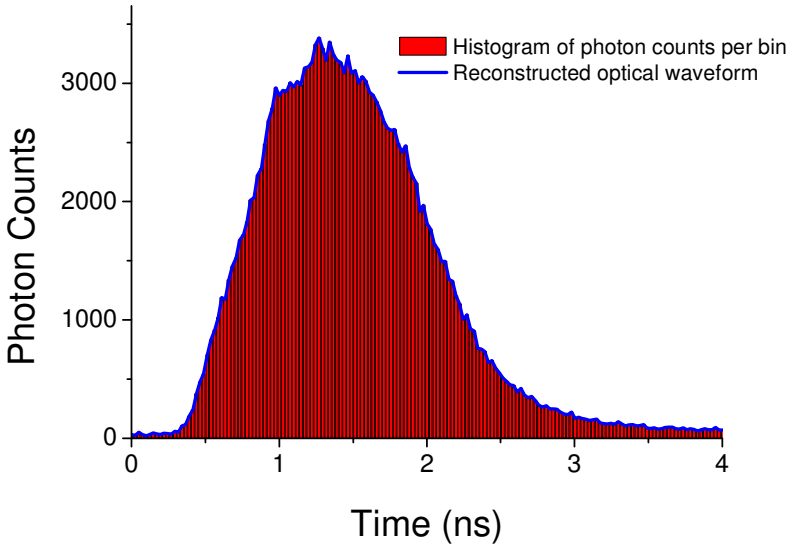

Figure 2.3. Histogram of photon counts recorded according to arrival time. Each time a photon event is measured a count is added to the appropriate time bin.

In Figure 2.3 each histogram bin, or channel, has a discrete width which can be chosen by the user before recording the histogram. Generally, a photon counting card has a set number of channels and a variable timing window duration. Therefore, a short time window will facilitate a narrow bin-width (down to sub-picosecond levels) for high accuracy measurements such as TRPL. A longer window will use wider time bins which may be suited to applications like ranging where several peaks might be evident in a single timing window (relating to different surfaces in the target object).

The accuracy of the time measurement itself is not limited by the width of the detector pulse. TCSPC is a thresholding technique- only the first part of the voltage pulse from the detector is used to indicate the stop of the timing process. This is accomplished via the means of a constant fraction discriminator (CFD). A constant voltage threshold does not fully exploit the high timing resolution that is achievable using TCSPC as demonstrated in Figure 2.4. The voltage discriminator level (dashed line) is set to a value which enables all output pulses of the device to be counted, if the voltage pulse does not exceed this level, the pulse will not be counted. Since the voltage pulse from the detector may differ slightly in magnitude, a threshold voltage might be achieved at a slightly different time which would lead to increased inaccuracy of the timing.

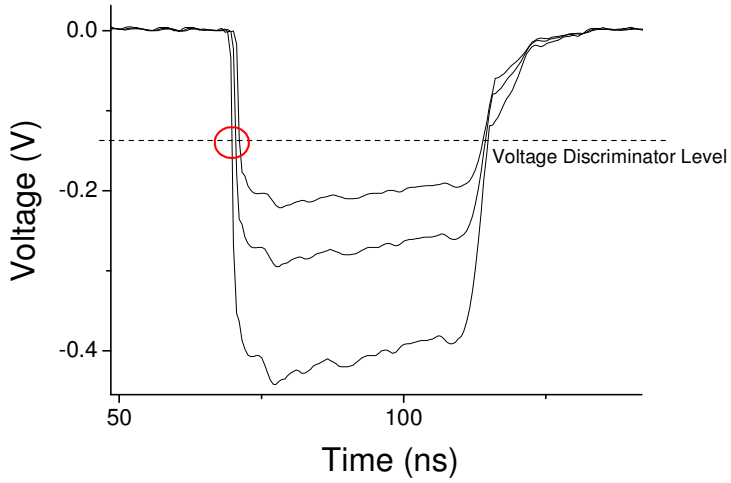

Figure 2.4. Single-photon detector output as seen on an oscilloscope. The differing pulse magnitudes have been exaggerated for clarity. The voltage discriminator level (dashed line) is set to a value which enables all output pulses of the device to be counted. However as highlighted in the red circle, the voltage pulses pass through the discriminator level at different times relative to the start of the individual measurement which will add jitter to the time differences between the start and stop pulses.

Instead, as demonstrated in Figure 2.5, the CFD method, as the name suggests, uses a constant fraction point on the leading edge of the pulse to trigger the timing stop pulse resulting in a constant timing point for pulses with similar shapes yet varying amplitudes. In Figure 2.5, we have a voltage pulse of height V and the discriminator set to time the pulse at a constant fraction, f, of the pulse. The pulse is split into two parts; in (a) the original pulse has been delayed by δ and inverted; (b) shows the original pulse attenuated to a maximum amplitude of fV. The sum of the signals is shown in (c) to give the zero crossing signal [10]. The CFD fires when the bipolar signal in (c) changes polarity.

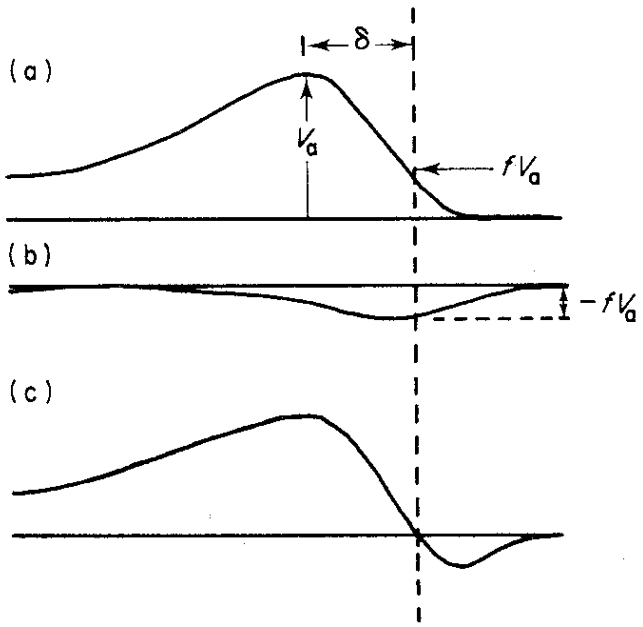

Figure 2.5. Demonstration of CFD operation. The original signal, of amplitude V_a, is delayed (by δ) and inverted in (a), (b) is the original signal attenuated to fV_a. The sum of (a) and (b) gives the bipolar signal (c). When the bipolar signal changes polarity (indicated by the dashed vertical line) the CFD fires [10].

The TAC within a photon counting card can only register one stop per each start event. The TAC then has a certain reset, or "dead-time", during which time no stop pulses can be counted. Therefore, the count rate of a TCSPC system must not exceed ~ 10 % of the overall system repetition rate (the "start" rate) i.e. the probability of detecting a photon per clock period is much less than unity. This avoids a problem known as "pulse pile-up" whereby there are many photons but only one start-stop pair per clock-cycle so only early events are recorded in the TAC window. This leads to a skewing of the recorded histogram towards the start of the timing window and results in an unreliable measurement since the likelihood of observing any photon counts in the latter part of the window is greatly reduced. Algorithms have been developed, such as that by Coates [12], to correct the distortion caused by pulse pile-up. However for the measurements described throughout this Thesis, the count rate was always less than 10 % to avoid pulse pile-up.

Finally in this brief review of TCSPC, we must consider noise within the technique. Noise is apparent from two contributing sources: (1) the Poissonian noise within the number of counts registered per time bin and background; (2) "dark" counts from the

detector. The Poissonian noise is dependent on the number of photon counts per time bin and is can be expressed as the standard deviation of the counts in a bin i where $\sigma_i = \sqrt{N_i}$, and N_i represents the number of counts in time bin i. To maximise the signal to noise of a TCSPC measurement, N_i must be high compared to the dark counts registered. The demands this places on single-photon detectors will be explained in the following section.

2.3 Single-Photon Detectors

Single-photon detectors must be capable of high amplification paired with an extremely low level of noise. In terms of amplification for "avalanche" devices, for each photon detected an output current normally in the order of 1,000,000 electrons, or greater, flows through the device and provides a measurable current at its output. In addition, the reset time between detection and subsequent readiness to detect a photon must be short in order to maximise operating count rate. Most single-photon detectors are characterised using parameters including: Detection efficiency, referred to herein as single-photon detection efficiency (SPDE) which is a measure of how efficiently the device detects incident photons. The dark count rate (DCR) represents the number of times the detector is triggered within 1 second by events unrelated to photon detection such as events triggered by thermally generated carriers. Noise equivalent power (NEP) is a quantification of device sensitivity. It represents the least measurable optical power (with 1-Hz bandpass noise filtering, that is, 1-s total counting time in single-photon counting) and is given by the following equation:

$$NEP = \frac{h\upsilon}{SPDE}\sqrt{2DCR} \qquad \text{Equation 2.1}$$

Where h is Planck's constant, υ is the frequency of the light incident upon the detector. The lower the NEP, the more sensitive the device. Other parameters including photon-timing jitter and device active area will be discussed. A review of single-photon detectors currently available for use in TCSPC applications is given below, followed by some more recent emerging detector technologies that are not yet commercially available.

2.3.1 Photomultipliers

Generally, TCSPC applications employed photomultiplier tubes (PMTs) as detectors [13] [14] [15] [16] [17]. A schematic representation of a typical PMT structure is shown in Fig. 2.6. The tube itself is a vacuum device with a photocathode at its entrance. Depending on the material composition of the photocathode, PMTs can be effective for detection of light at varying wavelengths. Following the absorption of a photon the photocathode releases an electron which is accelerated towards the first dynode where further electrons are emitted due to the increase in kinetic energy of the initial accelerated electron. Each subsequent dynode is charged at a higher positive potential than the previous resulting in amplification in the order of 10^6. There are three main designs for dynode configurations: "Venetian blind," "box and grid," and "focussed dynode chain". The focussed dynode chain offers the highest electron transfer efficiency and shortest response time since secondary electrons are focussed on the centre of the adjacent dynode resulting in a shorter transit-time between dynodes [18].

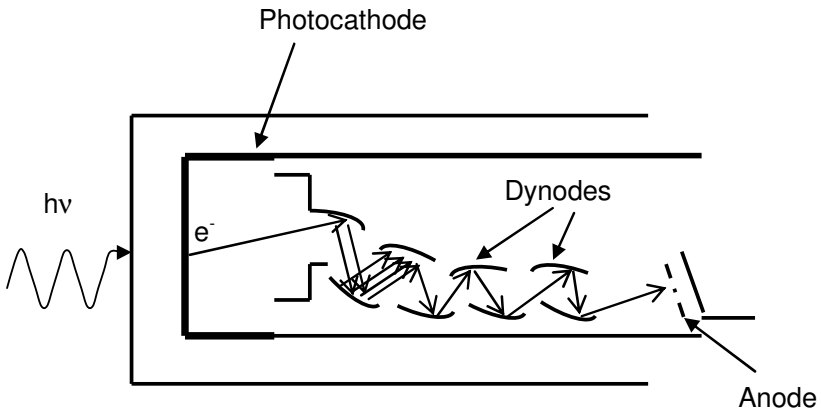

Figure 2.6. Schematic of a "focussed dynode chain" PMT; the process of electron multiplication from each dynode stage causes a measurable current to be detected.

The advantages of PMTs include their large active areas [19] and high internal gain (10^4 - 10^7). Whereas most of the other single-photon detectors that will be introduced next have active areas of 10's - 100's μm in diameter, PMTs have photocathodes that span the mm range resulting in easier alignment and integration in certain systems. There are, however, several disadvantages with such devices, including relatively large devices with poor mechanical stability and low SPDE (usually a few % in the visible). PMTs also require a high bias voltage in the order of 1 kV and their timing jitter (fluctuation of transit time) is typically in the region of 1 ns [20]. Therefore, in many modern photon counting applications, PMTs are far from ideal where higher efficiencies

and lower jitter are required. However, PMTs generally do not have a spectrally dependent instrumental response (unlike some semiconductor-based detectors), and much improvement has been seen in miniaturisation of the PMT packages.

Hamamatsu has recently developed a photomultiplier (H10330-45/-75) [21] that detects in the near infrared. To accomplish this, a photocathode of InGaAs was used in order to extend the spectral responsivity up to 1700 nm. Again, this devices require a high bias and must be cooled to 200 K in order to reduce the DCR which, when cooled, is ~ 10^5 Hz although the detector area is comparatively large (~ 1 mm diameter) compared to the active area of semi-conductor detectors (10 - 100's of µm in diameter). Figure 2.7 shows the quantum efficiency (QE) of two devices manufactured by Hamamatsu, at best their efficiency is ~ 2 %. The QE follows a different gradient to that of the cathode radiant sensitivity since they are related by Equation 2.2.

$$QE = S\frac{h\upsilon}{e} \qquad \text{Equation 2.2}$$

Where S is the cathode radiant sensitivity, *h* is Planck's constant, υ is the frequency of the light incident upon the detector, and *e* is charge on an electron.

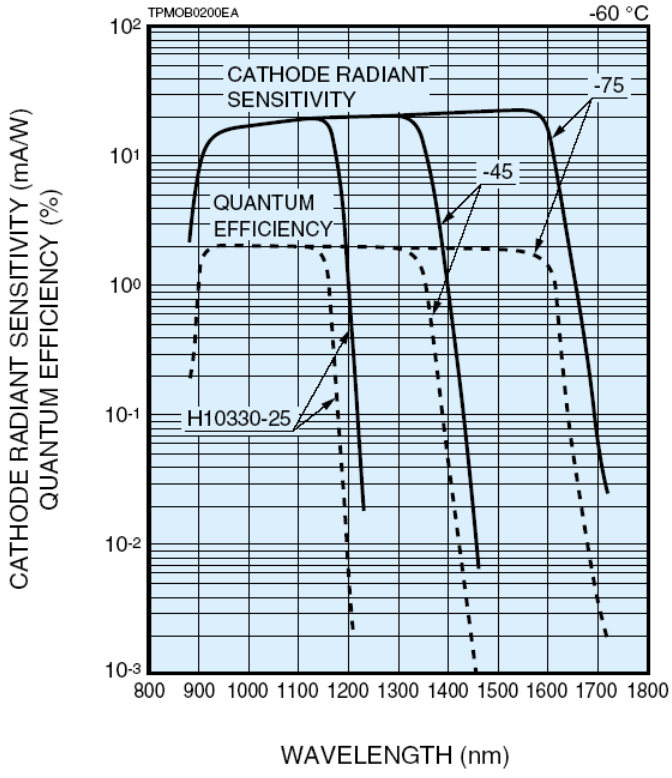

Figure 2.7. Quantum efficiency of three Hamamatsu PMT devices at -60 ºC [21].

2.3.2 Microchannel Plates

Microchannel plates (MCP) are similar in structure to PMTs. They consist of a thin disc containing many thin glass channels (~ 10 μm in diameter) fused in parallel in a 2D array as shown in Figure 2.8. The input electron is accelerated towards the channel wall where it collides, releasing secondary electrons. The interior of each capillary is coated with a photo-emissive material and biased at each end, thus acting as a continuous dynode. This process is repeated several times along the length of the channel constituting an exponential multiplication. The main advantage of such detectors is their 2D configuration which makes them ideal for imaging where they are used as image intensifiers. MCPs have been used in photon counting lidar systems [22].

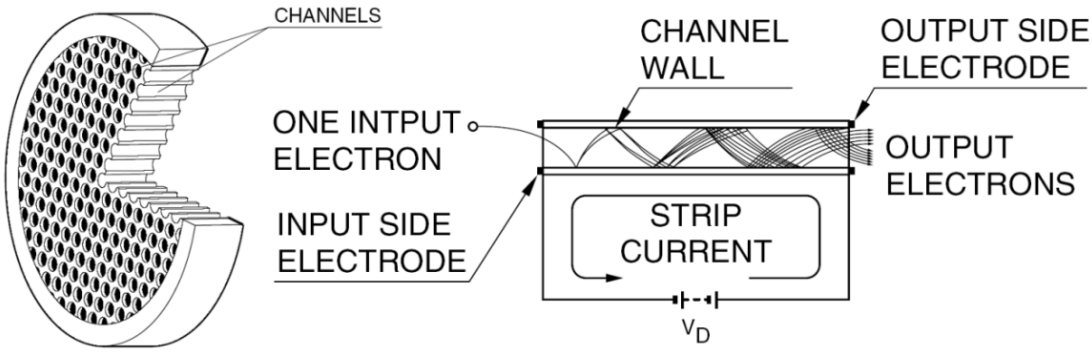

Figure 2.8. MCP schematic and operating mechanism [23]

2.3.3 Single-Photon Avalanche Diodes

A single-photon avalanche diode (SPAD) is an avalanche photodiode (APD) reverse biased at electric fields above that of the breakdown voltage [24]. This means it is operated in "Geiger-mode" as opposed to "linear mode" (reverse bias below breakdown for an APD). Diode structures suitable for use as SPADs have been implemented in silicon, germanium and compound semiconductors and comprise of either a p-n or p-i-n junction.

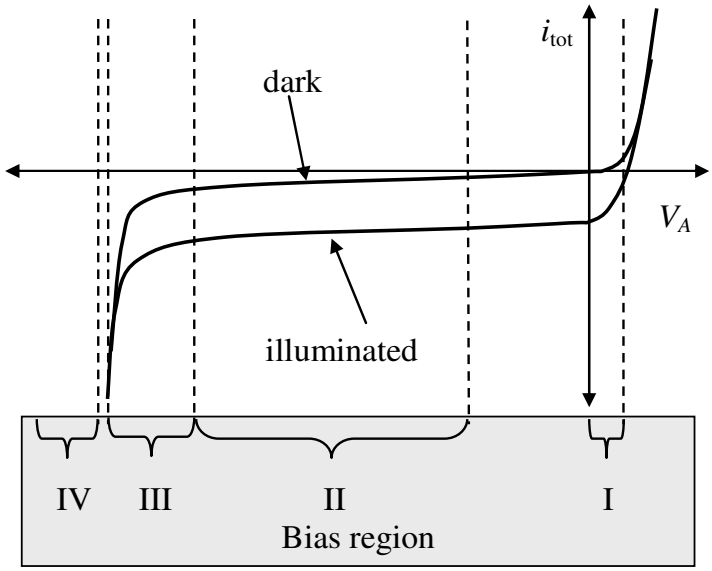

Figure 2.9. Current-Voltage characteristic of an APD structure [25]

Figure 2.9 represents the current-voltage characteristic of a p-n junction, in this case an APD. The plot has been split into four discrete bias regions.

Bias region I relates to forward bias, under which conditions the device will conduct and a positive current will flow. It is reverse bias that is of utmost importance to detector operation.

In bias region II there are two different traces, dark and illuminated. The "dark" current is the current that flows through the device under no illumination. The dark current can be accounted for by such processes as thermally generated carriers and leakage currents. The "illuminated" current is due to the photoelectric effect - for every photon absorbed an electron-hole pair is created as long as the following equation is satisfied (see Figure 2.10 for schematic of the photoelectric effect)

$$\lambda_c = \frac{hc}{E_g} \qquad \text{Equation 2.3}$$

Where λ_c is the absorption cut-off wavelength, h is Planck's constant, c is the velocity of light and E_g is the energy gap of the semiconductor.

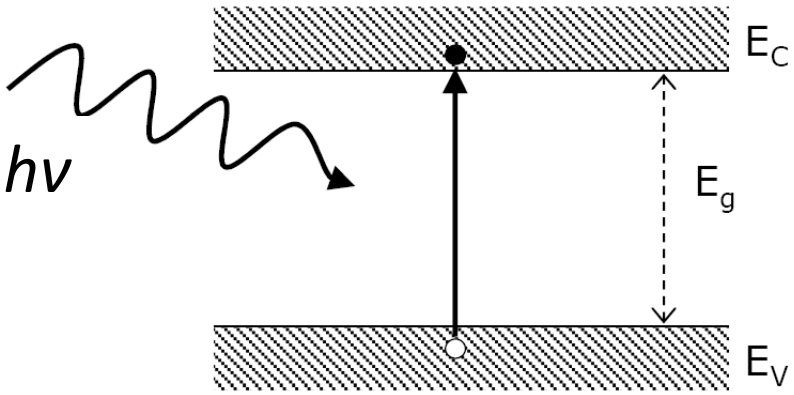

Figure 2.10. Absorption of a photon of energy hv in a semiconductor with energy gap E_g, creating an electron-hole pair, promoting the electron to the conduction band, where E_v and E_c are the valence and conduction bands respectively.

Bias region III is the region within which telecoms APDs are operated. At such electric fields within the device, an electron-hole pair created by an incoming photon can undergo impact ionisation, a process whereby the electrons and holes are accelerated in opposite directions by the high electric field and can ionise other atoms upon impact with the crystal lattice. This mode of operation is known as "linear-mode" and a photo-generated electron-hole pair can be amplified by a gain factor of typically 10-1000.

Finally, bias region IV relates to electric fields beyond avalanche breakdown, the so-called "Geiger mode". As before, an incoming photon creates an electron-hole pair. The primary carriers are accelerated due to the electric field and impact ionisation takes place. Since the electric fields are so high this process is self sustaining [26] and leads to avalanche multiplication. Here the gain is infinite, or meaningless, and the avalanche current will continue to flow until quenched by an external factor (usually accomplished by lowering the bias below breakdown). It is in this mode that SPADs are operated - the absorption of a single-photon leads to a detectable current output, the process is summarised in Figures 2.11 and 2.12.

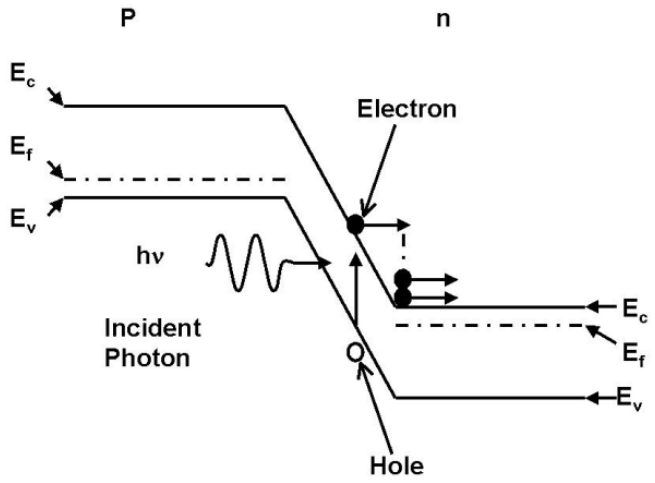

Figure 2.11. An incident photon is absorbed in the depletion region of the p-n junction, causing an electron to be promoted to the conduction band, leaving behind a hole in the valence band. If there is a high enough electric field, carriers can gain sufficient kinetic energy to cause impact ionisation upon collision with the lattice. This is repeated many times resulting in a multiplication process which generates a self-sustaining avalanche as shown in Figure 2.12 below.

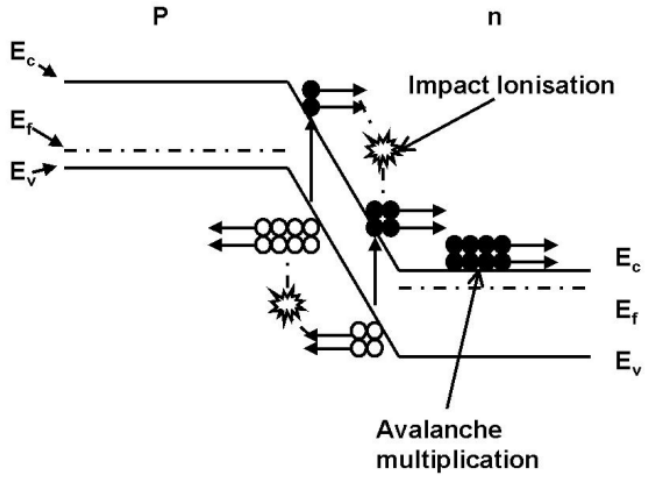

Figure 2.12. The electron-hole pairs that were created from impact ionisation undergo a multiplication process, whereby the number of charge carriers grows exponentially. This is known as avalanche multiplication. As the number of charge carriers continues to rise, a detectable current of a few mA flows through the device.

Investigation of the physics of avalanche breakdown in SPADs started back in 1964 [27], but it was not until 1981 that Cova *et al.* developed a practical thin-junction Si SPAD for use in TCSPC systems [28]. The first SPADs to be made were Si devices and the first company to make them commercially-available was Perkin-Elmer (formerly EG&G Optoelectronics, Canada) in the early 1990's. Their single-photon counting module (SPCM) is an example of a thick junction device and that designed by Cova is a shallow junction SPAD. As the names suggest, the main difference between the two lies in the thickness of the main junction where absorption takes place. Figure 2.13 shows the differences in structure between thin (~ a few μm) and thick junction (10's μm) SPADs. Their characteristic differences caused by the junction thickness can be summarised in Figure 2.14 (a) & (b). While the shallow junction SPAD has an excellent timing jitter of 45 ps, its SPDE at wavelengths > 600 nm is considerably less than that of the thick junction SPAD. Therefore we see there is a trade-off between SPDE and timing response. In 2005, Professor Cova established a university spin-off company Micro-Photonic-Devices (MPD) which now sells shallow junction devices.

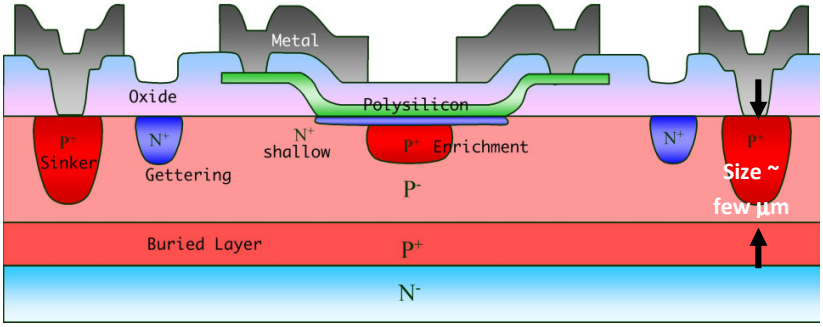

Figure 2.13. (a) Schematic cross section of a thin junction silicon SPAD structure, figure supplied by Sergio Cova, Politecnico di Milano, Italy.

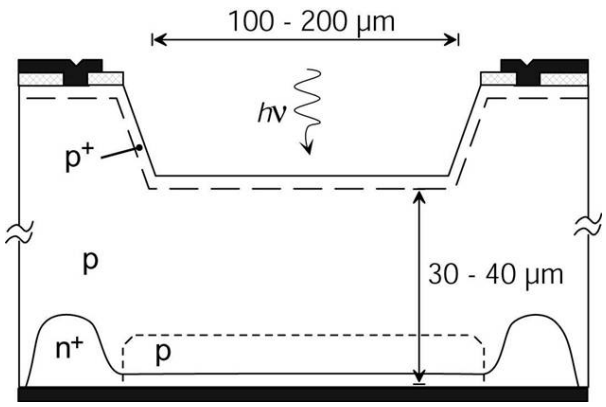

Figure 2.13. (b) Cross-section of thick junction SPAD showing approximate dimensions.

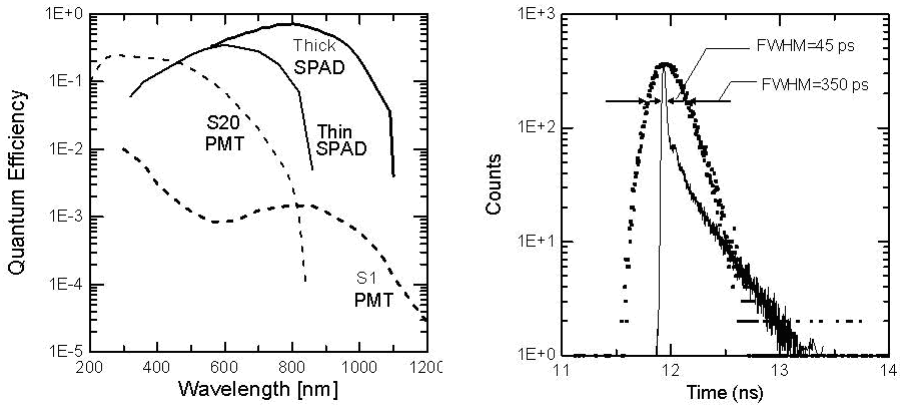

Figure 2.14 (a) Quantum Efficiency (SPDE) as a function of wavelength of thick and shallow junction SPADs compared to two PMTs. (b) Timing response for thick (350 ps) and shallow (45 ps) junction SPADs [29].

Other research efforts have seen the use of standard Complementary Metal-Oxide-Semiconductor (CMOS) to produce SPADs and SPAD arrays [30] [31]. The interest in using CMOS processing for SPADs is driven by the advantages it brings to the associated electronics required for SPAD operation. Using a SPAD with separate electronic circuits often results in extra problems such as high parasitic capacitance. Using CMOS, however, the electronics (quenching electronics, time-to-amplitude converter etc) can be integrated on-chip reducing capacitance, dead time, power dissipation and improving packaging. An SPDE of 41% with a DCR of 100 kHz at room temperature was reported in [32].

As mentioned previously, the SPDE of silicon SPADs reduces significantly at wavelengths greater than 1 μm as shown in Figure 2.14 (a). Until a few years ago, there were no longer wavelength SPADs available commercially, hence part of the reason for the work accomplished by the groups at Heriot-Watt and the University of Sheffield (some of which is covered in [33]) preceding this thesis. However, there are commercially available InGaAs/InP avalanche photo diodes (APDs) which operate at wavelengths > 1 μm. These devices normally operate in linear multiplication mode (reverse-biased below breakdown). They can, however, be exploited for use as single-photon detectors when operated in Geiger mode [34] [35] [36] [37] where the bias is above that of breakdown. They have shown good QE (10's of %) and low jitter (FWHM ~ 300 ps).

More recently, Princeton Lightwave Inc. have started manufacturing InGaAs/InP SPADs specifically designed for Geiger-mode operation, and have reported SPDEs in

excess of 20 % [38]. These devices will be discussed further in Chapter 3 and 4. Lincoln Laboratories have reported InGaAs/InP SPAD design and growth with SPDEs up to 45 % [39] and their afterpulsing performance will be discussed in Chapter 4, although these devices are not commercially available. A paper from Liu *et al.* reported an SPDE of 45 % at = 1310 nm with excellent NEP of 4.5×10^{-17} W/Hz$^{1/2}$ [40].

In the mid-1990s, Germanium APDs were characterised as SPADs [41] [42]. Their performance compared to that of other SPADs and two PMTs is displayed in Figure 2.15. The main problem with Ge SPADs was the high DCR which has to be limited by cryogenic cooling. At room temperature, Ge would absorb at wavelengths beyond 1550 nm, but at the temperatures the devices were tested (77K), the cut-off was a little under 1500 nm. The SPDE of a Ge SPAD was measured to be a modest ~ 10 % and sub 100 ps timing jitter. Ge devices also suffered from a high level of afterpulsing, a phenomena also apparent in InGaAs/InP devices which will be discussed in depth in Chapter 4.

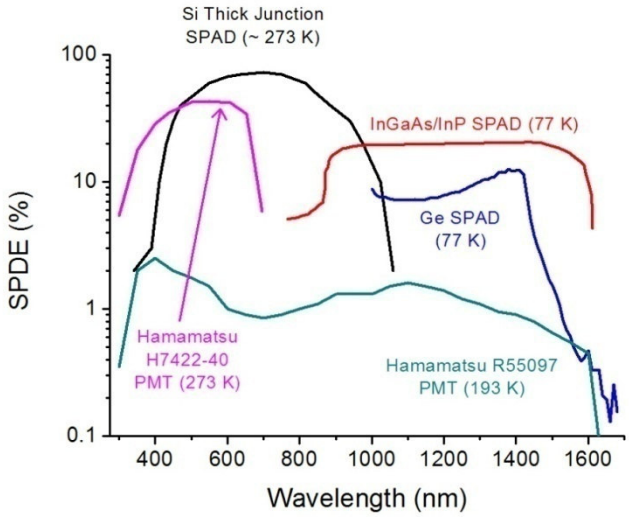

Figure 2.15. Plot of single-photon detection efficiencies vs. wavelength for: a silicon thick junction SPAD, an InGaAs/InP APD (operated in Geiger mode), a germanium SPAD, a Hamamatsu Infrared PMT, and a visible wavelength high efficiency Hamamatsu PMT.

The way in which a SPAD is biased and how the avalanche is quenched is crucial in determining the most suitable operating conditions for a given application. Once an avalanche is triggered, it is a self-sustaining process. Therefore, a quenching circuit to stop the avalanche current flowing and returning the detector to its quiescent state is necessary. The differing methods are described in the following subsections.

2.3.3.1 Gated Mode Quenching

Gated mode is the most common way in-which an InGaAs/InP SPAD is operated, and is the method adopted in Chapter 3 for device characterisation. As shown in Figure 2.16, the SPAD is reverse-DC biased (V_{DC}) a few volts below the breakdown voltage (V_{BD}). A short electrical pulse ($V_{G,}$ variable in duration, for characterisation 100 ns was used) is then superimposed upon the DC bias to take the device beyond avalanche breakdown and into Geiger-mode. When the gate is placed upon the SPAD, the device will remain in its quiescent state until an electron-hole pair (either photo-generated or "dark" carrier) is accelerated by the electric field such that impact ionisation occurs and a self-sustaining avalanche is initiated. The avalanche current rises quickly until it reaches the stable latching current. The avalanche is then quenched by the end of the gate-on period when the detector returns to the constant bias supplied by V_{DC}.

Gated mode quenching is most suited to characterisation since it allows the detector to be activated coincident with a highly attenuated laser pulse such that the SPAD is gated at the same repetition rate as the laser. Gated mode operation only allows dark counts within the gate period, thus reducing the total amount of charge flowing through the device and limiting the effects of afterpulsing (see Chapter 4).

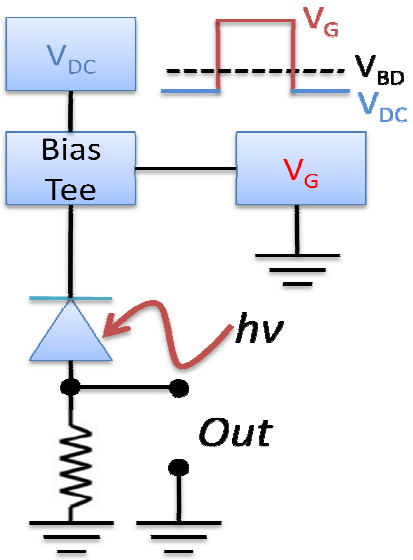

Figure 2.16. Gated mode circuit schematic. V_{DC} is the constant reverse DC bias placed on the SPAD which holds it just below the breakdown voltage, V_{BD}. A gate of amplitude V_G is superimposed to take the SPAD into Geiger mode. The self-sustaining avalanche is quenched when the gate is switched off. The avalanche is sensed across the R_{out} resistance, which is normally a photon counting card or a fast oscilloscope (50Ω).

2.3.3.2 Passive Quenching

Passive quenching is a simple quenching technique as demonstrated in Figure 2.17. The SPAD is reverse biased above breakdown through a quenching resistor, R_Q, of usually 100 kΩ or more [43] and the output sensed in the same way as gated quenching described previously.

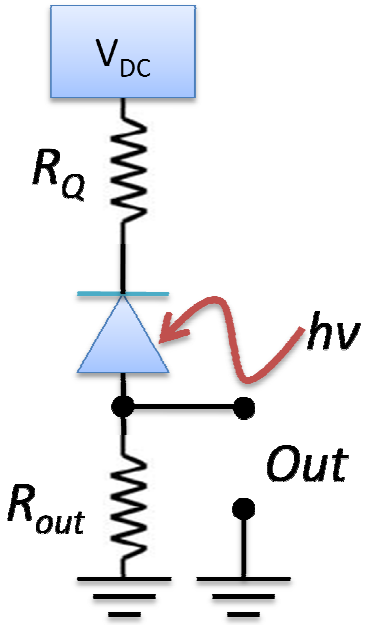

Figure 2.17. Passive quenching circuit where R_Q is the quenching resistor and V_{DC} is a constant bias above breakdown.

When the SPAD is DC biased through R_Q above breakdown and ready to detect a photon, there is no current flowing in the circuit. As soon as an avalanche is triggered, current flows through R_Q and thus causes the voltage across the SPAD to drop below V_{BD} and quenches the avalanche. The reset time is limited by the SPAD's capacitance and the value of R_Q. The Authors of [43] state that (for Si SPADs) even if the capacitance is very low (< 1 pF) and the excess bias is no more than a few volts, coupled with the minimum value of R_Q (~ 100 kΩ), the reset time will be ~ 1 μs thus drastically limiting the maximum count rate. It should also be noted that this configuration is far from ideal for InGaAs/InP SPADs due to the high level of afterpulsing and the high DCR of these detectors. If these devices were used with a passive quenching circuit the detector would be constantly triggered by trapped carriers since there is no forced hold-off time to allow trapped carriers to decay.

2.3.3.3 Active Quenching

An active quenching circuit (AQC) is a circuit within which a SPAD can be integrated in order to actively sense the onset of an avalanche pulse, quench it, and subsequently reset the SPAD for the next photon event as quickly as possible. One such circuit is demonstrated in Figure 2.18. The fast comparator (Comp in Figure 2.18) senses the rise of the avalanche pulse, the comparator's output then switches the bias voltage source to less than V_{BD} to quench the avalanche. The voltage supply to the SPAD is kept below V_{BD} for a controlled period of time (hold-off) to allow the release of any trapped carriers to avoid the effects of afterpulsing. The output from the comparator is also used as the photon-counting signal for recording the arrival time of a photon since it is coincident with avalanche's rise. The advantages of an AQC derive from the fast transitions between quenching and operating levels and the short avalanche pulse resulting in fewer carriers flowing through the device per event thus limiting afterpulsing and reducing the necessary associated dead time.

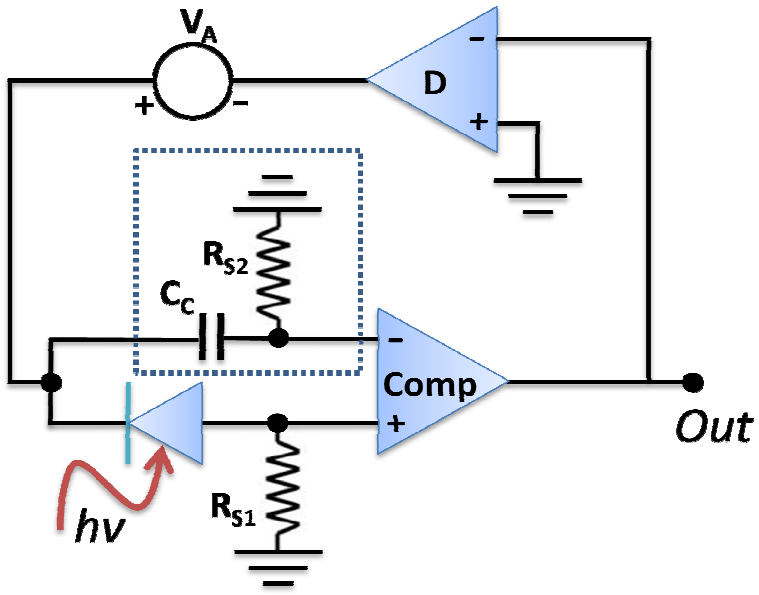

Figure 2.18. Simplified basic AQC diagram in an 'opposite sensing and quenching terminals' arrangement. The network within the dotted blue box is employed to avoid circuit oscillations by compensating for the current pulses injected from the quenching pulse through the SPAD capacitance. R_{S1} is the quenching resistor, Comp is the comparator and D is the quenching and reset driver, after [43].

2.3.4 Arrayed Silicon APD

In applications where large detector areas are required the long-favoured PMT may now have a realistic competitor in the form of the arrayed silicon APD, commonly referred to as silicon photomultiplier (SiPM). An SiPM is a multi-micropixel (10^3 mm^{-2}) semiconductor device where each Geiger mode APD is joined together on a common substrate and working on a common load [44]. The use of a common load means that the outputs of each single pixel are summed together. This makes photon-number resolution possible, since when two photons are coincidentally detected, an output pulse magnitude twice that of a single-photon measurement is observed. The drawback with this operating scheme is that the dark counts from each pixel are combined, although the overall number can be reduced by cooling the detector. The fill factor of a 1 mm^2 SiPM is about 25 % according to the Authors of [44].

SensL, a company who manufacture and package SPADs, now fabricate SiPMs and sell them as packaged detectors with the necessary circuitry for biasing and output readout. The SPDE of a SiPM is ~ 20 %, depending on overbias, at a wavelength of ~ 500 nm and falling to ~ 6 % at 800 nm [45]. Figure 2.19 shows, on the left a schematic for a single pixel, in the centre a schematic of part of the entire SiPM array and a microscope image of a number of pixels. Each pixel is passively quenched through RQ although the reported dead time was only 100 ns per pixel.

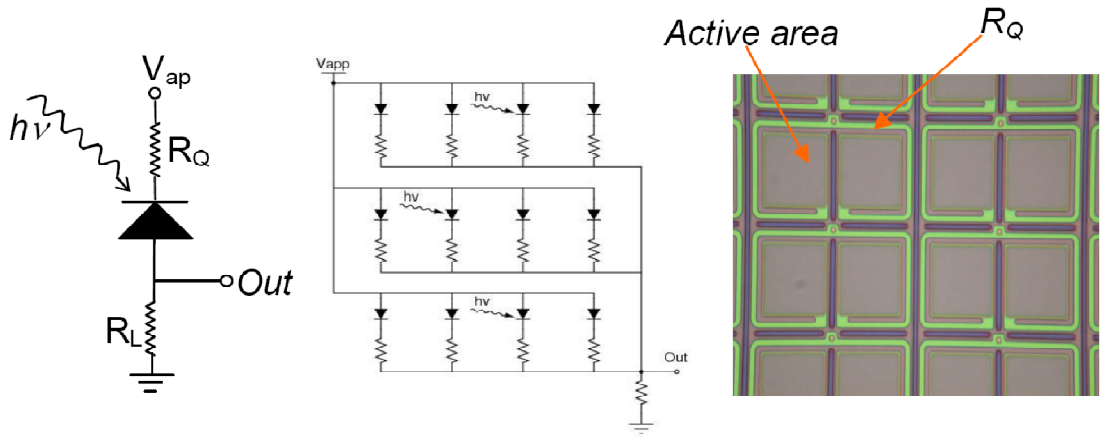

Figure 2.19. Left: single-pixel electrical circuit schematic, centre: schematic of multiplexed pixels, right: microscope image of a number of pixels showing the active area and R_Q [45].

The following sections present emerging photon-counting detector technologies.

2.3.5 Frequency Up-conversion

Frequency up-conversion [46] is the process of up-converting a photon from the IR (e.g. λ = 1550 nm) and directing it into a non-linear crystal (usually Periodically Poled Lithium Niobate or PPLN) along with an escort, or pump, laser wavelength (e.g. λ = 1064 nm) to a visible wavelength by sum-frequency mixing [47]. The up-conversion process thus enables a single-photon at an IR wavelength to be down-converted to a visible wavelength and hence the use of a Si SPAD as the detector, yielding greater SPDE, lower DCR, and virtually no afterpulsing. An example of the setup required for frequency up-conversion is shown in the Figure 2.20. The DCR within such a system is not limited by the Si SPAD, instead it is the parasitic nonlinear interactions within the PPLN crystal like spontaneous Raman scattering, parametric fluorescence, and second harmonic generation from the escort beam that dominate the DCR [48]. The up-conversion system efficiency is mainly limited by coupling and propagation losses and, of course, the SPDE of the SPAD.

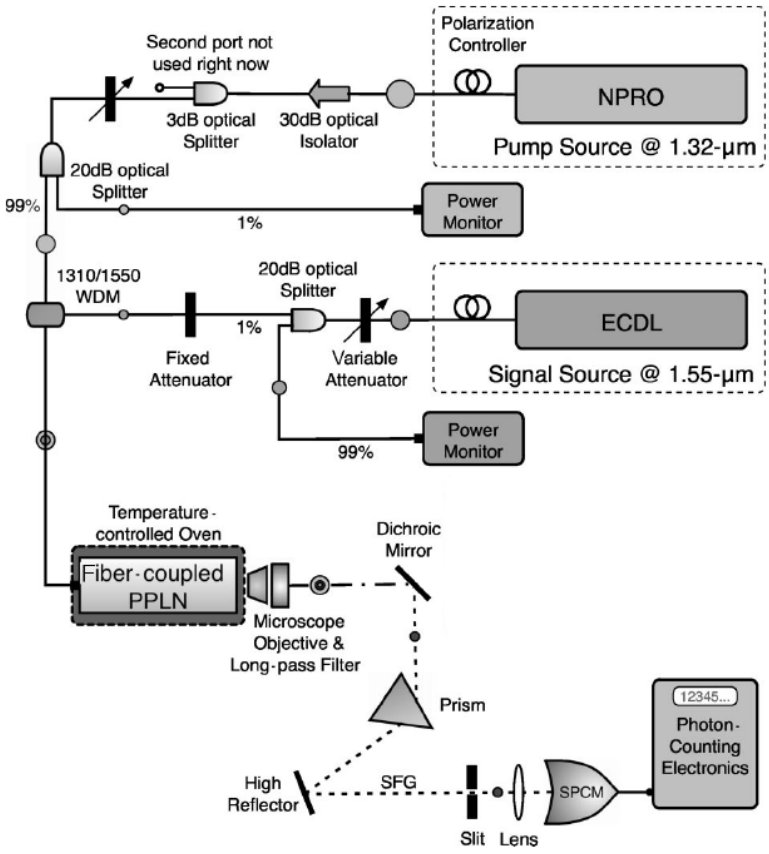

Figure 2.20. Frequency up-conversion schematic system setup where the single-photon at a visible wavelength is spectrally filtered out from the PPLN output using a prism, and using a Si SPAD as the single-photon detector [48].

Conversion efficiencies of ~ 80 % have been reported [49] whilst overall system efficiencies exceeding 46 % at 1.56 μm were detailed by the Authors of [48]. The count rates achievable (~ 15 MHz) are much higher than those possible with InGaAs/InP SPADs, although the main disadvantages of PPLN up-conversion are the cost, size and complexity of the setup. However, there have been practical demonstrations of up-conversion detectors used in QKD applications [50].

2.3.6 Visible Light Photon Counters

Visible light photon counters (VLPCs) are solid state Si diodes using the avalanche multiplication effect in an impurity band in silicon [51]. Single-photons are converted in to thousands of electrons but in contrast to normal APDs, only one species of carrier is multiplied. The bandgap across which the multiplication takes place is 50 meV. This impurity band lies 50 meV below the conduction band [52]. Since the band is so narrow, infrared photons of up to 28 μm in wavelength can excite electrons causing large DCRs up to 10^{15} c/s at room temperature. For this reason, the detector must be cooled to 6.4 K and in reference [53] was encased in a threefold-shield cryostat to stop room temperature radiation reaching the detector. A window to optically address the VLPC was incorporated and was capable of transmitting visible photons with high efficiency (97 % at 694 nm). Measured QE of a VLPC system of ~ 70 % was reported with a DCR of 2 x 10^4 c/s with a 1 mm detector diameter and count rates up to 10^7 c/s and no afterpulsing [53]. It has also been reported in reference [54] that VLPCs are capable of photon number resolution i.e. the detector can differentiate between 1, 2 or 3 etc. photons being absorbed simultaneously. The shielding and temperature issues may be the reason why these devices are not readily used in many photon-counting systems.

2.3.7 Quantum Dot-based Detectors

For several years, quantum dot field effect transistors (QDFETs) have been investigated and developed capable of single-photon sensitivity [55]. One such device is shown below in Figure 2.21. The detector consists of a GaAs/$Al_{0.33}Ga_{0.67}As$ field effect transistor where the channel is gated by the quantum dot (QD) layer. The efficiency of such devices depends on the ability of a dot to capture a single photo-excited carrier which results in a sizeable change in the source–drain current of the transistor, allowing the detection of a single-photon. The reported SPDE of the device in Figure 2.21 was only ~ 0.9 % at a wavelength of 650 nm (cooled to 77 K) although it was suggested that the operational wavelength could be shifted to 1550 nm by

translating the layer structure to InGaAs/InAlAs although at present, this has not been demonstrated.

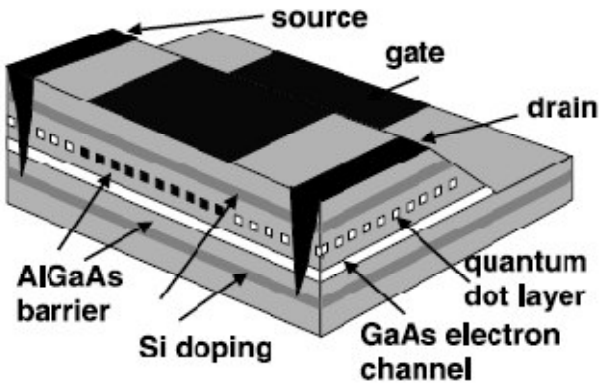

Figure 2.21. Schematic of the cross section of the QD single-photon detector. different layers grown by MBE are represented by varying shades of grey and 'active' dots in the device are shown in black [55].

A further paper from the authors of [55] showed the capability of the QDFET to perform photon-number resolving [56] which is desired for numerous applications, but in particular for the characterisation of single-photon sources [57].

In 2006, Rowe *et al.* reported SPDE up to 68 ± 18% at 800 nm with the device shown in Figure 2.22. operating at 4 K [58].

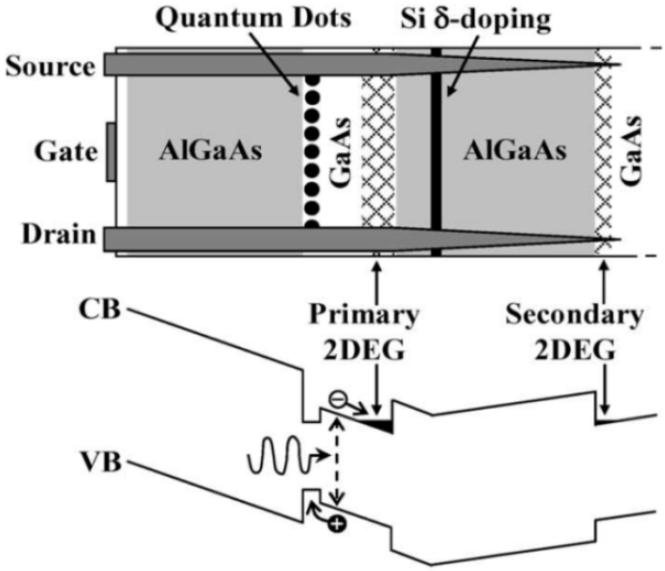

Figure 2.22. Quantum dot optically gated field-effect transistor as a single-photon detector [58].

Quantum dot structures have been exploited further [59] through the development of the QD resonant tunneling diode. Figure 2.23 shows the band structure, the black lines show the device under forward bias, close to resonance. The current flowing between the emitter and collector is restricted by tunneling through the double barrier. When the QD captures a photo-excited hole this lowers the potential of the dot and alters the resonant tunneling condition, shown by the red lines allowing the detection of single-photons. These devices have shown a much improved SPDE of ~ 10 % at a wavelength of 550 nm only when cooled to 4 K. Their timing jitter is the main disadvantage as this was reported to be 150 ns resulting in an extremely low repetition rate of detector operation.

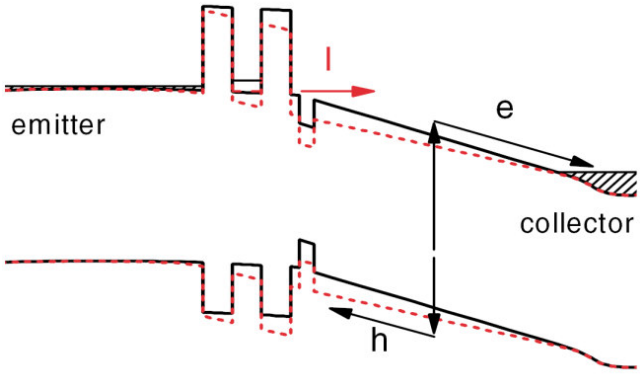

Figure 2.23. Schematic band structure of a quantum dot resonant tunnelling diode in forward bias (black) and after capture of photo-excited hole (red) [59].

Following on from this work, an InP based AlAs/$In_{0.53}Ga_{0.47}As$/AlAs quantum dot resonant tunneling diode was designed and grown to extend the detection wavelength to 1.3 μm [60]. At 4.5 K a single-photon detection efficiency of 0.35 % at a certain discriminator level, although it was suggested that this could be increased with a thicker absorption layer. The DCR of such devices is caused by electrons escaping from a quantum dot. At such a low temperature it is argued that thermally activated escape is negligible and that tunneling is responsible, dependent on the confinement energy and the electric field over the barrier layer. To increase the confinement, a material with higher barriers for electron and holes could be used.

2.3.8 Superconducting Single-Photon Detectors (SSPD)

In a superconducting material, the binding energy of Cooper pairs is ~ meV. Therefore, the absorption of a single-photon (~ eV energy range) can break a large number of these Cooper pairs to create quasiparticles which may perturb the superconducting material's electrical properties [61]. This is exploited in the following types of superconducting single-photon detectors.

2.3.8.1 Transition Edge Sensors

Superconducting Transition Edge Sensors (TESs) are biased close the superconducting/normal metal transition edge in order to detect a measurable increase in resistance when a photon is absorbed as in Figure 2.24. These detectors offer excellent SPDE at near IR wavelengths (88 % at 1550 nm in [62] and 95 % in [63]) and negligible dark counts (10 counts per sec) but suffer from poor timing attributes, namely 90 ns timing jitter at full-width-half-maximum (FWHM) and a reset time of 4 μs [64]. They also have the advantage of photon number resolution [62]. A major disadvantage of such devices is the temperatures at which they must be operated, ~ 100 mK in an adiabatic demagnetisation refrigerator.

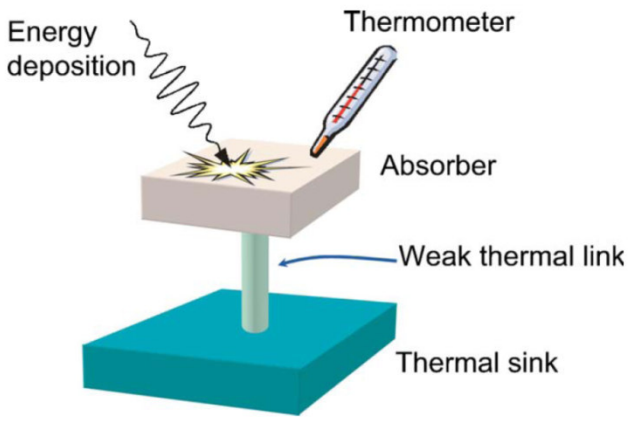

Figure 2.24. Both the absorber and thermometer in this TES are composed of a thin film of tungsten. A DC bias maintains the tungsten electrons on the edge of the transition between normal and superconducting conditions. An incident photon deposits energy which is read out as change in temperature by the thermometer since the resistance is highly dependent on the temperature. The weak thermal link is made due to the low electron-phonon coupling in tungsten [62].

2.3.8.2 Niobium Nitride Superconducting Single-Photon Detectors

In 1991, Gol'tsman *et al.* pioneered NbN as a single-photon detector using a long narrow strip of NbN as the absorber [65]. Unfortunately, the SPDE of these devices was poor due to the width of the wire and the low probability of a photon being incident. It would seem logical to increase the width hence increasing the probability of a photon being absorbed by the wire. However, due to the process involved in the absorption this is not feasible since a wider or thicker wire would not be sufficiently resistive. Instead, the NbN wire was arranged in a meander style as shown in the scanning electron microscope (SEM) image in Figure 2.25. This style of meander wire results in a 50 % fill factor and increases the probability of a photon being absorbed.

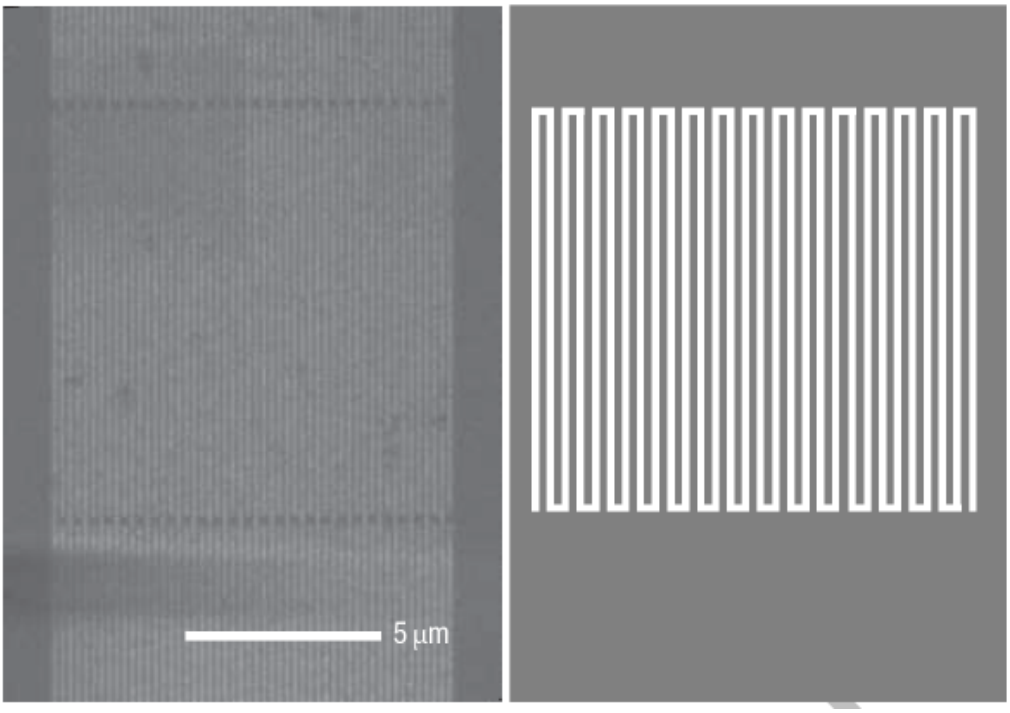

Figure 2.25. SEM image of a NbN superconducting single-photon detector (10 μm x 10 μm, 100 nm pitch) on left. Right shows a schematic representation of such a device clearly showing the meander pattern of the wire (images courtesy of R. H. Hadfield).

These devices were developed at the Moscow State Pedagogical University and comprise of an extremely thin (~ 5 nm) and narrow NbN stripe cooled to 4.2 K [66]. The strip is current biased at a specific current. When a photon is absorbed a "hotspot" of a certain volume (proportional to the photon energy) is generated leading to a temporary formation of a resistive barrier across the superconducting sensor strip and results in an easily measurable voltage pulse as in Figure 2.26. This is the reason that the wire cannot be made wider – if the cross-section of the wire is small, there is a more

dramatic effect on the current distribution upon the absorption of a single-photon, and hence the hotspot will be more likely to trigger a voltage pulse. The hotspot 'heals' itself in approximately 30 ps [67] re-entering its previous superconducting state ready to detect another photon resulting in a very low jitter detector. Initial tests on these devices as single-photon detectors and showed a SPDE of ~ 20 % at 850 nm and ~ 5 % at 1550 nm. However, in applications such as optical networks of field-based systems they may not be practical due to the low temperatures at which they must be operated, although ~ 4 K is achievable with the availability of closed-cycle refrigerators and is certainly more practical than 100 mK which requires an adiabatic demagnetisation refrigerator. SSPDs must also be shielded from thermal radiation longer than 2.5 µm since this leads to a higher DCR.

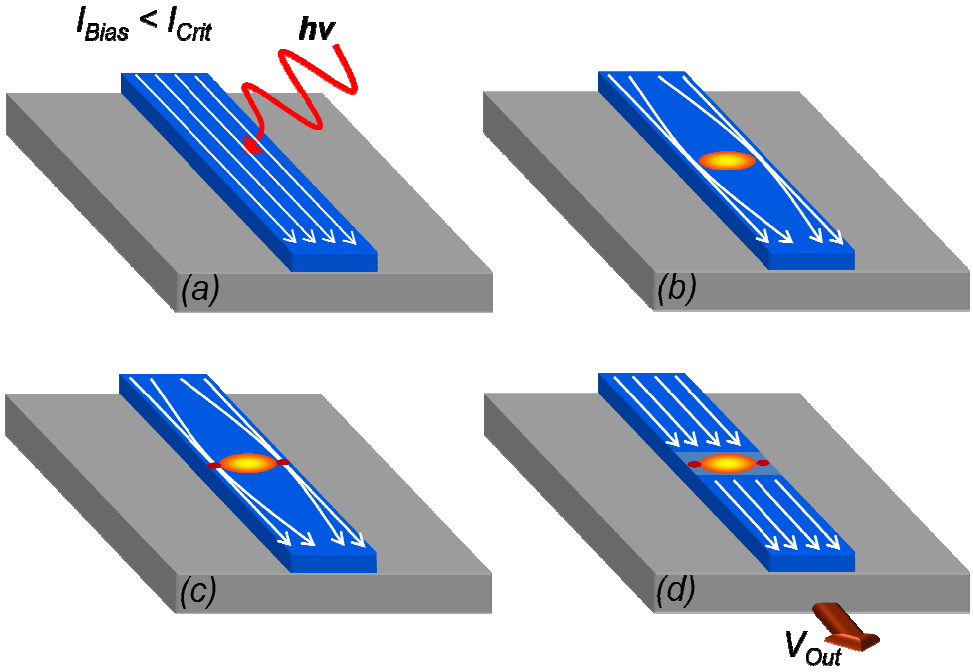

Figure 2.26. NbN SSPD schematic of operation. (a) An incoming photon is absorbed by the wire which is DC biased (I_{Bias}) just below its critical current (I_{Crit}). (b) The absorption process causes a localised "hot-spot" perturbing the current and redirecting it around the hotspot. (c) The excited electrons spread from the initial point of absorption causing the supercurrent to be diverted through the edge regions. (d) The current density in these edge regions exceeds the critical current density causing a resistive strip across the width of the wire resulting in a measurable voltage pulse at the detector output. As the wire returns to its operating temperature, the hot-spot shrinks, removing the resistive barrier and re-enters its superconducting state.

Since their introduction, a large research effort has been put into increasing the device efficiency using various methods. One of the most promising is that of using the device within an optical cavity [68] [69]. Photons that are not absorbed on the first pass enter the optical cavity formed by the metallic mirror and the dielectric SiO2 layer which has a thickness of λ/4. Such devices as shown in Figure 2.27 have shown detection efficiencies in excess of 50 % at 1550 nm at a temperature of 1.8 K. The 50 % quoted SPDE is the efficiency of the device itself, not including the coupling losses before the light reaches the detector, whereas the 1 – 2 % efficiency of the device used in Chapter 6 is the *system* SPDE, including coupling losses etc.

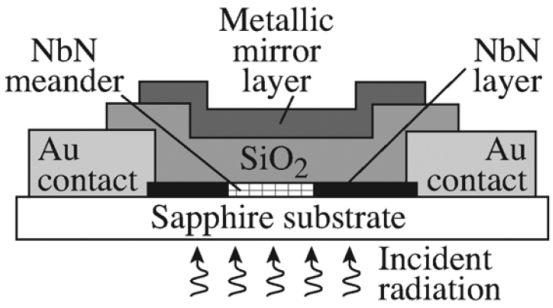

Figure 2.27. SSPD with microcavity resonator where the SiO_2 layer has a thickness of λ/4 [69].

2.3.8.3 Superconducting Tunnel Junction Detector

Superconducting tunnel junctions (STJs) have been used for many years as a photon detector in the X-ray region of the electromagnetic spectrum and for spectroscopy since these detectors are energy-resolving [70] [71]. They have been demonstrated to work at visible wavelengths [72] [73] and are of particular interest to astronomers as they may replace CCDs as the astronomical detector of choice due to their energy resolving properties in contrast to Si CCDs. An STJ comprises two thin superconducting (usually niobium, tantalum or hafnium) film layers separated by a thin insulating layer, as in Figure 2.28. When operated below the superconductor's critical temperature, a photon causes the breaking of many Cooper pairs. A small voltage is applied across the junction so that the electrical charge proportional to the energy of the incoming photon can be extracted and subsequently recorded. To suppress the Josephson current, a magnetic field parallel to the barrier is employed.

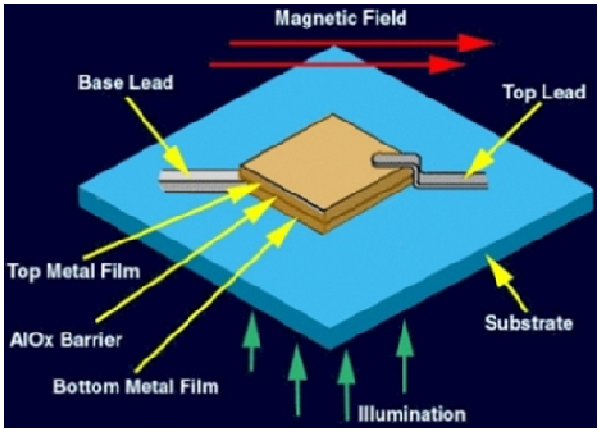

Figure 2.28. STJ schematic [74]. The superconducting films at the top and bottom are separated by a thin insulating layer. Incoming photons break many Cooper pairs. A small voltage is applied across the two terminals to allow the extraction of the product electrons whose total energy is proportional to that of the absorbed photon. A magnetic field suppresses the Josephson current.

The authors of [73] reported a QE of ~ 50 % over a wavelength range of 200 – 500 nm with a spectral resolution of 45 nm. The count rates were limited to detecting single-photons at 2.5 kHz.

2.4 Conclusion

In this Chapter a brief review of the TCSPC technique has been presented including a description of the appropriate conditions under which measurements should be taken.

A review of single-photon detectors was also detailed. This covered many differing device types and an explanation of the advantages and disadvantages of each type given. PMTs are large area devices which is beneficial to facilitate easy aligning, yet their high operating voltages, poor detection efficiencies (particularly in the near infrared) and large packaging dimension are disadvantages. MCPs are advantageous in that they are two-dimensional devices and are used in LIDAR applications but suffer from similar low detection efficiencies at longer wavelengths like PMTs.

SPADs were then introduced and their method of operation explained. Si SPADs are currently the highest performance single-photon detector in terms of SPDE at visible wavelengths. The differences between thick and shallow junction Si SPADs were reported along with the trade-off between timing jitter and SPDE. A brief description of

current InGaAs/InP SPADs available for near infrared single-photon counting was given and will be followed by a more in-depth study of these devices in the next Chapter. Ge SPADs were reported and the SPDE of various detectors compared. Different quenching methods and circuits were briefly reviewed and their associated advantages discussed.

SiPMs were reviewed. Their large active areas make them ideal candidates to replace PMTs in some applications, especially since they are also capable of photon-number resolution. The disadvantages of many SPADs acting on the same load is that the DCR of the SiPM is the addition of the DCR of each single pixel, although this can be limited by cooling the device.

Frequency up-conversion by the sum-mixing of a signal IR source with a higher energy escort beam in a non-linear PPLN crystal enables the conversion of, for example, a 1550 nm photon to a photon of a visible wavelength which can then be detected by a standard Si SPAD thus taking advantage of its high SPDE, low jitter, little afterpulsing and high count rate. The DCR of the system is limited by the parasitic nonlinear interactions within the PPLN crystal like spontaneous Raman scattering, parametric fluorescence, and second harmonic generation from the escort beam. Overall system efficiencies of 46 % were reported along with practical demonstrations in QKD.

VLPCs operated at a temperature of 6.4 K showed a system QE of ~ 70 % with a DCR of 2 x 10^4 c/s with a 1 mm detector diameter and count rates up to 10^7 c/s and no afterpulsing. The main disadvantage is that the VLPC has to be carefully shielded from room temperature radiation to attain a low DCR.

Quantum dot based devices have shown promising performance in the visible range, with SPDE reported up to > 60 %. Unfortunately, the only reported device at telecoms wavelengths (1.3 μm) showed a low SPDE of 0.35 % with prohibitively long reset times.

Single-photon detection with superconducting detectors is a fast emerging technology area. TES have an extremely high SPDE of > 95% and a very low DCR, however, they are made less favourable by the long reset time and slow timing jitter. Niobium nitride superconducting single-photon detectors, however, are comparatively fast devices, both in terms of reset time and timing jitter. Early examples showed poor SPDEs, yet more recently with the use of resonant microcavities, SPDEs of up to 50 % were reported.

Finally, STJs capable of working at visible wavelengths showed a QE of ~ 50 % and energy resolution although they were limited to a maximum count rate of 2.5 kHz.

The main problem with quantum dot devices and superconducting detectors is the temperature at which they must be operated – around 4 K or below – requiring either closed cycle refrigerator cooling, liquid He in a cryostat or adiabatic refrigeration. Whilst this is feasible in a laboratory setup, the implementation and integration of such devices in a commercial setup may be problematic and expensive.

2.5 References

[1] G.S. Buller, S.J. Fancey, J.S. Massa, A.C. Walker, S. Cova, and A. Lacaita, *Time-resolved photoluminescence measurements of InGaAs – InP multiple-quantum-well structures at 1.3 μm wavelengths by use of germanium single-photon avalanche photodiodes*, Applied Optics, **35** (6), 916 - 921 (1996)

[2] J.A. Timpson, D. Sanvitto, A. Daraei, P.S.S. Guimaraes, H. Vinck, S. Lam, D.M. Whittaker, M.S. Skolnick, A.M. Fox, C.Y. Hu, Y.-L. D. Ho, R. Gibson, J.G. Rarity, S. Pellegrini, K.J. Gordon, R.E. Warburton, G.S. Buller, A. Tahraoui, P.W. Fry, M. Hopkinson, *Single photon sources based upon single quantum dots in semiconductor microcavity pillars*, Journal of Modern Optics, **54** (2), 453 - 465 (2007)

[3] C.H. Bennett and G. Brassard, *Quantum cryptography: public key distribution and coin tossing*, Proceedings of the IEEE international conference on computers, system, and signal processing, Bangalore, India, 175 - 179 (1984)

[4] P.A. Hiskett, G. Bonfrate, G.S. Buller and P.D. Townsend, *Eighty kilometre transmission experiment using an InGaAs/InP SPAD-based quantum cryptography receiver operating at 1.55 μm, Journal of Modern Optics*, **48** (13), 1957 - 1966 (2001)

[5] J.S. Massa, A.M. Wallace, G.S. Buller, S.J. Fancey and A.C. Walker, *Laser depth measurement based on time-correlated single photon counting*, Optics Letters, **22** (8), 543 - 545 (1997)

[6] A.M. Wallace, G.S. Buller and A.C. Walker, *3-D Imaging and ranging by time-correlated single-photon counting*, Computing and Control Engineering Journal, **12**, 157 - 168 (2001)

[7] M.A. Albota, R.M. Heinrichs, D.G. Kocher, D.G. Fouche, B.E. Player, M.E. O'Brien, B.F. Aull, J.J. Zayhowski, J. Mooney, B.C. Willard and R.R. Carlson, *Three-dimensional imaging laser radar with a photon-counting avalanche photodiode array and microchip laser*, Applied Optics, **41** (36), 7671 - 7678 (2002)

[8] R.E. Warburton, A. McCarthy, A.M. Wallace, S. Hernandez-Marin, S. Cova, R.A. Lamb and G.S. Buller, *Enhanced performance photon-counting time-of-flight sensor*, Optics Express, **15** (2), 423 - 429 (2007)

[9] A.L. Lacaita, P.A. Francese, and S. Cova, *Single-photon optical-time domain reflectometer at 1.3 μm with 5 cm resolution and high sensitivity*, Optics Letters, **18** (13), 1110 - 1112 (1993)

[10] D.V. O'Connor and D. Phillips, *Time-Correlated Single Photon Counting*, Academic, London (1984)

[11] W. Becker, *Advanced Time-Correlated Single Photon Counting*, Springer, Berlin, Germany (2005)

[12] P.B. Coates, *The correction for photon 'pile-up' in the measurement of radiative lifetimes*, Journal of Physics E: Scientific Instruments, **1**, 878 - 879 (1968)

[13] R. Foord, R. Jones, C.J. Oliver, and E.R. Pike, *The Use of Photomultiplier Tubes for Photon Counting*, Applied Optics, **8** (10), 1975 - 1989 (1969)

[14] Burle Industries Inc., *Photomultiplier Handbook*, (1980)

[15] S.J. Fancey, *Single-photon avalanche diodes for time-resolved photoluminescence measurements in the near infrared*, PhD thesis, Heriot-Watt University (1996)

[16] G.A. Motron, *Photon Counting*, Applied Optics, **7** (1), 1 - 10 (1968)

[17] J.P. Rodman, and H.J. Smith, *Tests of photomultipliers for astronomical pulse-counting applications*, Applied Optics, **2** (2), 181 - 186 (1963)

[18] G.S. Buller and J.S. Smith, *Handbook of Laser Technology and Applications: Principles*, Institute of Physics Publishing, **1**, 255 - 257 (2004)

[19] http://sales.hamamatsu.com/en/products/electron-tube-division/detectors/photomultiplier-tubes.php?src=hp (date accessed 06/08)

[20] http://sales.hamamatsu.com/index.php?id=13195879 (date accessed 01/08)

[21] http://sales.hamamatsu.com/en/products/electron-tube-division/detectors/photomultiplier-modules/part-h10330-75.php (date accessed 01/08)

[22] J.J. Degnan, *Photon-counting multikilohertz microlaser altimeters for airborne and spaceborne topographic measurements*, Journal of Geodynamics **34** (3 - 4), 503 - 549, (2002)

[23] http://www.hpk.co.jp/Eng/products/ETD/mcpe/mcpe.htm (date accessed 01/08)

[24] S. Cova, G. Ripamontia, and A. Lacaita, *Avalanche semiconductor detector for single optical photons with a time resolution of 60 ps*, Nuclear Instruments and Methods in Physics Research Section A: Accelerators, Spectrometers, Detectors and Associated Equipment, **253** (3), 482 - 487 (1987)

[25] C.E. Webb, and J.D.C. Jones, *Handbook of laser technology and applications*, Institute of Physics Publishing (2003)

[26] A. Lacaita, M. Mastrapasqua, M. Ghioni, and S. Vanoli, *Observation of avalanche propagation by multiplication assisted diffusion in p-n junctions*, Applied Physics Letters, **57** (5), 489 - 491 (1990)

[27] R.H. Haitz, *Model for the electrical behaviour of a microplasma*, Journal of Applied Physics, **35** (5), 1370 - 1376 (1964)

[28] S. Cova, A. Longoni, and A. Andreoni, *Towards picoseconds resolution with single-photon avalanche diodes*, Review of Scientific Instruments, **52** (3), 408 - 412 (1981)

[29] M. Ghioni, A. Giudice, S. Cova and F. Zappa, *High-rate quantum key distribution at short wavelength: performance analysis and evaluation of silicon*

single-photon avalanche diodes, Journal of Modern Optics, **50** (14), 2551 - 2269 (2003)

[30] M. Dandin, N. Nelson, V. Saveliev, J. Honghao, P. Abshire, and I. Weinberg, *Single Photon Avalanche Detectors in Standard CMOS*, Sensors 2007 IEEE, **Oct**, 585 - 588 (2007)

[31] L. Pancheri, and D. Stoppa, *Low-Noise CMOS single-photon avalanche diodes with 32 ns dead time*, 37th European Solid State Device Research Conference, 2007. **Sept**, 362 - 365, (2007)

[32] C. Niclass, M. Gersbach, R. Henderson, L. Grant, and E. Charbon, *A Single Photon Avalanche Diode Implemented in 130-nm CMOS Technology*, IEEE Journal of Selected Topics in Quantum Electronics, **13** (4), 863 - 869 (2007)

[33] S. Pellegrini, *InGaAs/InP single-photon avalanche diodes*, Thesis submitted for PhD, Heriot-Watt University (2005)

[34] P.A. Hiskett, G.S. Buller, A.Y. Loudon, J.M. Smith, I. Gontijo, A.C. Walker, P.D. Townsend, and M.J. Robertson, *Performance and design of InGaAsInP photodiodes for single-photon counting at 1.55 μm*, Applied Optics, **39** (36), 6818 - 6829 (2000)

[35] G. Ribordy, N. Gisin, O. Guinnard, D. Stucki, M. Wegmuller and H. Zbinden, *Photon counting at telecom wavelengths with commercial InGaAs/InP avalanche photodiodes: current performance*, Journal of Modern Optics, **51** (9-10), 1381 - 1398 (2004)

[36] X. Li, P.L. Voss, J.E. Sharping, and P. Kumar, *Optical-Fiber Source of Polarization-Entangled Photons in the 1550 nm Telecom Band*, Physical Review Letters, **94**, 053601 (2005)

[37] J. Chen, K.F. Lee, C. Liang, and P. Kumar, *Fiber-based telecom-band degenerate-frequency source of entangled photon pairs*, Optics Letters, **31** (18), 2798 - 2800 (2006)

[38] M.A. Itzler, R. Ben-Michael, C.F. Hsu, K. Slomkowski, A. Tosi, S. Cova, F. Zappa, and R. Ispasoiu, *Single photon avalanche diodes (SPADs) for 1.5μm*

photon counting applications, Journal of Modern Optics, **54** (2), 283 - 304 (2007)

[39] S. Verghese, J.P. Donnelly, E.K. Duerr, K.A. McIntosh, D.C. Chapman, C.J. Vineis, G.M. Smith, J.E. Funk, K.E. Jensen, P.I. Hopman, D.C. Shaver, B.F. Aull, J.C. Aversa, J.P. Frechette, J.B. Glettler, Z.L. Liau, J.M. Mahan, L.J. Mahoney, K.M. Molvar, F.J. O'Donnell, D.C. Oakley, E.J. Ouellette, M.J. Renzi, and B.M. Tyrrell, *Arrays of InP-based Avalanche Photodiodes for Photon Counting*, IEEE Journal of selected topics in Quantum Electronics, **13** (4), 870 - 886 (2007)

[40] M. Liu, C. Hu, X. Bai, X. Guo, J.C. Campbell, Z. Pan, and M.M. Tashima, *High-Performance InGaAs/InP Single-Photon Avalanche Photodiode*, IEEE Journal of Selected Topics in Quantum Electronics, **13** (4), 887 - 894 (2007)

[41] P.C.M. Owens, J.G. Rarity, P.R. Tapster, D. Knight and P.D. Townsend, *Photon counting with passively quenched germanium avalanche*, Applied Optics, **33**, (30), 6895 - 6901 (1994)

[42] A. Lacaita, P.A. Francese, F. Zappa and S. Cova, *Single-photon detection beyond 1 micrometer: performance of commercially available germanium photodiodes*, Applied Optics, **33** (30), 6902 - 6918 (1994)

[43] S. Cova, M. Ghioni, A. Lacaita, C. Samori, and F. Zappa, *Avalanche Photodiodes and Quenching Circuits for Single-Photon Detection*, Applied Optics, **35** (12), 1956 - 1976 (1996)

[44] P. Buzhan, B. Dolgoshein, L. Filatov, A. Ilyin, V. Kantzerov, V. Kaplin, A. Karakash, F. Kayumov, S. Klemin, E. Popova, and S. Smirnov, *Silicon photomultiplier and its possible applications*, Nuclear Instruments and Methods in Physics Research A, **504**, 48 - 52 (2003)

[45] SensL Technical Note, *Introduction to the Silicon Photomultiplier*, Rev. 1, www.sensl.com/pdfs/SPM_Tech_App_Notes/TN_Intro.pdf (date accessed 07/08)

[46] G.D. Boyd, and D.A. Kleinman, *Parametric interaction of focused Gaussian light beams*, Journal of Applied Physics, **39** (8), 3597 - 3639 (1968)

[47] M.A. Albota, and F.N.C. Wong, *Efficient single-photon counting at 1.55 μm via frequency upconversion*, Quantum Electronics and Laser Science, QELS. Postconference Digest (2003)

[48] C. Langrock, E. Diamanti, R.V. Roussev, Y. Yamamoto, M.M. Fejer and H. Takesue, *Highly efficient single-photon detection at communication wavelengths by use of upconversion in reverse-proton-exchanged periodically poled LiNbO3 waveguides*, Optics Letters, **30** (13), 1725 - 1727 (2005)

[49] A.P. Vandevender, and P.G. Kwiat, *High efficiency single photon detection via frequency up-conversion*, Journal of Modern Optics, **51** (9 - 10), 1433 - 1445 (2004)

[50] R.T Thew, S. Tanzilli, L. Krainer, S.C Zeller, A. Rochas, I. Rech, S. Cova, H. Zbinden, and N. Gisin, *Low jitter up-conversion detectors for telecom wavelength GHz QKD*, New Journal of Physics, **8** (32), 1 - 12 (2006)

[51] M.D. Petroff, M.G. Stapelbroek, and W.A. Kleinhans, *Detection of individual 0.4 – 28 μm wavelength photons via impurity-impact ionization in a solid-state photomultiplier*, Applied Physics Letters, **51** (6), 406 - 408 (1987)

[52] D. Adams, M. Adams, B. Baumbaugh, I. Bertram, A. Bross, D. Casey, S. Chang, M. Chung, C. Cooper, C. Cretsinger, R. Demina, G. Fanourakis, T. Ferbel, S. Grünendahl, J. Hinson, B. Howell, H. Johari, J. S. Kang, C. L. Kim, S. K. Kim, D. Koltick, F. Lobkowicz, S. Margulies, J. Moromisato, M. Narain, C. H. Park, S. Reucroft, Y. M. Park, R. Ruchti, J. Solomon, E. VonGoeler, J. Warchol, M. Wayne, E. Won, Y. Yu, *First Large Sample Study of Visible Light Photon Counters (VLPC's)*, Nuclear Physics B - Proceedings Supplements, **44** (1), 340 - 348 (1995)

[53] S. Takeuchi, J. Kim, Y. Yamamoto, and H.H Hogue, *Development of a high-quantum-efficiency single-photon counting system,* Applied Physics Letters, **74** (8), 1063 - 1065 (1999)

[54] J. Kim, S. Takeuchi, Y. Yamamoto, and H.H Hogue, *Multiphoton detection using visible light photon counter*, Applied Physics Letter, **74** (7), 902 - 904 (1999)

[55] B.E. Kardynal, A.J. Shields, M.P. O'Sullivan, N.S. Beattie, I. Farrer, D.A. Ritchie and K. Cooper, *Detection of single photons using a field effect transistor with a layer of quantum dots*, Measurement Science and Technology, **13**, 1721 - 1726 (2002)

[56] B.E. Kardynal, S.S. Hees, A.J. Shields, C. Nicoll, I. Farrer, and D.A. Ritchie, *Photon number resolving detector based on a quantum dot field effect transistor*, Applied Physics Letters, **90** (18), 181114 (2007)

[57] Z. Yuan, B.E. Kardynal, R.M. Stevenson, A.J. Shields, C. Lobo, K. Cooper, N.S. Beattie, D.A. Ritchie, and M. Pepper, *Electrically driven single-photon source*, Science, **295**, 102 - 105 (2002)

[58] M.A. Rowe, E.J. Gansen, M. Greene, R.H. Hadfield, T.E. Harvey, M.Y. Su, S.W. Nam, and R.P. Mirin, and D. Rosenberg, *Single-photon detection using a quantum dot optically gated field-effect transistor with high internal quantum efficiency*, Applied Physics Letters, **89**, 253505 (2006)

[59] J.C. Blakesley, P. See, A.J. Shields, B.E. Kardynal, P. Atkinson, I. Farrer and D.A. Ritchie, *Efficient single photon detection by quantum dot resonant tunnelling diodes,* Physics Review Letters, **94** (6), 067401 (2005)

[60] H.W. Li, B.E. Kardynał, P. See, A.J. Shields, P. Simmonds, H.E. Beere, and D.A. Ritchie, *Quantum dot resonant tunneling diode for telecommunication wavelength single photon detection*, Applied Physics Letters, **91**, 073516 (2007)

[61] R. Romestain, B. Delaet, P. Renaud-Goud, I. Wang, Jorel, J-C. Villegier, and J-Ph. Poizat, *Fabrication of a superconducting niobium nitride hot electron bolometer for single-photon counting*, New Journal of Physics, **6**, 129, (2004)

[62] D. Rosenberg, A.E. Lita, A.J. Miller, and S. Nam, *Noise-free high-efficiency photon-number-resolving detectors*, Physical Review A, **71**, 061803 (2005)

[63] A. E. Lita, A. J. Miller, and S. W. Nam, *Counting near-infrared single-photons with 95% efficiency*, Optics Express **16** (5), 3032 - 3040 (2008)

[64] P.A. Hiskett, D. Rosenberg, C.G. Peterson, R.J. Hughes, S. Nam, A.E. Lita, A.J. Miller and J.E. Nordholt, *Long-distance quantum key distribution in optical fibre*, New Journal of Physics, **8**, 193 (2006)

[65] G.N. Gol'tsman, A.D. Semenov, Y.P. Gousev, M.A. Zorin, I.G. Gogidze, E.M. Gershenzon, P.T. Lang, W.J. Knott, K.F. Renk, *Sensitive picosecond NbN detectors for radiation from millimeter wavelengths to visible light*, Superconductor Science and Technology, **4** (9), 453 - 456 (1991)

[66] G.N. Gol'tsman, O. Okunev, G. Chulkova, A. Lipatov, A. Semenov, K. Smirnov, B. Voronov, and A. Dzardanov, *Picosecond superconducting single-photon optical detector*, Applied Physics Letters, **79** (6), 705 - 707 (2001)

[67] K.S. Il'in, M. Lindgren, M. Currie, A.D. Semenov, G.N. Gol'tsman, and Roman Sobolewski, *Picosecond hot-electron energy relaxation in NbN superconducting photodetectors*, Applied Physics Letters, **76** (19), 2752 - 2754 (2000)

[68] K.M. Rosfjord, J.K.W. Yang, E.A. Dauler, A.J. Kerman, V. Anant, B.M. Voronov, G.N. Gol'tsman, and K.K. Berggren, *Nanowire single-photon detector with an integrated optical cavity and anti-reflection coating*, Optics Express **14** (2), 527 - 534 (2006)

[69] G.N. Gol'tsman, O. Minaeva, A. Korneev, M. Tarkhov, I. Rubtsova, A. Divochiy, I. Milostnaya, G. Chulkova, N. Kaurova, B. Voronov, D. Pan, J. Kitaygorsky, A. Cross, A. Pearlman, I. Komissarov, W. Slysz, M. Wegrzecki, P. Grabiec, and R. Sobolewski, *Middle-infrared to visible-light ultrafast superconducting single-photon detectors*, IEEE Transactions on applied superconductivity, **17** (2), 246 - 251 (2007)

[70] J.B. le Grand, C.A. Mears, L.J. Hiller, M. Frank, S.E. Labov, H. Netel, D. Chow, S. Friedrich, and M.A. Lindeman, *A superconducting tunnel junction x-ray detector with performance limited by statistical effects*, Applied Physics Letters, **73** (9), 1295 - 1297 (1998)

[71] P.A.J. de Korte, Proceedings of ESA Symposium on Photon Detectors for Space Instrumentation, ESTEC, Noordwijk, The Netherlands (1992)

[72] N. Rando, A. Peacock, M.A.C. Perryman, P. Hübner, A. van Dordrecht, P. Videler, and J. Lumley, *UV to IR photon detection using superconducting tunnel junctions*, Journal of Low Temperature Physics, **93** (3 - 4), 659 - 664 (1993)

[73] A. Peacock, P. Verhoeve, N. Rando, A. van Dordrecht, B.G. Taylor, C. Erd, M.A.C. Perryman, R. Venn, J. Howlett, D.J. Goldie, J. Lumley, and M. Wallis,

Single optical photon detection with a superconducting tunnel junction, Nature, **381**, 135 - 137 (1996)

[74] http://sci.esa.int/science-e/www/object/index.cfm?fobjectid=33525
(date accessed 06/08)

Chapter 3 - InGaAs/InP Single-Photon Avalanche Diodes: Device Structure, Modelling, Growth, Operation and Performance

3.1 Introduction

In the previous chapter, various single-photon detectors were introduced and some of their advantages and disadvantages discussed. InGaAs/InP single-photon avalanche diodes (SPADs) have been designed, modelled, and characterised within the Photon Counting Group at Heriot-Watt University. They were chosen as the primary detector to investigate due to their promising performance, practicality, and ease of integration in various TCSPC setups. Since the late 1990's the photon counting group have been characterising and employing InGaAs/InP APDs in Geiger-mode in order to extend the operating wavelength range of TCSPC systems beyond the silicon cut-off of $\lambda \sim 1$ μm. A summary of relevant work performed by previous group members will be given, followed by the results of device characterisation that have been undertaken by the author. A brief description of the growth process will also be given.

3.2 Device Structure, Modelling and Growth

The devices studied in this thesis are of planar geometry and are based on the separate absorption, grading and multiplication region (SAGM) APDs [1], [2] commonly used for applications requiring internal gain of weak input optical signals. An example of this structure is shown in Figure 3.1, displayed with the electric field profile on the right. The SPADs discussed in this Thesis make use of this SAGM structure but have subtle enhancements specifically designed and modelled for use at electric fields above avalanche breakdown in Geiger-mode, and also at the low operating temperatures necessary to avoid a prohibitively high DCR.

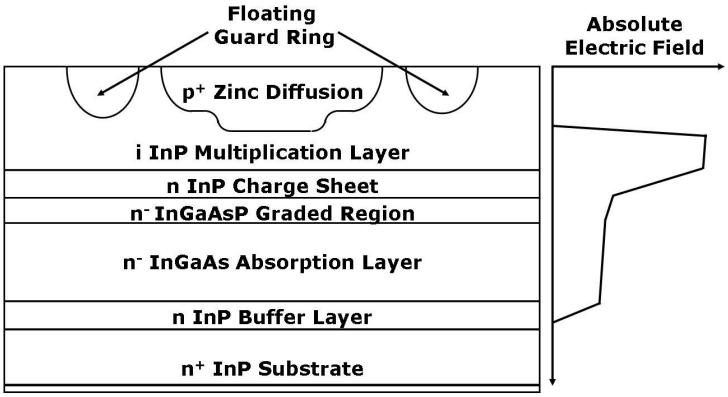

Figure 3.1. Cross-section of an InGaAs/InP SPAD structure and absolute electric field (right) [3].

In this structure the optical absorption occurs in the $In_{0.53}Ga_{0.47}As$ absorption layer, which is not suitable for multiplication, since tunnelling in this narrow-gap material [4] would take place at a lower electric field than that required for impact ionisation. Instead, the multiplication takes place in the wider-gap InP. The mechanism for photon absorption was demonstrated in Chapter 2 for a silicon SPAD. Figure 3.2 shows the absorption process and movement of the photo-generated electron-hole pair in an InGaAs/InP SPAD according to the band structure under reverse-biased conditions.

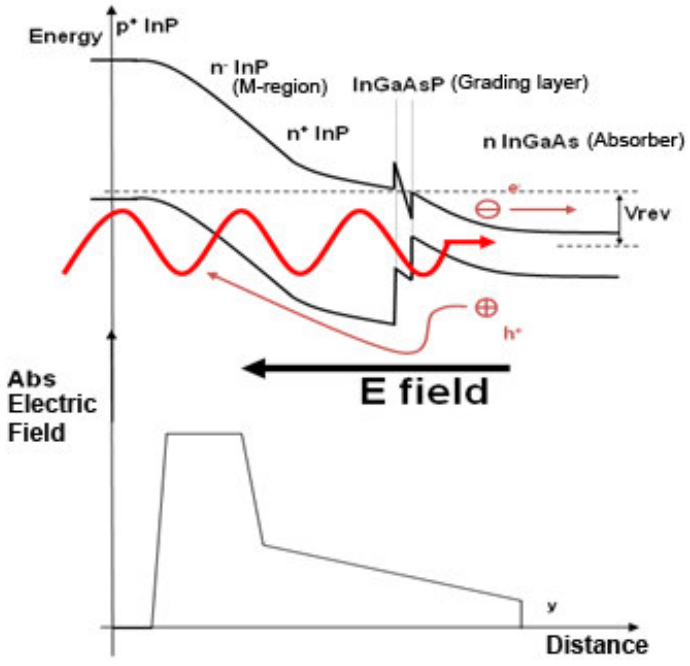

Figure 3.2. Band structure of an InGaAs/InP SPAD under reverse bias conditions (of magnitude V_{rev}) shown with the associated electric field profile for clarity.

An incoming photon is absorbed in the n-type InGaAs, creating an electron-hole pair. Under the electric field, the electron is swept towards the rear contact. The photo-generated hole must pass into the InP multiplication region where it undergoes avalanche multiplication via impact ionisation due to the acceleration it experiences from the electric field. In order to pass into the high-field InP, the hole must first overcome the valence band discontinuity between the narrow-gap InGaAs and the wide-gap InP. For this reason, a quaternary layer of InGaAsP is grown between to provide an easier passage for the hole. The step between layers shown in Figure 3.2 is exaggerated for clarity.

As previously stated, the structure is based upon the SAGM linear multiplication APD structure except for three key features. Firstly, to reduce the DCR due to thermally generated carriers, the device must be able to work at low temperatures, preferably capable of operating at < 150 K. This requirement is satisfied by ensuring the punch-through and breakdown voltages are separated by at least 30 V at room temperature since the breakdown voltage decreases as the temperature is lowered, whereas the punch-through voltage remains relatively unchanged with temperature. This meant that even at low temperatures, the absorption region would be fully depleted before the onset of avalanche breakdown. Secondly, the electric fields involved in a SPAD device are higher than those required for a linear multiplication device. This may result in a higher tunnelling current if care is not taken to avoid a high field in the InGaAs, therefore the device design must take into account this potentially adverse factor. Finally, the mask design through which the zinc p-type well is diffused needed to incorporate smaller diameter devices to reduce the active volume which decreases the DCR. A zinc diffusion was chosen to form the p-type region, giving a planar device, based on previous studies on linear multiplication devices operated in Geiger mode performed by a number groups, including our own, since they consistently showed lower DCRs [5] [6] [7]. Referring to Figure 3.1, it can be seen that there is a section of the zinc diffusion that extends further into the structure. This was first suggested by Liu *et al.* [2] and is the result of two separate zinc diffusion processes through different mask sets. This double-diffusion reduces the curvature at the edge of the device, consequently reducing the likelihood of edge-breakdown. Edge-breakdown is, as the name suggests, when the device exhibits preferential breakdown at the edge of the active region [8]. This results in a lower field in the centre of the region in which the device is optically addressed, resulting in a much reduced single-photon detection efficiency. Using a zinc diffusion to form the p-type well also meant that the critical and difficult sidewall

passivation of mesa structures could be avoided: such a process may lead to increased surface defects and generation-recombination centres leading to high dark currents and higher dark count rates. Etch and regrowth techniques [9] were also avoided to reduce interface states that may contribute to higher dark count and afterpulsing levels.

Before the structures were grown, 2-dimensional electric field profiling was accomplished by means of computer simulation and modelling using an adapted version of a commercially-available software package, ISE. This program was originally designed for modelling silicon structures prior to the growth to avoid costly production errors, however, the software was modified so that III-V semiconductor structures could be modelled. This work was completed previously by Dr Sara Pellegrini and a full explanation of the modelling can be found in her PhD Thesis [10]. The purpose of the modelling was to ascertain the values of breakdown and punch-through voltages, to calculate the value of the electric field in both absorption and multiplication regions, and also to find the most suitable junction geometry to avoid edge-breakdown.

Examples of the results given by the ISE software are shown in Figure 3.3 and 3.4.

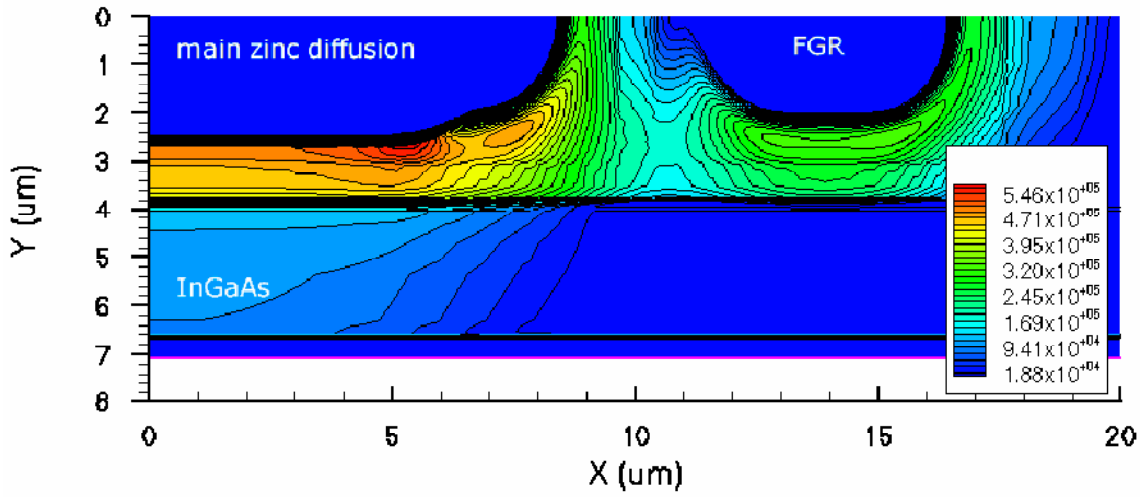

Figure 3.3. Electric field profile of an InGaAs/InP SPAD at breakdown. The legend shows the electric field in Vcm^{-1}. The red represents the area of highest electric field, and in this example shows slight evidence of edge-breakdown [10].

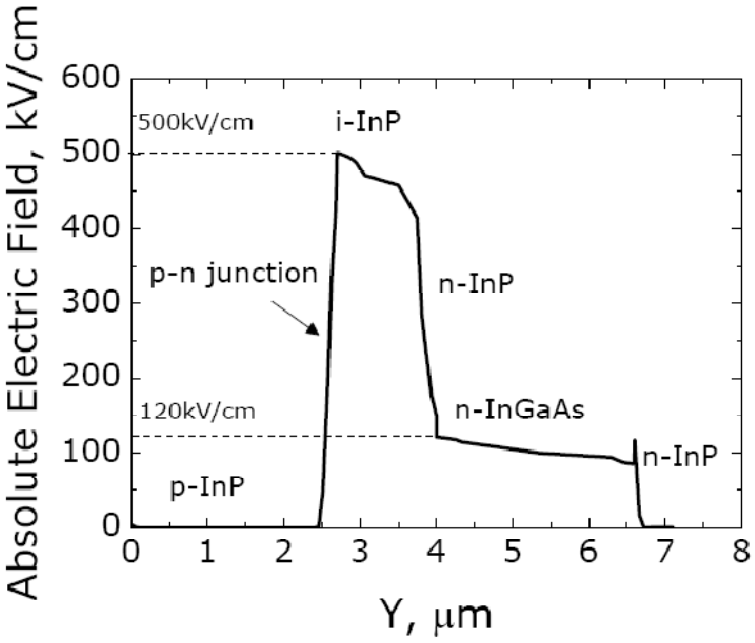

Figure 3.4. Electric field profile of an InGaAs/InP SPAD at breakdown along the centre of the device [10].

As demonstrated in Figure 3.4, the software enables the user to calculate the absolute electric field through the device. This is crucial so the correct field can be achieved in the InGaAs to avoid tunnelling.

The device material was grown by metal organic chemical vapour deposition (MOCVD) at the University of Sheffield in the Centre for III-V technologies.

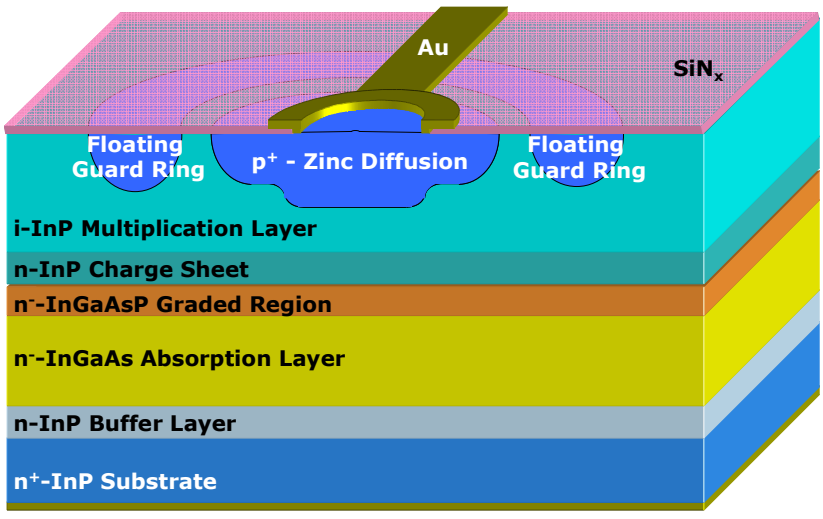

Figure 3.5. Three-dimensional representation of InGaAs/InP SPAD cross-section.

Figure 3.5 shows a 3-D representation of an InGaAs SPAD cross-section which consists of a 2.5 μm thick layer of lightly n-doped InGaAs for efficient absorption of photons at a 1.55 μm wavelength and a 1 μm thick nominally undoped InP in which multiplication takes place. To reduce the electric field from 500 $kVcm^{-1}$ in the InP multiplication region to 120 $kVcm^{-1}$ in the InGaAs (as shown in Figure 3.4) a 300 nm thick InP charge sheet layer n-doped at 6 x 10^{16} cm^{-3} was grown. For the graded region which smoothes the valence band discontinuity two different devices were designed and grown as shown in Figure 3.6. Firstly, with a graded region consisting of one InGaAsP quaternary with an exactly intermediate bandgap between the InGaAs and InP layers which will be referred to as SPAD-1Q. Secondly, SPAD-3Q which has a graded region composed of three sublayers of stepped bandgap. Attempts were also made to grow a structure with a continually varying bandgap although these were unsuccessful due to growth control issues.

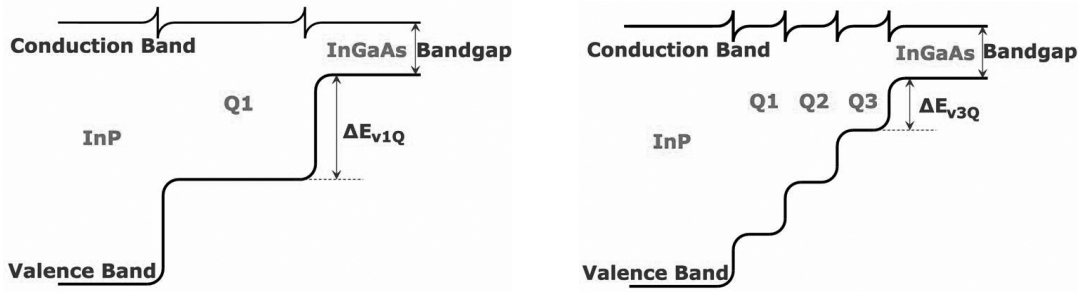

Figure 3.6. SPAD 1Q (left) and SPAD 3Q (right) band-structures.

The effects of the different graded regions will be summarised in the following sections.

Finally, in Figures 3.7 and 3.8, images taken under an optical microscope are shown. Figure 3.7 shows a fully processed and bonded chip demonstrating the differing sizes of device and the configurations of floating guard rings.

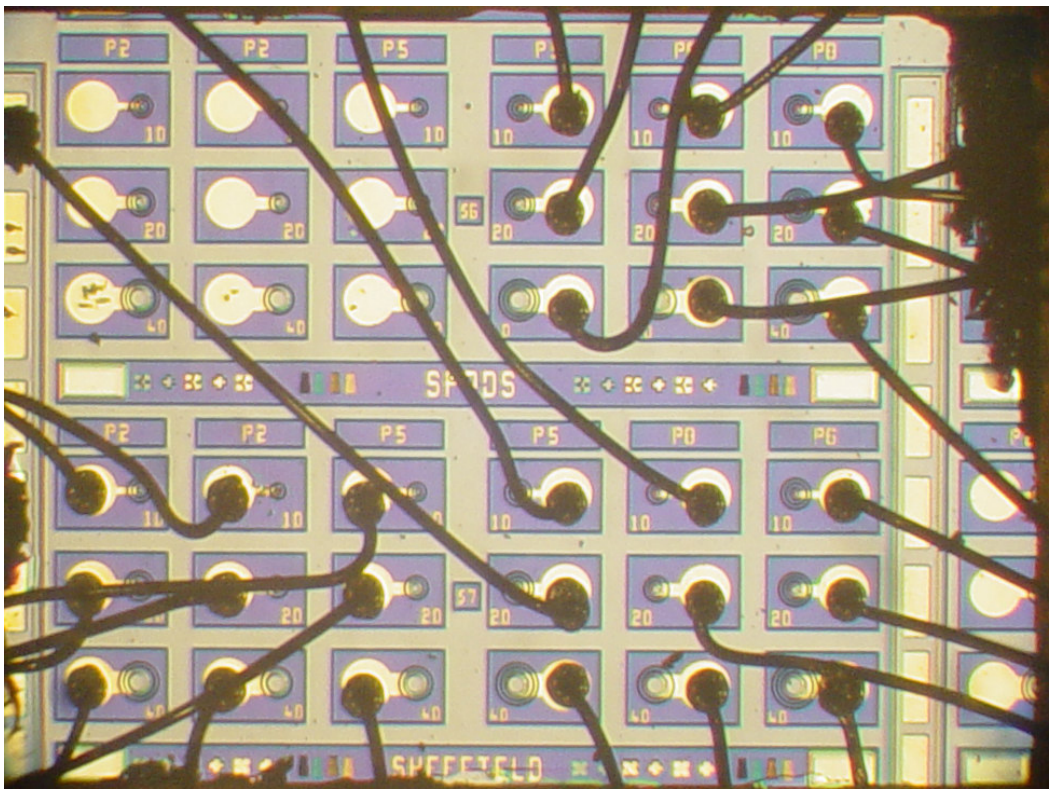

Figure 3.7. Microscope image of a fully processed chip of SPAD-3Q devices.

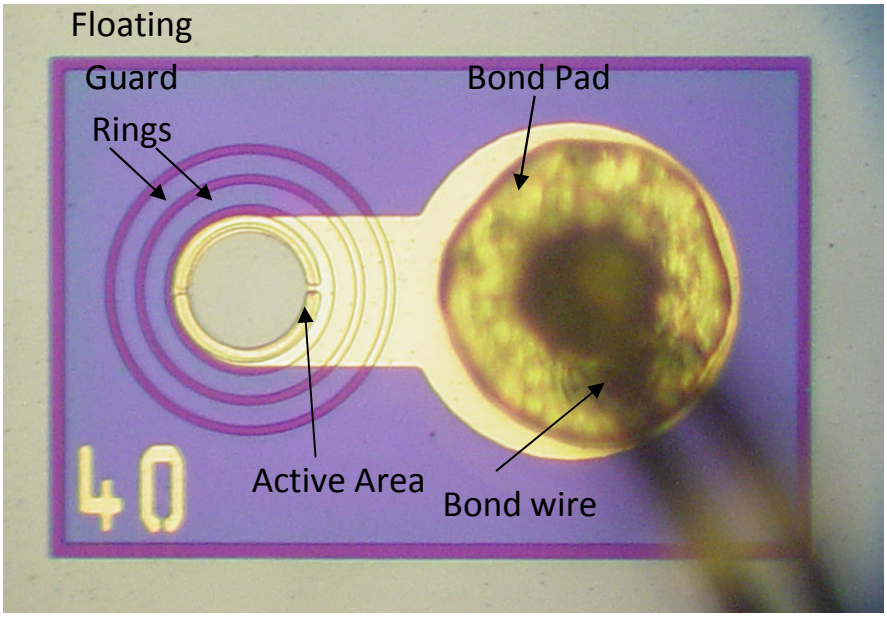

Figure 3.8. Microscope image of a 40 μm diameter SPAD-3Q devices detailing floating guard rings, active area, bond wire and bond pad.

3.3 Device Characteristics and Performance

The first property to be measured of any device is the reverse current-voltage characteristic, or I-V for short. From this plot, various key aspects can be ascertained as shown in Figure 3.9.

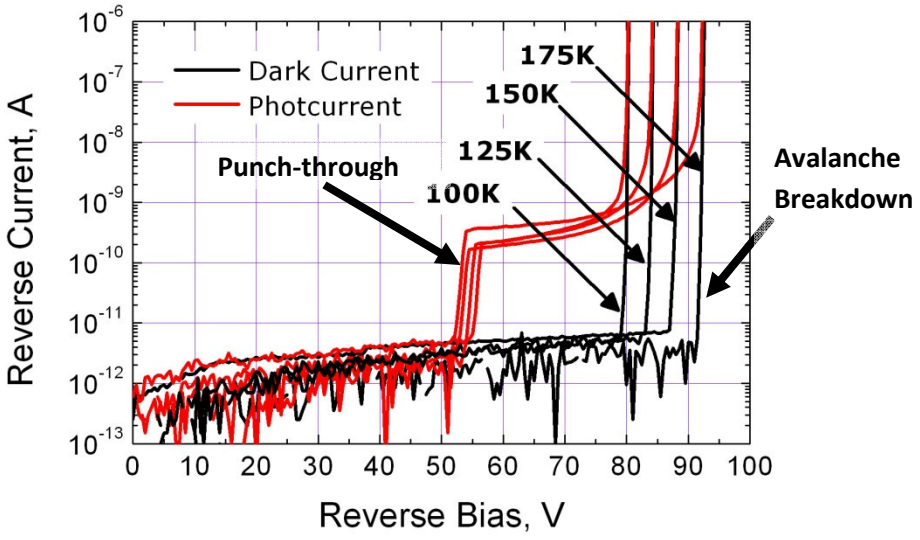

Figure 3.9. Reverse I-V characteristic for a 20 μm diameter SPAD-3Q device at varying temperatures.

As stated previously, the punch-through voltage (~ 55 V in Figure 3.9) does not change greatly with temperature, whereas the breakdown voltage decreases at a rate of ~ 0.17 VK^{-1} which is consistent with previously published results [6]. From the I-V measurement, it is possible to estimate device performance in terms of dark count rate. If the device has a high partially multiplied dark current it is likely that this will manifest itself in a high dark count rate. All I-V measurements were taken with an HP 4145B semiconductor parameter analyser capable of a few pA accuracy.

Once an I-V has been recorded at a certain temperature, it is then possible to start characterising the detector.

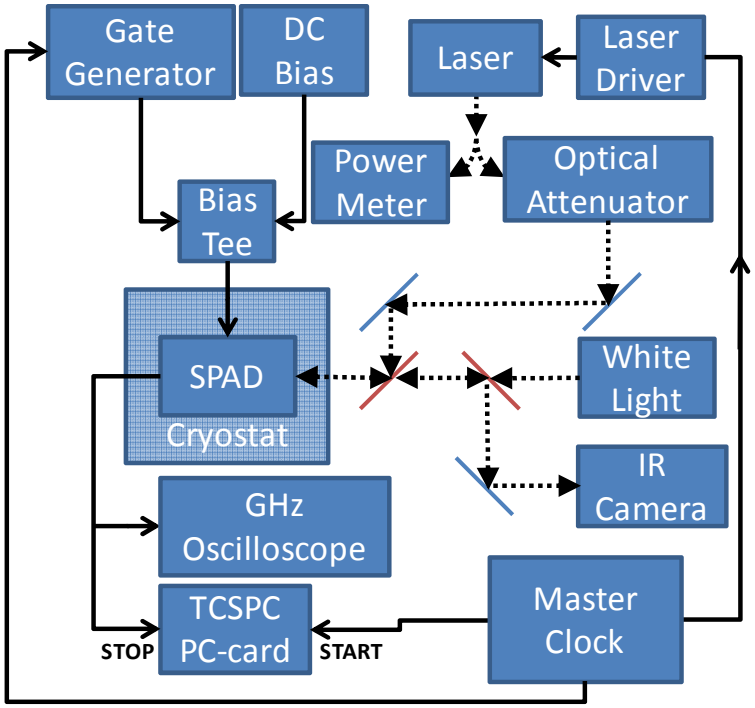

Figure 3.10. SPAD characterisation setup where the dotted lines represent optical paths/fibres, and solid lines represent electrical connections. The laser wavelength was 1550 nm. The slanted blue lines represent mirrors, and the red represent pellicle beam-splitters.

For the characterisation of these detectors in terms of photon-counting performance, we used the setup shown in Figure 3.10. Two lasers, $\lambda \sim 1550$ nm, were used for the characterisation: a passively Q-switched diode laser for the timing measurements with a low jitter 20 ps pulse-width and a distributed feedback (DFB) laser for alignment and SPDE measurements. This setup allowed SPDE and jitter measurements to be performed without altering the optical alignment of the system [11]. One output of the beamsplitter was used to constantly monitor the laser power, the second was heavily attenuated to ensure an average of less than one photon per pulse arrived at the SPAD detector. The output fibre of the optical attenuator was collimated and then focused on the sample using a $\times 20$ magnification microscope objective lens. All optical components for imaging and delivering the laser to the detector were fixed to an optical bench, allowing high-precision alignment and focusing on the detector. White light and an infrared camera were used to image the devices to ensure that the incident light was fully coincident with the detector window. The sample was fixed in a continuous flow cryostat under high vacuum, and was connected to two coaxial cables for biasing and output pulse readout. The DC bias had a gate superimposed upon it by the pulse generator to take the device beyond avalanche breakdown and into the Geiger regime,

i.e., the gated mode operation [12]. This pulse generator also provided the synchronisation pulse for the laser drivers and signals the start for the timing of the photon-counting card. At low excess biases the avalanche pulse current was small and therefore amplified before passing through a constant fraction discriminator. The photon-counting statistics were measured using an Edinburgh Instruments Ltd. TCC900 photon-counting PC card, apart from the jitter measurements (detailed later) for which a Becker & Hickl SPC600 photon-counting card was used since its internal jitter contribution was lower.

The SPADs were characterised according to the appropriate figures of merit for single-photon detectors: Dark count rate (DCR), single-photon detection efficiency (SPDE), noise equivalent power (NEP) and timing jitter. Afterpulsing analysis will be discussed in Chapter 4.

The DCR is the count rate of the detector when no light is incident on it, and is due to thermally generated carriers but is enhanced by the release of trapped carriers. In gated mode of operation, the DCR is calculated by the following equation:

$$DCR = \frac{\text{total number of measured dark events}}{t_{aqc}\, t_g\, f} \qquad \text{Equation 3.1}$$

where t_{acq} is the total acquisition time for the measurement, t_g is the gate duration and f is the frequency of operation or repetition rate of the gate pulse.

The SPDE is the probability that a photon incident on the detector generates an output pulse. It can be measured as the ratio of the number of detected photon events compared to the number of incident photons averaged over a large number of optical pulses, and assuming a low probability of multiple photons in each optical pulse. In gated mode, the SPDE is given by Equation 3.2 below:

$$SPDE = \frac{(\text{total measured counts}) - (\text{dark events})}{(\text{number of incident photons})} \frac{1}{t_{aqc}\, f} \qquad \text{Equation 3.2}$$

where t_{acq} is the total acquisition time for the measurement and f is the frequency of operation or repetition rate of the gate pulse.

The NEP is a figure of merit for photodetectors that takes into account both the SPDE and the DCR. It represents the least measurable optical power (with 1-Hz bandpass

noise filtering, that is, 1-s total counting time in single-photon counting) and is given by the following equation:

$$NEP = \frac{h\upsilon}{SPDE}\sqrt{2DCR} \qquad \text{Equation 3.3}$$

where $h\upsilon$ is the energy of a single-photon.

Gated mode operation was used for all of the following results which consisted of applying a constant DC bias to the detector at 1 V below breakdown (V_{BD}) and applying a 100 ns duration gate at an amplitude corresponding to a relative excess bias (V_{XS}) of 10% of V_{BD} calculated as follows:

$$V_{xs}(\%) = \frac{(V_{DC} + V_{gate}) - V_{BD}}{V_{BD}} \qquad \text{Equation 3.4}$$

Prior to the growth and fabrication programme with the University of Sheffield, members of the photon counting group at Heriot-Watt University investigated the use of commercially available linear multiplication APDs in Geiger mode. After an intensive selection process studying batches of APDs from different manufacturers, the best device was found to be Epitaxx EPM239AA [7]. Hence, we compare the devices fabricated in this growth programme with this device found to have the best Geiger-mode performance after rigorous selection, although it should be noted that most commercially available linear multiplication devices have much increased dark count rates when operated under the same Geiger-mode conditions [5]. Note that SPAD 1Q and 3Q do not have anti-reflective coatings on the optical windows unlike the Epitaxx device, thus reducing the expected SPDE by approximately a third. The Epitaxx EPM239AA has a nominal active area diameter of 40 μm and some information regarding its microstructure has been published previously [13] [14]. This published material indicates that the p-well is obtained by two different zinc diffusion processes. The edge breakdown is prevented by use of two floating guard rings at each side of the well. The grading of the quaternary layer is obtained by growing three different sublayers of varying composition of InGaAsP. Substrate entry geometry allows incident photons a second chance at absorption after reflection at the annealed AuZn top contact, thus permitting a thinner InGaAs absorption layer thickness and a corresponding reduction in the thermally generated leakage current for a given device diameter.

All the work on the Epitaxx devices was previously performed by Dr Phil Hiskett and Dr Sara Pellegrini at Heriot-Watt University. The tests on SPAD 1Q & 3Q devices were performed by the Author and Dr Sara Pellegrini.

Firstly, SPDE will be reported. Figure 3.11 shows the comparison between Epitaxx and our custom design SPAD devices. It should be pointed out that Epitaxx have ceased manufacture of the APD reported herein and, since then, some of the key researchers and product designers from Epitaxx have moved to Princeton Lightwave Inc. Devices from Princeton Lightwave Inc. will be discussed later.

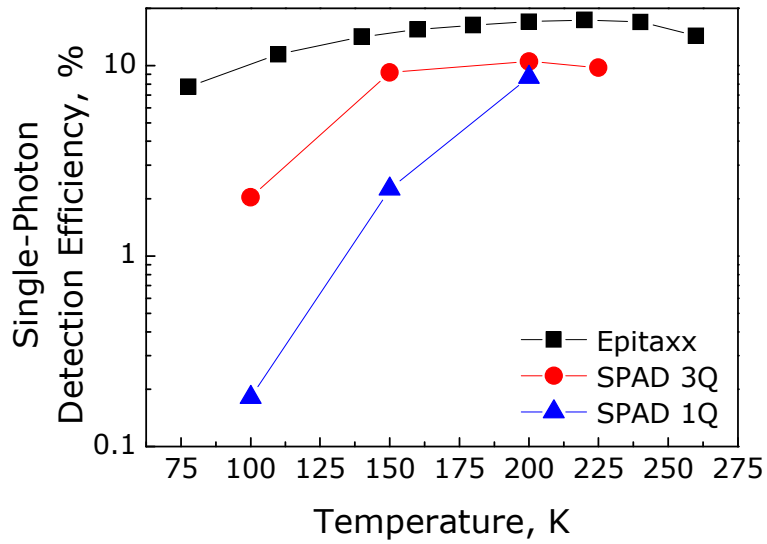

Figure 3.11. SPDE of SPAD 1Q and 3Q compared to the Epitaxx EPM239AA.

Figure 3.11 shows the SPDE of SPADs 1Q & 3Q compared to the Epitaxx device. At high temperatures, the SPADs reach a SPDE of about 10%, which is comparable to the best reported performance of InGaAs/InP single-photon detectors operating in comparable conditions. Higher SPDE was reported only for operation with ultrashort gate duration (about 1 ns) and larger excess bias [15]. When the temperature is reduced, the detection efficiency drops significantly in both the SPAD-1Q and SPAD-3Q detectors, but significantly more so for the SPAD-1Q detectors. This shows the effect of the different number of quaternary steps on the SPDE. At low temperatures where the carriers do not have much thermal energy, the barrier inhibits the passage of the hole into the multiplication region hence lowering the SPDE particularly at low temperatures. This is reflected in the difference between the SPDE of the 1Q and 3Q devices. As the temperature is increased, their performances converge since the photo-generated hole has more thermal energy to traverse the valence band discontinuities.

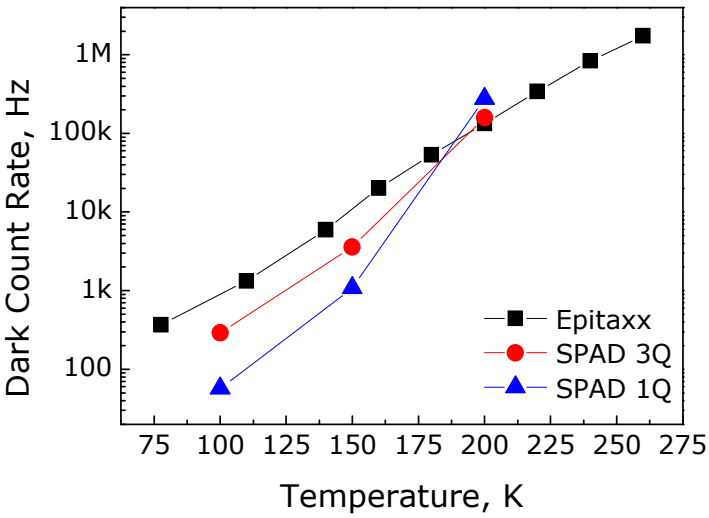

Figure 3.12. DCR of SPAD-1Q and 3Q compared to the Epitaxx EPM239AA.

Figure 3.12 represents the DCR of the devices tested. Generally, the SPAD devices presented here compare well in terms of DCR with the selected APD device. The expected behaviour of the DCR as a function of temperature is an exponential dependence. At temperatures higher than 200 K the SPADs have a higher DCR than the Epitaxx APD, but this drops at lower temperature, and is more noticeable for the SPAD-1Q. This is most likely due to thermally generated holes in the InGaAs not being efficiently swept across the valence band discontinuity at low temperature due to their reduced thermal energy. This effect is more pronounced in the SPAD-1Q due to the higher valence band discontinuity between adjacent sub-layers in comparison to the SPAD-3Q device.

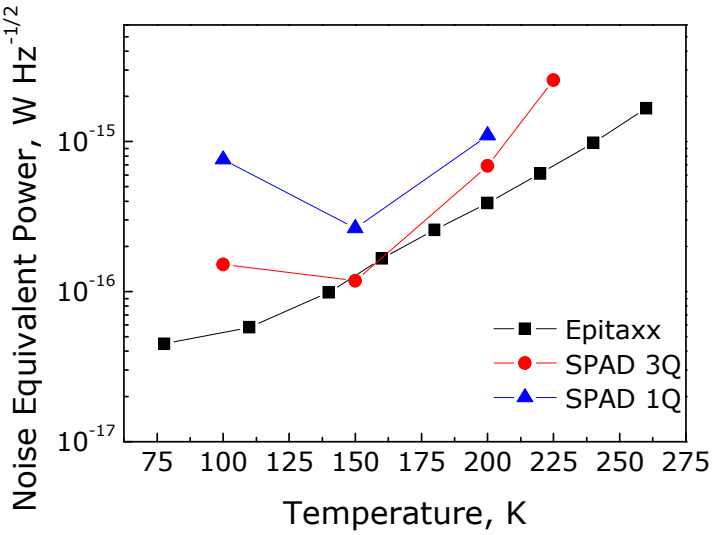

Figure 3.13. NEP of SPAD-1Q and 3Q compared to the Epitaxx EPM239AA.

Figure 3.13 shows the results in terms of NEP. The lower the NEP, the more sensitive the device, therefore at high temperature the SPADs still compare well with the commercial devices, but their performance degrades at lower temperature due to the large reduction in SPDE.

Finally, jitter measurements were conducted on the SPAD-3Q devices. Figure 3.14 represents the best jitter measurements on three different active area devices from the same chip. The jitter measurements were performed with a fast (< 50 ps) duration laser pulsed at the low repetition frequency of 10 kHz to avoid the effects of afterpulsing and at a mean photon number of ~ 0.1 photons per pulse permitting a maximum count rate of no more than 10 % of the clock frequency. This is necessary to avoid the effects of pulse pile-up which could compromise the accuracy of the measurements. Jitter measurements were not conducted on SPAD 1Q due to reliability issues with the devices, mainly due to thermal cycling.

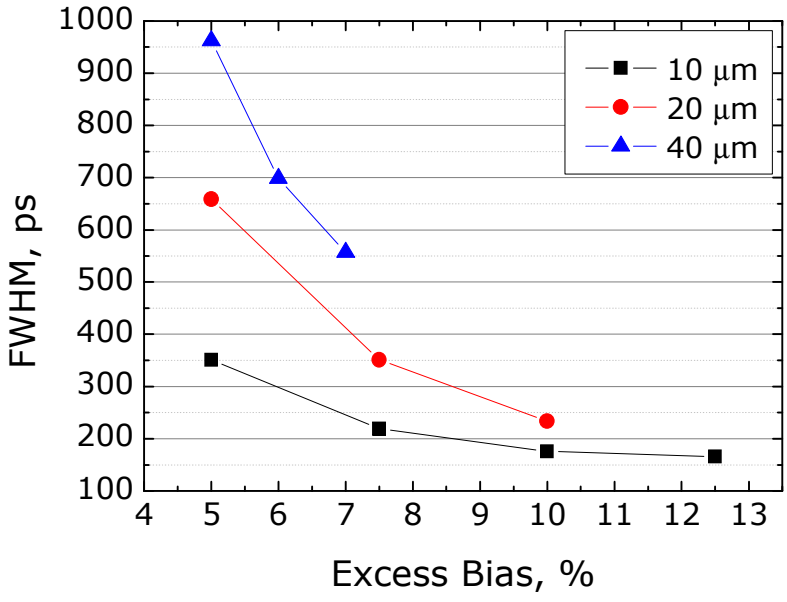

Figure 3.14. Jitter (FWHM) shown as a function of excess bias for different device areas for SPAD-3Q at 175 K.

From the results in Figure 3.14 the link between device diameter and jitter is clear. This has been observed previously in Si SPADs [16] and is linked to two factors. The first is a minor contribution caused by the random time taken for the first generated electron-hole pair to reach the high field region, depending where the photon was absorbed. As the electric field increases, the carriers reach the high-field region quicker hence reducing the jitter seen at higher excess bias. Secondly, and most importantly, once an

avalanche is triggered, the high concentration of free carriers lowers the junction electric field in the area surrounding where the avalanche was triggered and the impact ionisation rate decreases. This causes the saturation of the current density and no further increase in the avalanche current will be seen until the avalanche spreads to the areas of the device that are still in the quiescent state. The time take for this to occur is dependent on carrier diffusion and drift and is demonstrated schematically in Figure 3.15. This condition directly affects the rise-time of the current pulse, and hence the overall jitter. These two factors explain the increasing timing-jitter with increasing active device area.

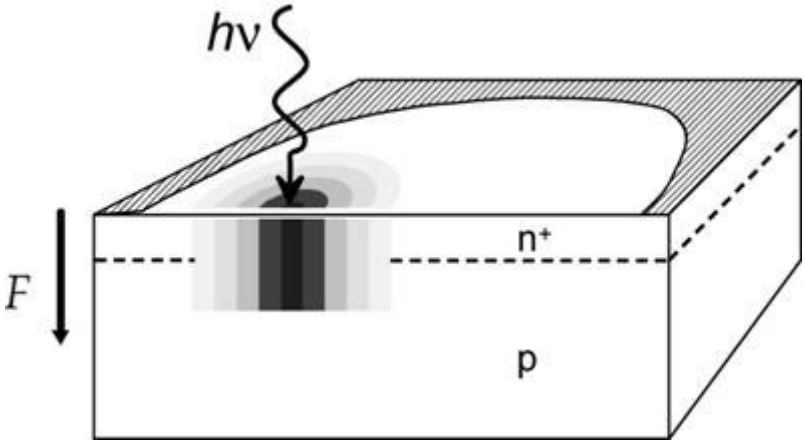

Figure 3.15. Lateral propagation of avalanche across device area [16].

In summary, custom built InGaAs/InP SPADs have been designed, modelled, grown, tested and characterised. The devices perform as well as the best linear multiplication mode APDs operated in Geiger mode with an SPDE of ~10 % and timing jitter as low as 175 ps.

In parallel with our work, Princeton Lightwave Inc. instigated their own research initiative into growing and characterising InGaAs/InP SPADs for sale in the commercial market. The following section details their device performance.

3.4 Princeton Lightwave Inc. Device Characterisation

Over the past few years, Princeton Lightwave Inc. has been designing, testing, and is now commercially selling InGaAs/InP SPADs specifically designed for Geiger-mode operation, under the guidance of various staff previously at Epitaxx including Mark Itzler. The photon counting group at Heriot-Watt University was requested, by him, to characterise two of their test devices in order to compare and contrast findings

with their own. The structure of the device is shown in Figure 3.16 and is similar to the devices characterised previously, except the Princeton Lightwave design uses a fully metalised p-contact to act as a mirror for unabsorbed photons, and substrate entry. For this, an identical setup was used as for characterising our devices. The findings of which will now be presented below.

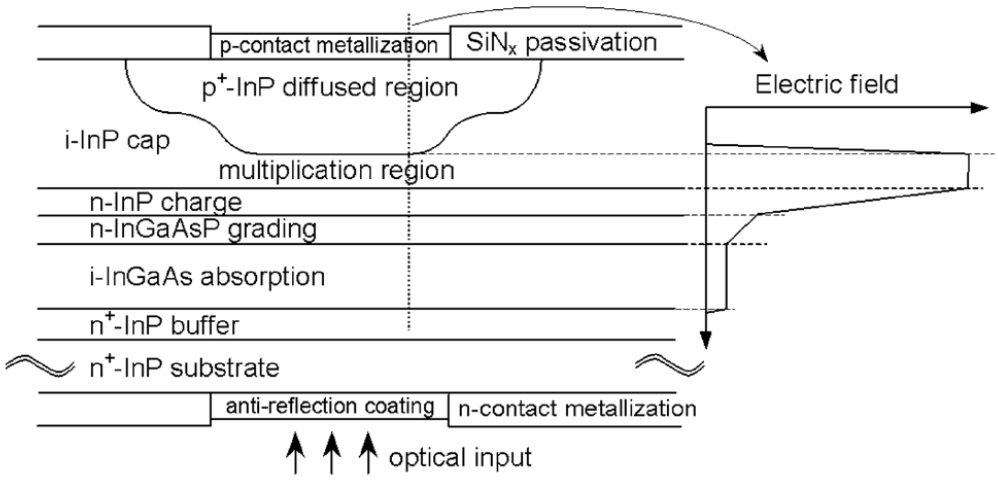

Figure 3.16. Schematic cross-section of a Princeton Lightwave InGaAs/InP SPAD showing optical entry through the substrate [17].

The InGaAs/InP avalanche photodiode detectors PLI-75-60 and PLI-75-102 with a 25 µm diameter were characterised. These devices correspond to a central and edge position on the growth wafer for devices PLI-75-102 and PLI-75-60 respectively. For easy reference we will call the edge device E25, and the centre one C25. The characterisation of the devices was in terms of the previously explained and presented figures of merit. The measurements were taken at five different temperatures of 150 K, 175 K, 200 K, 225 K and 250 K. At each temperature the results show the device characteristics at different excess bias conditions. The devices were biased in gated mode, using a DC bias of V_{DC} = 3 V below breakdown, and a gate bias with amplitude V_{gate} and duration of 100 ns. The percentage excess bias was calculated as previously.

The device E25 exhibited a breakdown voltage 1.5 V lower than C25. This is in agreement with published results on the behaviour of the devices in respect to their position on the wafer. Figure 3.17 shows the value for the breakdown voltage at different temperatures for both detectors.

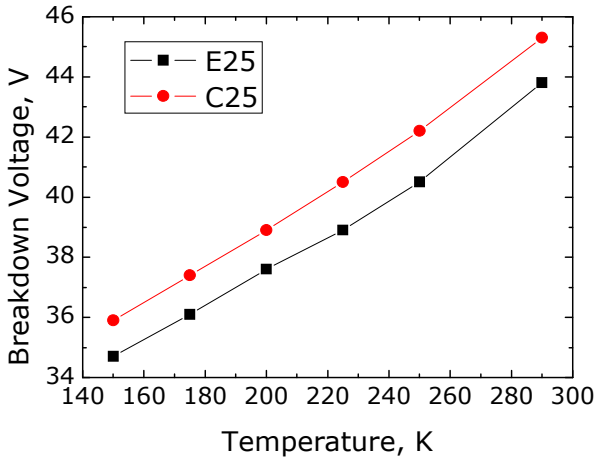

Figure 3.17. Temperature dependence of the breakdown voltage for both devices. The value for the edge device E25 is lower than that measured for the device coming from the centre of the wafer C25.

All measurements were performed at a low gate repetition rate of 10 kHz to avoid the effects of afterpulsing.

In Figure 3.18 we see the DCR at the 5 different temperatures measured at varying excess biases.

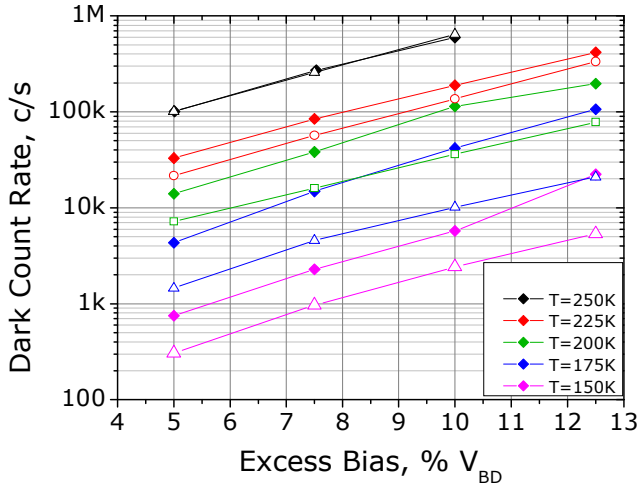

Figure 3.18. Dark count rate versus relative excess bias for the device E25 (filled symbols) and C25 (empty symbols) at different temperatures. At 150 K the device E25 shows a strong increase in the dark count rate with increasing bias due to trapping.

The behaviour in terms of dark count rates is as expected, exhibiting an exponential dependence of dark count rate with temperature, as well as an exponential dependence of dark count rate on excess bias. In general, at each measured operational temperature, the value of the DCR for E25 is higher than that measured for C25.

Plotting the DCR against 1/kT in an Arrhenius plot allows the extraction of the activation energy of the dark count mechanism. This is displayed for both devices in Figure 3.19.

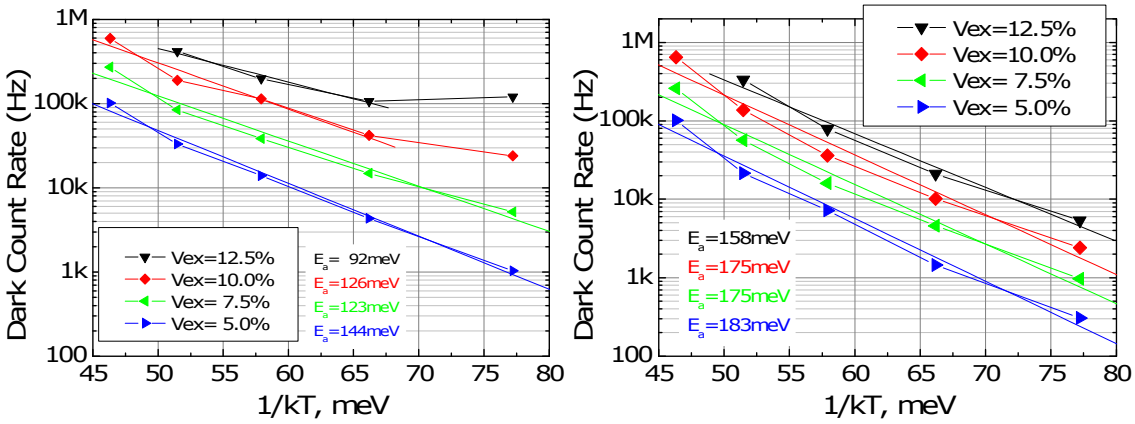

Figure 3.19. Arrhenius plot of the dark count rate for device E25 (left) and C25 (right).

As is evident from Figure 3.19, the activation energy is the same at all excess biases, but is different for the two devices. Device E25 shows an activation energy of 124 meV, while the value of the activation energy for diode C25 is 175 meV.

SPDE in terms of excess bias is presented in Figure 3.20.

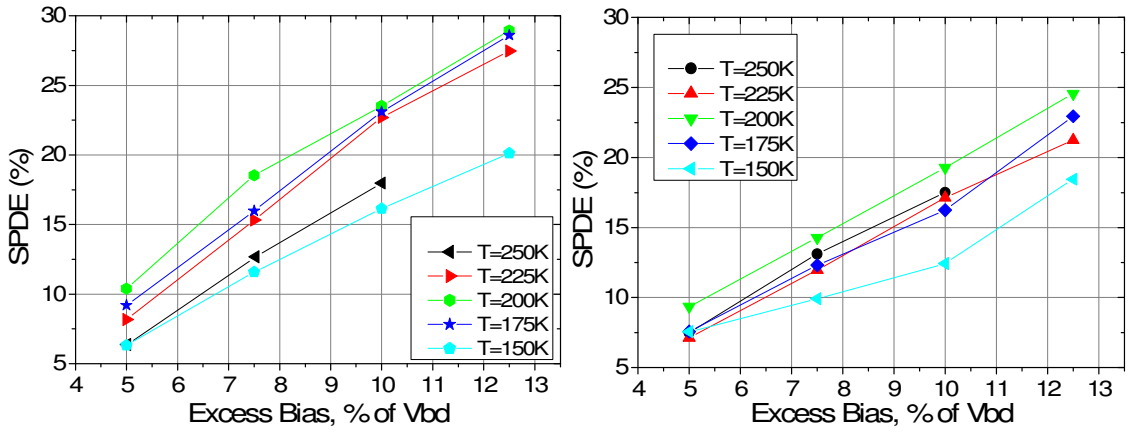

Figure 3.20. Single-photon detection efficiency vs relative excess bias for the device E25 (left) and C25 (right).

The behaviour of the SPDE is linear with excess bias, as expected. In terms of temperature dependence, there is a maximum in the detection efficiency at a temperature of 200 K for both detectors. In general, the edge detector E25 exhibits higher detection efficiency than the central detector C25.

Figure 3.21 show the behaviour of DCR vs. SPDE at 200 K. The edge device presents a dark count rate twice as high as the one measured for the central detector. This is consistent with the position of the devices on the wafer with respect to the flow direction during growth. In reference [17], the authors state that there is an increase in the integrated field control charge from the centre towards the edge going upwards from the flat edge of the wafer. This reflects in a reduction of the electric field and consequently a decrease in DCR as we move from the flat edge towards the centre of the wafer and further away, which is consistent with the behaviour measured for the devices under test. This is also confirmed by the higher detection efficiency measured for the device E25.

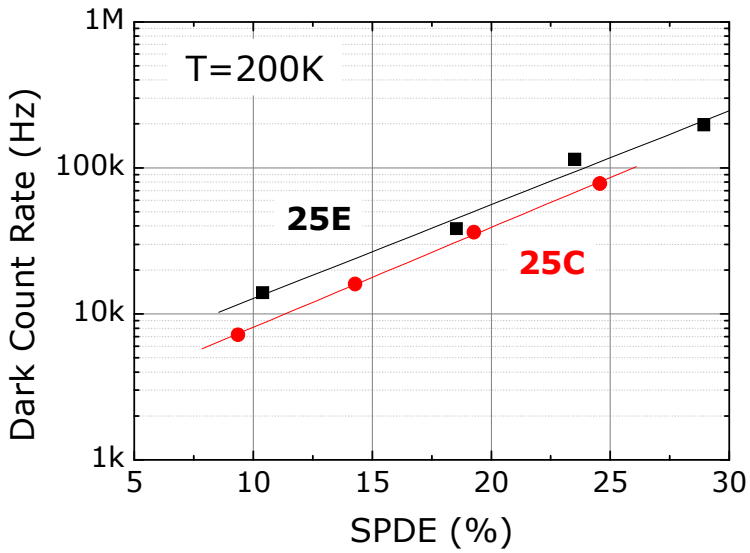

Figure 3.21. Dark count rate versus single-photon detection efficiency at 200 K for both devices.

The NEP is displayed in Figure 3.22.

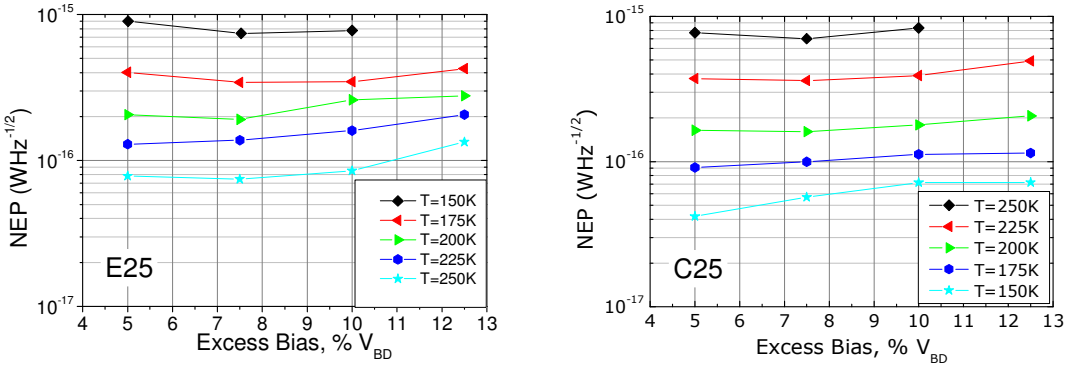

Figure 3.22. Noise equivalent power vs excess bias at different temperatures for detectors E25 (left) and C25 (right).

Generally speaking, the central device, C25 has a lower NEP and is therefore a more sensitive device.

The timing jitter was measured at the different temperatures at a repetition rate of 10 kHz, since the afterpulsing effect will not affect this parameter

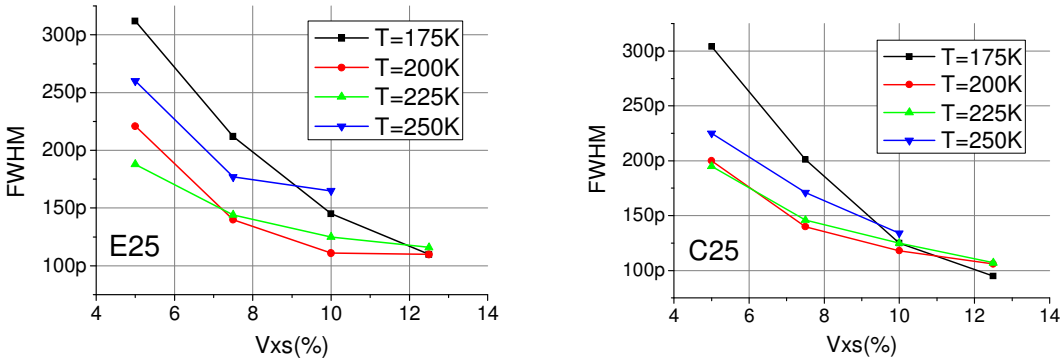

Figure 3.23. Timing jitter versus excess bias at different temperatures for device E25 (left) and C25 (right).

As shown in Figure 3.23, the two devices have very similar timing jitter, within experimental error. The timing jitter of the detectors decreases with increasing excess bias as expected. At high temperatures the jitter is independent on the temperature of the detector, but at 175 K the long tail becomes dominant on the timing jitter at low excess biases, as shown in Figure 3.24. This is due to the lower electric field at lower excess biases and therefore a less efficient collection.

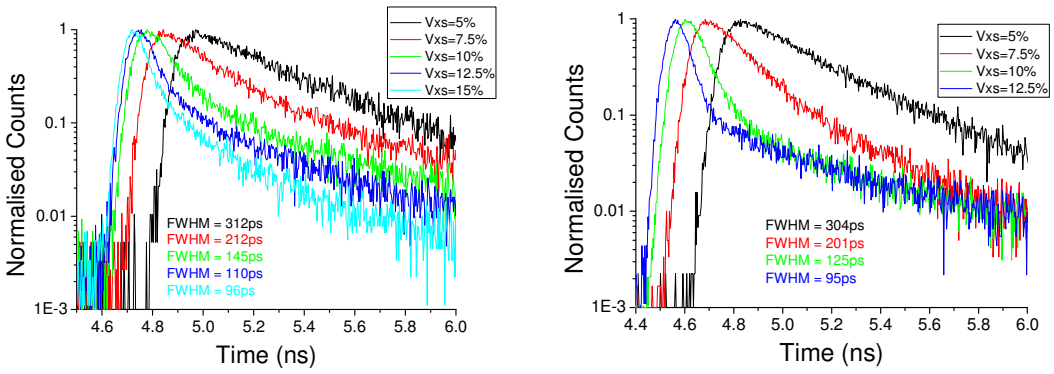

Figure 3.24. MCA traces acquired for the measurement of the timing jitter at 175 K for device E25 (left) and C25 (right). The increasing effect of the tail on the jitter as the excess bias increases is evident.

When characterising the devices E25 and C25 we found some agreement and also some discrepancies with previously published results. Here, some conclusions have been drawn on devices behaviour with reference to the behaviour described in [17].

The edge device E25 presented a lower breakdown voltage than the central device, which is consistent with the published behaviour.

Device E25 also presented a higher dark count rate at lower temperatures than C25, which seems to be related to a higher electric field in the device at the heterointerface or in the InGaAs. This is also consistent with E25 presenting a higher detection efficiency than C25. The data do not agree with those presented in [17]. We believe that this could be due to the fact that the edge device that was characterised at Heriot-Watt was closer to the flat edge of the wafer, while the other devices described in the paper were taken from the opposite side with respect to the centre. The devices could present a different behaviour due to the non-uniformity of the wafer in the direction of the flow of the gasses only if the wafers did not sit on a rotating susceptor. The lower breakdown voltage, instead, could be related to the processing at the edge of the wafer. It could be useful to analyse the value of the punch-through voltage, and how it changes across the wafer. These are speculations, and it could well be that we are dealing with local changes in the wafer characteristics that produce a change of a factor of 2 in the dark count rate. This is a level of fluctuation commonly found in SPADs both made with Si and InGaAs.

3.5 Conclusions

InGaAs/InP avalanche photodiodes specifically designed for Geiger-mode operation have been modelled, fabricated and characterised. The design was based upon the SAGM structure of linear multiplication InGaAs/InP APDs, with critical modifications to allow high-field and low-temperature operation. The modelling process revealed key characteristics such as the punch-through and breakdown voltage along with facilitating the calculation of the most suitable junction geometry so as to avoid edge-breakdown.

The effects of the quaternary layer (InGaAsP) which helps smooth the valence band discontinuity were investigated through the analysis of two separate structures – SPAD 1Q and SPAD 3Q. It was found that a higher number of quaternary "steps" resulted in a significant increase in SPDE, particularly at lower temperatures (< 150 K) where the primary photo-generated hole has less thermal energy to traverse the valence band discontinuity. At higher temperatures (~ 200 K), their SPDE performance converges. The performance of SPAD 3Q was comparable to the best commercial device previously characterised (Epitaxx EPM239AA), reaching a maximum SPDE of about 10%. The Epitaxx device showed a slightly higher SPDE but also a higher DCR, resulting in a NEP approximately equal to that of SPAD 3Q. The Epitaxx had the advantage of an anti-reflective coating which increases the SPDE by a factor of approximately 30 %.

Photon-arrival timing jitter was measured for differing device active areas of SPAD 3Q type structures. As the active diameter doubled, the jitter also approximately doubled. This is linked to the lateral spread of the avalanche across the active area and the time taken for the first photo-generated carrier to reach the high field region and trigger the avalanche. Sub-200 ps jitter was measured from a 10 μm diameter SPAD at 10 % excess bias.

In collaboration with Princeton Lightwave, two SPADs were characterised from their growth programme. The SPADs were from different parts of a specific wafer (edge and central positions) resulting in slightly different characteristics. Generally speaking, the central device had a lower NEP and was therefore a more sensitive device. The jitter of both devices was the same, with the fastest being ~ 95 ps. The highest detection efficiency reached was ~ 30 %.

Comparing the Princeton Lightwave and Sheffield grown SPADs, it is clear the Princeton Lightwave devices achieve higher performance in all parameters investigated. There are a variety of reasons that may explain the difference in performance. Firstly, the Princeton Lightwave SPADs are anti-reflection coated. In addition, the SPADs are substrate entry devices and the top 'p' contact is completely metallised as in Figure 3.16. Therefore, if a photon passes through the InGaAs absorption region and is not absorbed it may be reflected by the p-type metallisation and has a second chance at being absorbed. The processing steps involved in making such a device are more complex due to the alignment of an aperture that must be place in the header-chip exactly coincident with the active area.

Finally, the way in which the devices are grown will also affect the device characteristics. From the performance reported from both sets of devices, it is clear that the material grown for the Princeton Lightwave Inc. devices is of higher quality. It is less easy to comment on the quality of the interfaces within the hetrostructure, but this may also help increase the SPDE of the Princeton Lightwave Inc. SPADs compared to those grown at the University of Sheffield.

These factors combined may explain the difference in device performance. As for how the devices compare in-terms of afterpulsing, this will be discussed in the following Chapter.

3.6 Acknowledgements

I would like to thank Dr. Sara Pellegrini for her help and guidance on the operation of SPADs and for training me to work effectively in the laboratory. I would also like to express my thanks to Dr. Mark Itzler for supply of samples and discussions.

3.7 References

[1] J.C. Campbell, A.G. Dentai, W.S. Holden, B.L. Kasper, *High performance avalanche photodiode with separate absorption grading and multiplication regions*, Electronics Letters, **19** (20), 818 - 820 (1984)

[2] Y. Liu, S.R. Forrest, M.J. Lange, G.H. Olsen, and D.E. Ackley, *A planar InP/InGaAs avalanche photodiode with floating guard ring and double diffused junction, Journal of Lightwave Technology*, **10** (2), 182 - 193, (1992)

[3] G.S. Buller, R.E. Warburton, S. Pellegrini, J.P.R. David, J.S. Ng, L.J.J. Tan, A. Krysa and S. Cova, *Single-Photon avalanche diode detectors for quantum key distribution*, IET Optoelectronics, **1** (6), 249 - 254 (2007)

[4] S.R. Forrest, M. DiDomenico Jr., R.G. Smith, and H.J. Stocker, *Evidence for tunneling in reverse-biased III-V photodetector diodes*, Applied Physics Letters, **36** (7), 580 - 582, (1980)

[5] P.A. Hiskett, G.S. Buller, A.Y. Loudon, J.M. Smith, I. Gontijo, A.C. Walker, P.D. Townsend, and M.J. Robertson, *Performance and design of InGaAs–InP photodiodes for single-photon counting at 1.55 μm*, Applied Optics, **39** (36), 6818 - 6829, (2000).

[6] A. Lacaita, F. Zappa, S. Cova, and P. Lovati, *Single-photon detection beyond 1 μm: Performance of commercially available InGaAs/InP detectors*, Applied Optics, **35** (16), 2986 - 2996 (1996)

[7] P.A. Hiskett, J.M. Smith, G.S. Buller, and P.D. Townsend, *Low-noise single-photon detection at awavelength of 1.55 μm*, Electronics Letters, **37** (17), 1081 - 1083 (2001)

[8] S.M. Sze, and G. Gibbons, *Effect of junction curvature on breakdown voltage in semiconductors,* Solid-State Electronics, **9** (9), 831 - 845 (1966)

[9] M. Kobayashi, S. Yamazaki, and T. Kaneda, *Planar InP/GaInAsP/GaInAs buried structure avalanche photodiode*, Applied Physics Letters, **45**, (7), 759 - 761 (1984)

[10] S. Pellegrini, *InGaAs/InP Single-photon avalanche diodes*, Thesis submitted for the degree of doctor of philosophy, (2005)

[11] S. Pellegrini, R.E. Warburton, L.J.J. Tan, J.S. Ng, A.B. Krysa, K. Groom, J.P.R. David, S. Cova, M.J. Robertson, and G.S. Buller, *Design and Performance of an InGaAs–InP Single-Photon Avalanche Diode Detector*, IEEE Journal of Quantum Electronics, **42** (4), 397 - 403 (2006)

[12] S. Cova, M. Ghioni, A. Lacaita, C. Samori, and F. Zappa, *Avalanche photodiodes and quenching circuits for single-photon detection*, Applied Optics, **35** (12), 1956 - 1976, (1996)

[13] M.A. Itzler, K.K. Loi, S. McCoy, N. Codd, and N. Komaba, *Manufacturable planar bulk-InP avalanche photodiodes for 10 Gb/s applications*, in Proceedings of 12th Annual Meeting: Lasers Electro-Optics Soc., Paper ThK0005, 748 - 749 (1999)

[14] M.A. Itzler, K.K. Loi, S. McCoy, N. Codd, and N. Komaba, *Highperformance, manufacturable avalanche photodiodes for 10 GB/s optical receivers*, in Proceedings Optical Fiber Communications Conference, Washington, DC, 126 - 128 (2000)

[15] D. Stucki, G. Ribordy, A. Stefanov, H. Zbinden, J.G. Rarity, and T. Wall, *Photon counting for quantum key distribution with Peltier cooled InGaAs–InP APDs*, Journal of Modern Optics, **48** (13), 1967 - 1981 (2001)

[16] A. Spinelli and A.L. Lacaita, *Physics and numerical simulation of single-photon avalanche diodes*, IEEE Transactions on Electronic Devices, **44** (11), 1931 - 1943 (1997)

[17] M.A. Itzler, R. Ben-Michael, C-F. Hsu, K. Slomkowski, A. Tosi, S. Cova, F. Zappa, and R. Ispasoiu, *Single-photon avalanche diodes (SPADs) for 1.5 μm photon counting applications*, Journal of Modern Optics, **54** (2 - 3), 283 - 304 (2007)

Chapter 4 - Afterpulsing in InGaAs/InP Single-Photon Avalanche Diodes

4.1 Introduction

In Chapter 3, the key figures of merit were reported for the InGaAs/InP SPADs grown in a programme in conjunction with the University of Sheffield and also those gained from the two Princeton Lightwave Inc. test devices. The standard of these figures of merit result in a device that satisfies many of the requirements for use in single-photon counting experiments, and such devices have been used in applications such as QKD [1]. However, these devices have been severely limited in terms of the count rate at which they can be operated, along with other limitations on operating conditions placed on the detectors, due to the detrimental effects of afterpulsing.

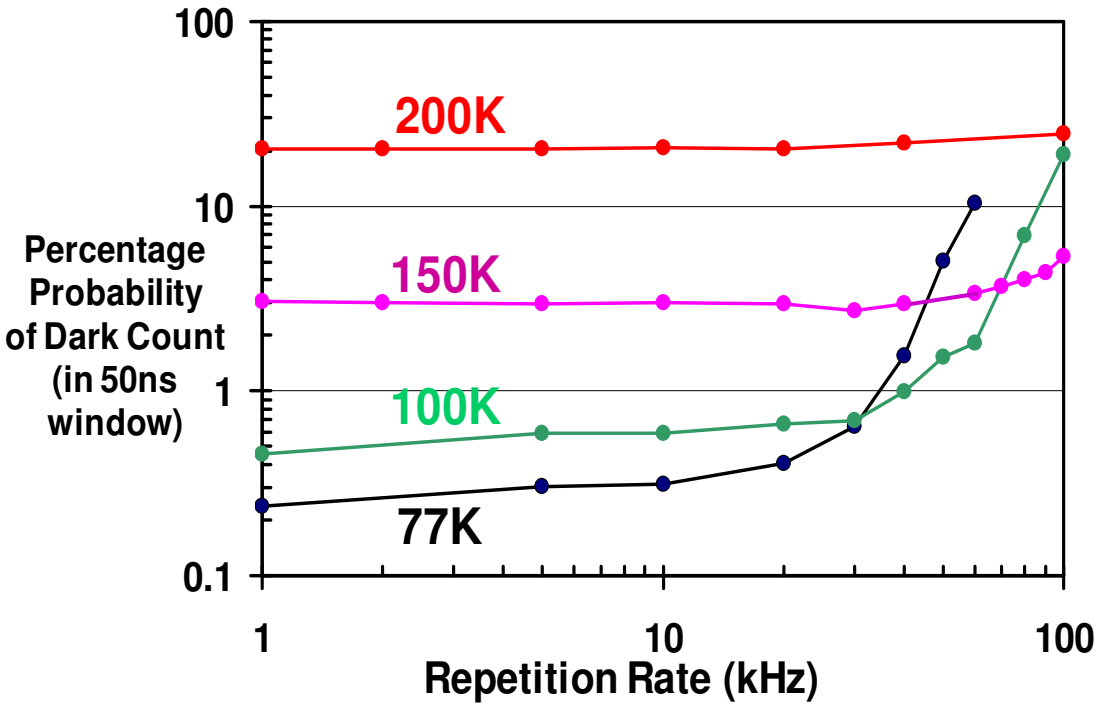

Figure 4.1. Percentage probability of dark counts in a 50 ns timing window versus repetition rate (gating frequency) [2].

The afterpulsing phenomenon is essentially a memory effect caused by the large amount of carriers that flow through the device during the avalanche process associated with any individual photon event, or, indeed, a dark count. Some of these carriers can become trapped in deep levels [3] and are released after the avalanche event, and may contribute to the dark counts in the measurement during the subsequent period if the

device is armed again before all the traps have depopulated. Since these SPADs are operated in gated mode, it is at least possible, in principle, to disable the SPAD for a sufficiently long period of time such that there is a negligible probability of a filled trap. If the device is enabled before all trap states are empty, it is possible that these carriers will be released and cause an unwanted count, or "afterpulse". Figure 4.1 illustrates the afterpulsing phenomenon: as we increase the repetition rate (the frequency at which the AC gate is superimposed on the SPAD to take the device beyond breakdown and into Geiger mode) the probability of observing a dark count within a certain window increases.

The release of trapped carriers is temperature dependent, and causes a further conflict when deciding how best to operate the device for the specific application. At low temperatures, the DCR is low but the trapped carriers have a longer lifetime, hence the afterpulsing is noticeable even at lower device repetition rate. At higher temperatures, the DCR is higher but the effects of afterpulsing are less noticeable. The effects can be seen in Figure 4.1 – the 200 K trace only just starts to show signs of afterpulsing as the repetition rate reaches several tens of kHz – a much higher repetition rate when compared to the gating frequencies where afterpulsing is evident at lower temperatures.

In photon counting applications this causes issues in terms of the maximum permissible count rate at which the detector can be operated. The afterpulsing probability is directly linked to the amount of charge carriers that pass through the device per avalanche event. Due to this, there are several methods adopted by InGaAs/InP SPAD users in order to limit the charge carriers that pass through the device. Most commonly, this is accomplished by placing a very short gate on the detector (< 5 ns) [4] [5] hence limiting the avalanche pulse current. Other methods to reduce afterpulsing will be discussed in Chapter 5 where alternatives to the standard Geiger mode operation will be presented.

Using a very short gate at the arrival time of the photon can only be efficiently adopted by some types of applications such as QKD when the detector is used in a repetitive and periodic manner. For other applications such as TRPL and LIDAR a wider window of photon arrival times is preferred, indeed, LIDAR would benefit from a "free-running" device (see Chapter 6). Therefore to fully exploit InGaAs/InP detectors, a dedicated effort needs to be placed in researching the causes of the afterpulsing effect and to attempt to lessen its deleterious effects on device performance. For this reason, part of the work undertaken by the Author was to conduct a full afterpulsing analysis on

InGaAs/InP SPADs along with other test structures to try and gain a better understanding of the phenomenon.

4.2 Afterpulsing Analysis Methods

Methods for analysing afterpulsing in SPADs can be defined by two separate measurement techniques. The first involves a simple change in hold-off time between two gates placed upon the detector within 1 clock period and measuring the DCR within both gates. An example of the data recorded using this method can be seen in Figure 4.2.

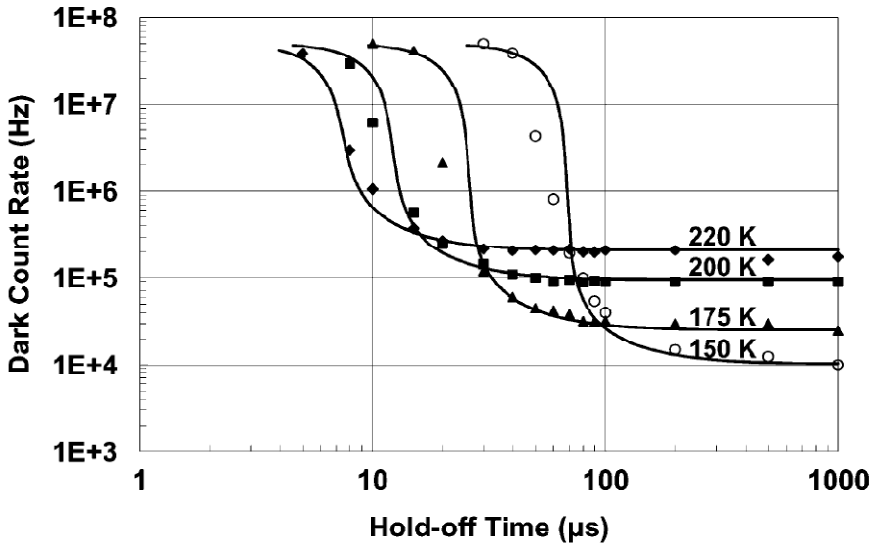

Figure 4.2. DCR of an InGaAs/InP SPAD measured as a function of hold-off time between subsequent gates. Afterpulsing data can be amassed this way using the hold-off time technique as in [6]. It should be noted that both axis are logarithmic.

In Figure 4.2 the DCR as a function of hold-off time is plotted at different temperatures. Whilst this method provides some information about the trapping within the device there are a few disadvantages when compared to the method described later. We let a certain amount of current pass through the device (avalanche current), we then disable the device and subsequently re-arm it after a certain hold-off time. One potentially important issue with using this dark count rate as a basis for afterpulsing measurements is that we cannot be sure exactly how much charge passed through the device in the first gate since the avalanche is triggered only by a dark count which has the same probability of occurring at any time during the first gate. This means that every time a

new measurement is made, it may not always be an accurate repeat of the measurement before since the first dark count will generate an avalanche current of different duration, and hence an uncertain integrated charge. If the gate is of relatively short duration then the variation in integrated charge over many events will be minimised. However, using a short gate also results in a much longer measurement acquisition time in order to build up a statistically reliable measurement of the afterpulsing probability, especially at lower temperatures due to the exponentially reduced thermal excitation of carriers causing dark counts.

In principle, for an accurate analysis of the afterpulsing phenomenon, it would be preferable to control the exact amount of charge flowing through the device to ensure that the same amount of trap states are filled during the first gate. The second gate could then be used to observe the release of these traps.

The time-correlated carrier counting method (TCCCM) [7] [8] was the method chosen by the Author in order to investigate the trapping phenomenon. A schematic for the gating sequence is shown in Figure 4.3.

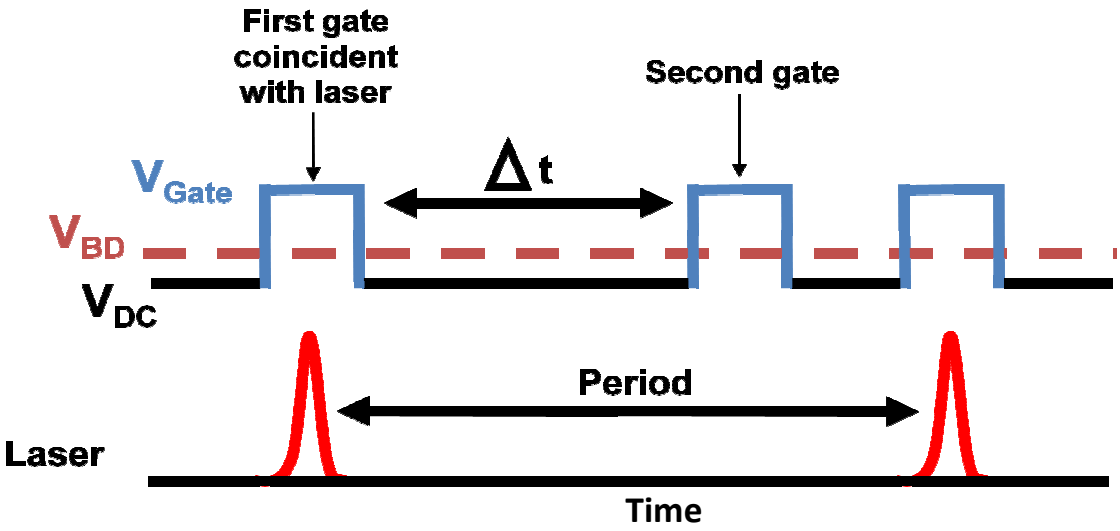

Figure 4.3. Gating scheme for the TCCCM for measuring the afterpulsing probability.

Referring to Figure 4.3, the SPAD is reverse DC-biased (V_{DC}) just below breakdown (V_{BD}) and has a gate of amplitude V_{Gate} superimposed to take the detector into Geiger mode. Exactly coincident with the start of this first gate, a multi-photon laser pulse ($\lambda \sim$ 1550 nm) is incident on the detector. This ensures that the device breaks-down at the start of every period for the entire length of the gate and the charge flowing through the device is kept constant for each individual measurement. At a time Δt later, a second

gate is placed upon the detector with the same amplitude, V_{Gate}, with no light incident upon the detector. During this second gate, only the dark counts are measured as the traps states decay and released carriers contribute to the apparent dark count rate. By varying Δt from very short delays (almost adjacent to the 1st gate) to very long delays (at the end of the period) and scanning the 2nd gate, an afterpulsing probability distribution can be measured. An example of an afterpulsing probability graph can be seen in Figure 4.4. Practically, this is accomplished using a gated Stanford photon-counter (SR400) so that the number of counts in the 1st and 2nd gates can be counted separately and simultaneously. The number of counts in the 2nd gate divided by the number of counts in the 1st gate gives the afterpulsing probability. In these experiments, each gate was chosen to be 50 ns in duration using gated quenching (the gate was applied to the SPAD for the full 50 ns duration regardless of the avalanche's temporal position within that gate.)

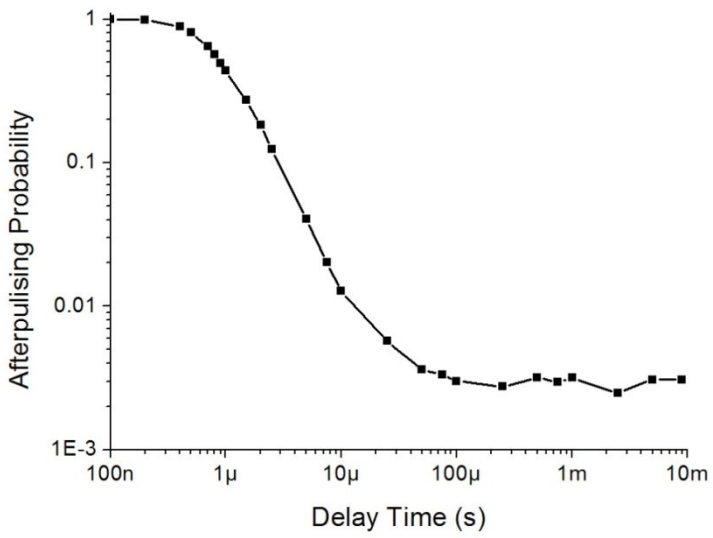

Figure 4.4. Example of an afterpulsing probability distribution measured using the TCCCM from released traps where the time along the x-axis signifies the delay between the 1st and 2nd gates.

Before measuring the afterpulsing probability using this method, the DCR was measured with no light incident on the detector, under otherwise identical experimental conditions. At long values of Δt, we expect the afterpulsing probability to reach the DCR of the device. If this true dark count rate is not achieved, then the repetition frequency of the measurement was further reduced in order to let the traps decay fully. This is a very important condition for these measurements as is demonstrated in Figure

4.5 (a) and (b). If too short a period is used, the trap population never fully decays and subsequent avalanches increase the trap population as shown in Figure 4.5 (a).

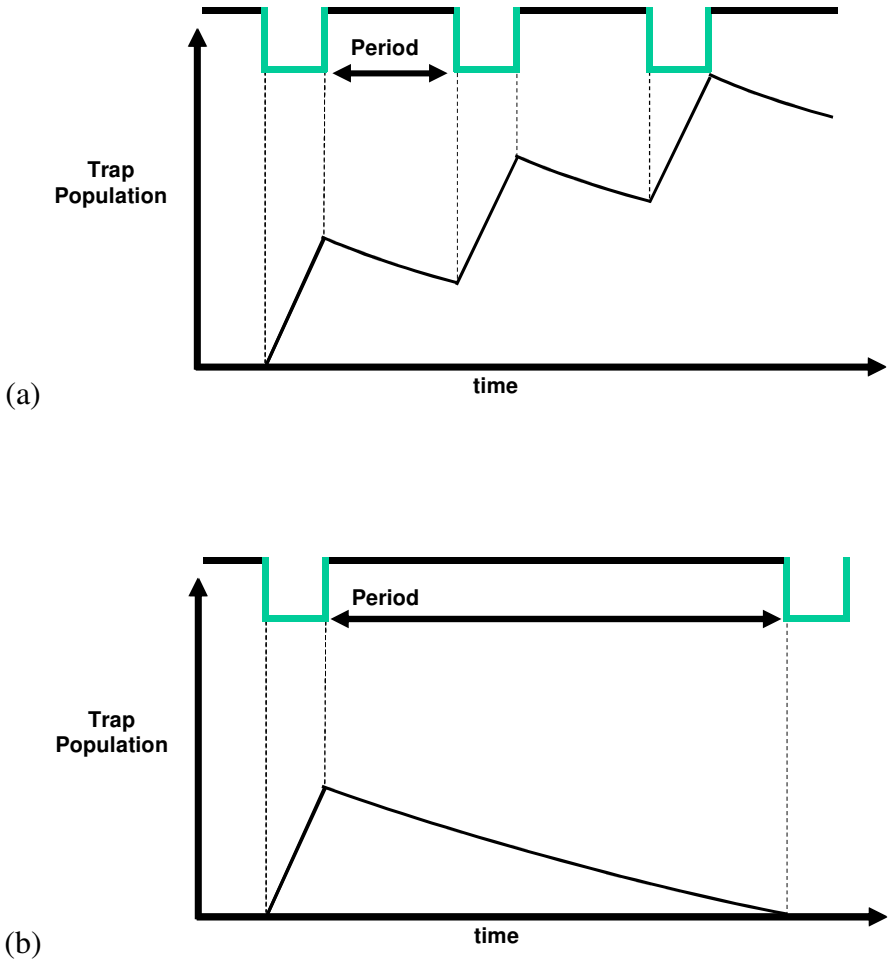

Figure 4.5. (a) TCCCM method used with gated mode operation, where the period of operation is too short and does not allow all trap states to decay fully, resulting in an inaccurate measurement. (b) As previous, except with a sufficiently long period to allow all carriers to decay from traps before re-arming the device in the following period, after [9].

After ensuring that the period was long enough for all trap states to decay completely (which required up to 1 second for our devices at low temperatures, < 150 K), the TCCCM could then be used to observe the release of trapped carriers. Each delay point was recorded individually for a period of time that allowed good statistical accuracy of the count rate in the second gate since, at times, this was many orders of magnitude lower than that in the first. The TCCCM was employed at several different temperatures so that an Arrhenius plot could be compiled in order to extract information about the trap energy.

4.3 Afterpulsing Analysis Results

The afterpulsing probability as a function of delay time between gates for a 20 μm active area diameter SPAD-3Q device can be seen in Figure 4.6. The TCCCM was used at 4 different temperatures. The gate length was 50 ns, and the excess bias was set so that the total charge flowing through the device was the same at each temperature. The output pulse as seen on an oscilloscope (50 Ω) is shown in Figure 4.7. Observing Figure 4.6 it can be seen that at 190 K, for example, there is still a finite probability of finding a trapped carrier up to and beyond 1 ms. In practical terms this would mean a 1 ms detector dead-time before subsequent re-arming, limiting the repetition rate to ~ kHz to fully avoid the effects of afterpulsing. In terms of the actual afterpulsing measurement, it was necessary to reduce the repetition rate to 1 Hz at low temperatures to ensure that all the trap states were vacant before the following period.

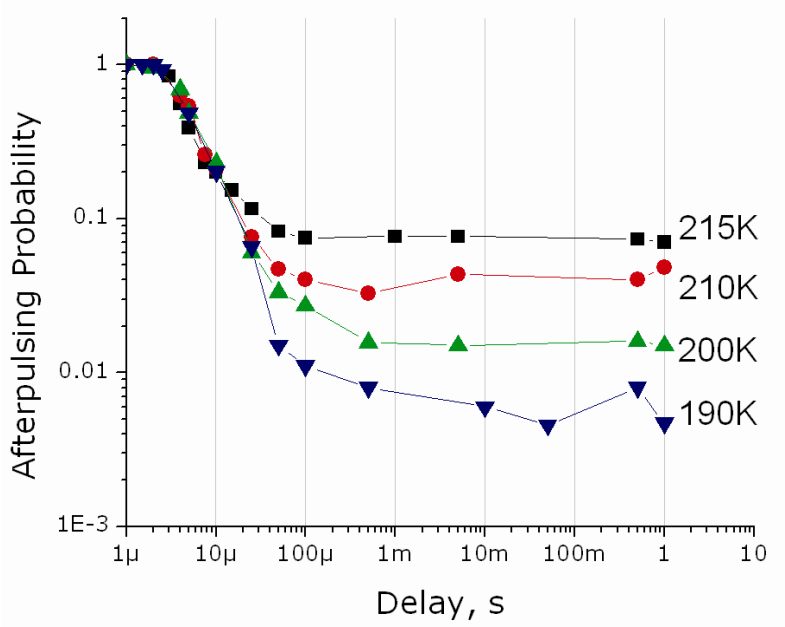

Figure 4.6. Afterpulsing data from a 20 μm diameter SPAD 3-Q device at four temperatures displayed on a logarithmic plot.

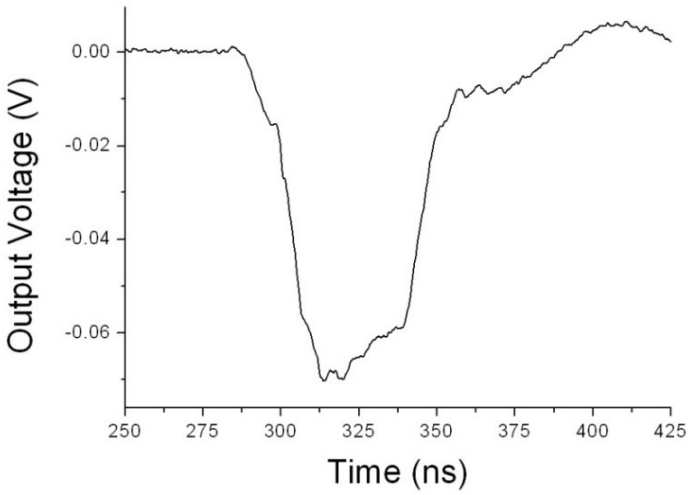

Figure 4.7. SPAD output pulse as seen across a 50 Ω load.

Methods of interpreting these results have varied in the literature. Exponentials have been fitted to the curves to extract decay times [8] [10]. Other authors [11] have measured the time taken for the afterpulsing probability to fall to 10 times the DCR of the device. Later, it will also be shown that these two analysis methods actually give similar results. We chose to adopt the latter technique, since one exponential did not accurately represent the data which may suggest the presence of more than one trap state. Using the afterpulsing probability at the longest delay, we find the point on the curve at which the afterpulsing probability is 10 times this value. This is repeated for each temperature and the data is displayed in an Arrhenius plot as in Figure 4.8 for a SPAD 3Q device. An Arrhenius plot is a plot of the logarithm of the decay time plotted versus the reciprocal of temperature, T, or in our case kT. This gives a straight line from which the activation energy can be extracted.

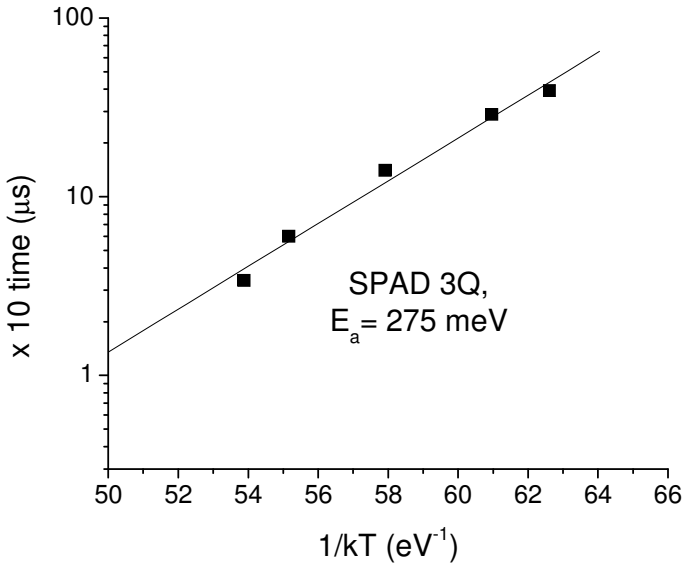

Figure 4.8. Arrhenius plot of time constant versus 1/kT with activation energy of traps extracted and displayed for a 20 µm SPAD 3Q device.

The emission rate ($1/\tau$) of the trapped carriers follows the exponential decay:

$$\frac{1}{\tau} \propto e^{(-\frac{Ea}{kT})} \qquad \text{Equation 4.1}$$

Therefore, if we plot τ *vs.* 1/kT on a semi-log plot, the gradient of the line multiplied by ln (10) gives E_a. For the SPAD-3Q device tested (20 µm diameter), an activation energy of 275 meV was calculated. Although this information has some use, it is a mid-gap state that could be present within any material in the structure hence preventing a localisation of the traps within the device. For this reason, it was decided that other structures could be grown and tested in the same manner.

Two separate test structures were grown for characterisation using the TCCCM as shown in Figure 4.9.

(a)

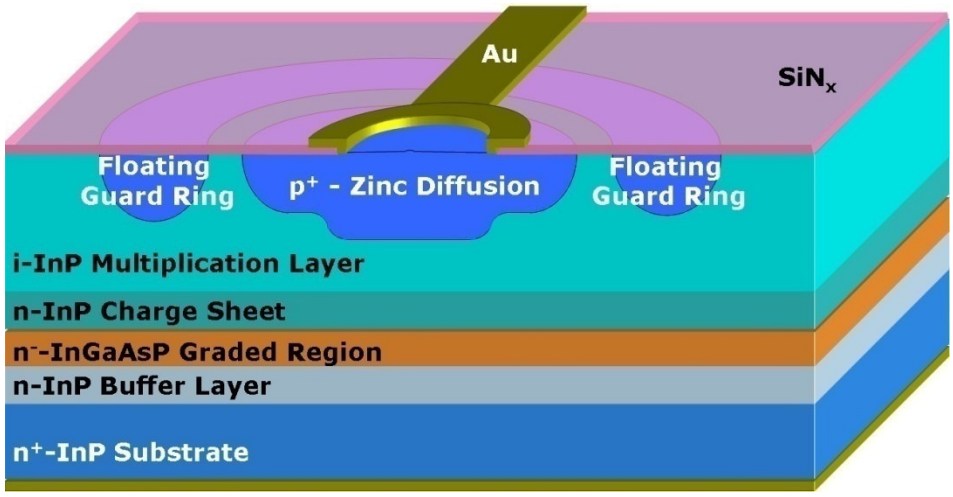

(b)

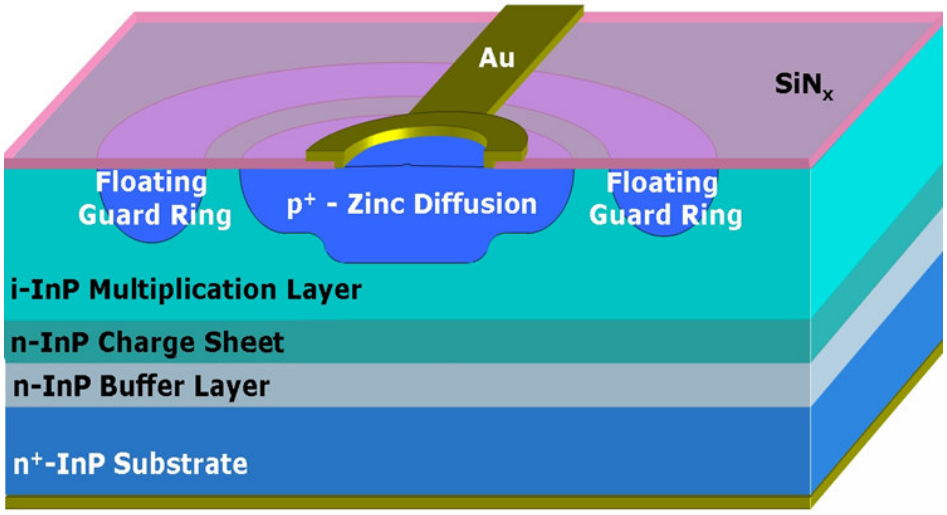

Figure 4.9. Two test structures grown under identical conditions in order to gain further insight into the trapping phenomenon: (a) full SPAD without InGaAs absorption region; (b) full SPAD without InGaAs absorption region nor quaternary graded region.

The two structures facilitate a localisation of the traps by eliminating possible candidates layer by layer. In Figure 4.9 (a) the full SPAD device is shown without the InGaAs absorption region. Unfortunately, problems with device reliability due to cracks in the insulating SiN_x (see Figure 4.10) meant that no reliable results were gained before the writing of this Thesis. The cracks were later found to be caused by poor growth conditions of the SiN_x. Figure 4.9 (b) shows the SPAD structure grown without the absorption nor the graded region and is therefore an all InP device, which will be referred to as "InP-only".

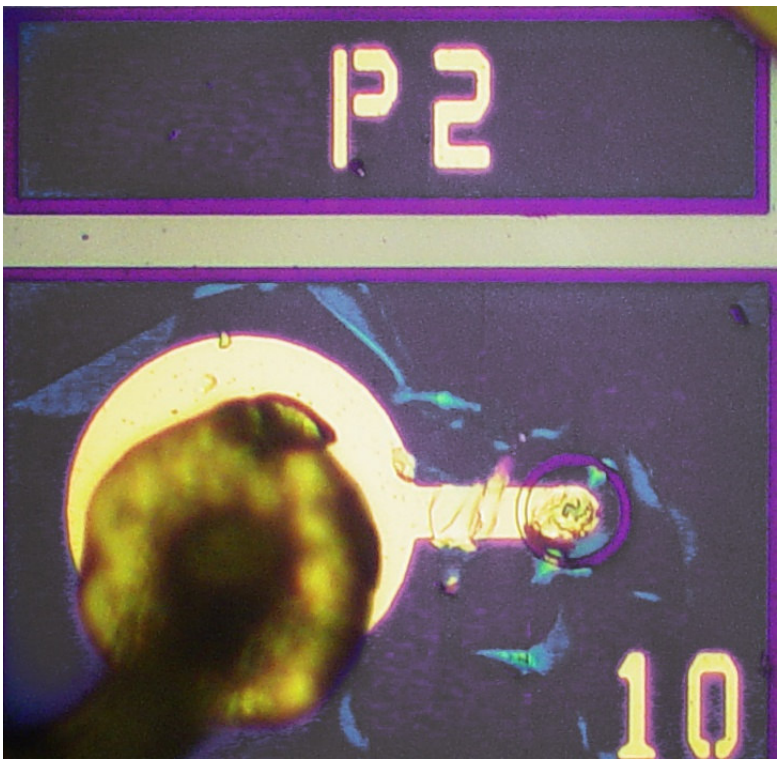

Figure 4.10. Cracks in the SiN_x insulating layer can be seen around the light-blue areas. Colours have been changed to increase contrast hence increasing the crack visibility.

The InP-only devices did not have a DCR dominated by the narrow-gap InGaAs layer and could therefore be characterised at higher temperatures easing the thermal stress on the devices and prolonging their life. Due to the larger bandgap of InP, a 850 nm wavelength laser was used to initiate the avalanche within the first gate. Other than the laser wavelength, the same method was used for afterpulsing analysis on the InP-only device as previous.

Figure 4.11 shows the Arrhenius plot from the InP-only device.

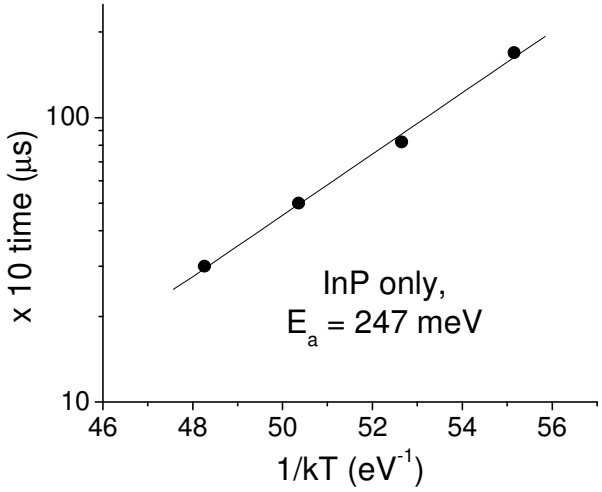

Figure 4.11. Arrhenius plot of time constant versus 1/kT with activation energy of traps extracted and displayed for a 20 µm diameter InP-only device.

Despite the InP-only device not having the absorption region, nor the quaternary graded region, it seems that both devices share a very similar trap activation energy. Logically, it can be assumed that the traps are located somewhere within the InP layers. Possible candidates will be discussed later in this chapter along with a comparison with other values found by other research efforts.

As with the SPDE, DCR and NEP of our custom made SPADs, the trapping of the Epitaxx SPAD was also studied and compared in the same manner. The afterpulsing probability of the Epitaxx device can be seen in Figure 4.12.

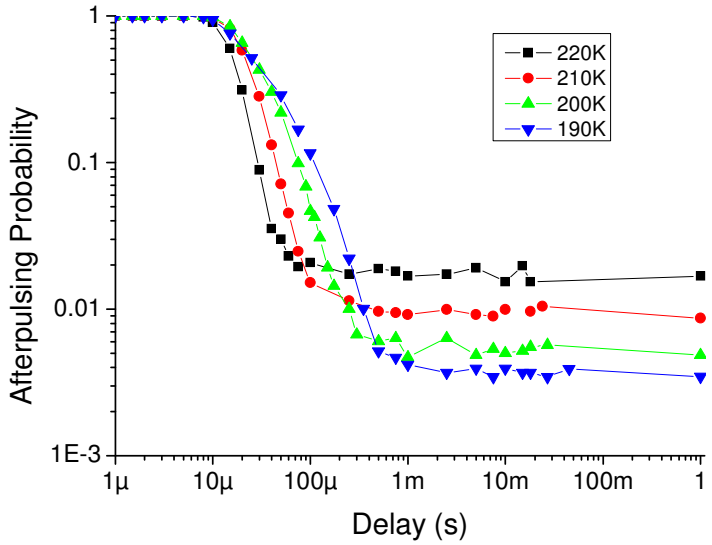

Figure 4.12. Epitaxx afterpulsing probability measured at four different temperatures.

The decay times were then extracted, and for comparison, plotted on the same graph as the full SPAD and the InP-only device in Figure 4.13.

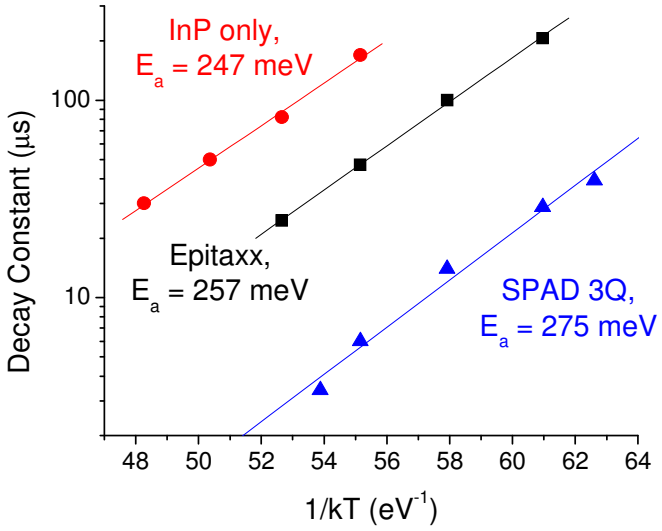

Figure 4.13. Arrhenius plot of the three devices tested with the TCCCM.

The relative difference in times between the devices can be explained by their relative DCR, SPAD 3Q having the highest DCR, followed by Epitaxx and finally InP-only. This results in each device reaching 10 × the base DCR after a longer period of time as the overall DCR of each device decreases as demonstrated in Figure 4.14.

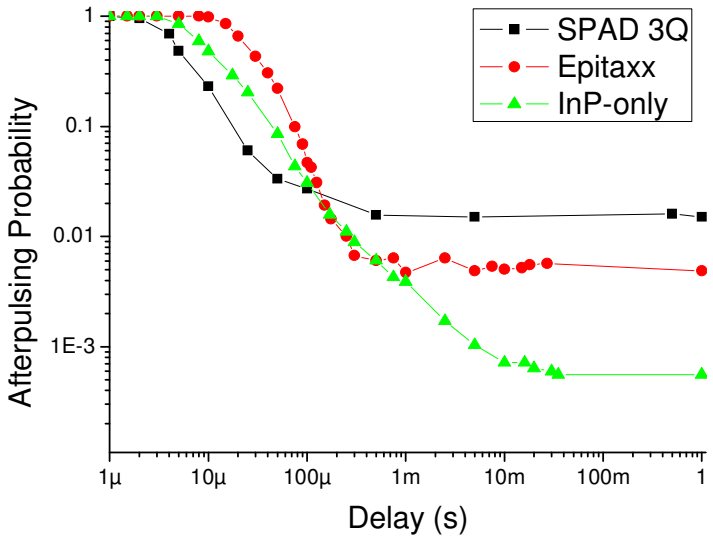

Figure 4.14. Afterpulsing probability of SPAD 3Q, Epitaxx and InP-only devices at 200 K showing the difference in base DCR.

The main result, as shown in Figure 4.13 is that all three devices, despite having different structural features and indeed having been grown in different locations and under different conditions, all have very similar trap activation energies. This key result points to a specific trap location somewhere within the InP layers.

This is a conclusion that has also been reached by other research efforts. Cova *et al.* explain in [9] that the adverse effect of a trap state on afterpulsing is the product of two probabilities: firstly, the probability that the trap state will capture a carrier during the avalanche which is proportional to the avalanche current; secondly, the probability that a released trapped carrier could trigger another avalanche [12]. Considering these two factors, the authors of [9] postulate that trapping within InGaAs can be ignored since there is a high concentration of electrons within the InGaAs layer from the avalanche process and since electrons flow to the back contact they cannot trigger an avalanche. Also, hole traps that are above the multiplication region (near the cathode contact) are not effective at triggering an afterpulse avalanche. Logically, they concluded that the trapping centres are located in the InP multiplication region. The test structures did, however, also enable the investigation of the possibility of trap centres located at the interfaces between adjacent layers within the structure as well as within the layers. Also, in [9] it is reported that hole and electron traps are equally as effective, since an electron released within the multiplication region would also undergo avalanche multiplication, causing an afterpulse, since the hole and electron impact ionisation coefficients are sufficiently similar at these high fields.

Finally, the afterpulsing of the two Princeton Lightwave Inc. devices (see Chapter 3) were also tested in the same fashion to compare trap energies from another source of devices. As mentioned previously, exponentials can be fitted to afterpulsing probability decay curves. This approach seemed to work well with the Princeton Lightwave Inc. devices with two exponentials (1 short, 1 long) being fitted to each curve as demonstrated in Figure 4.15.

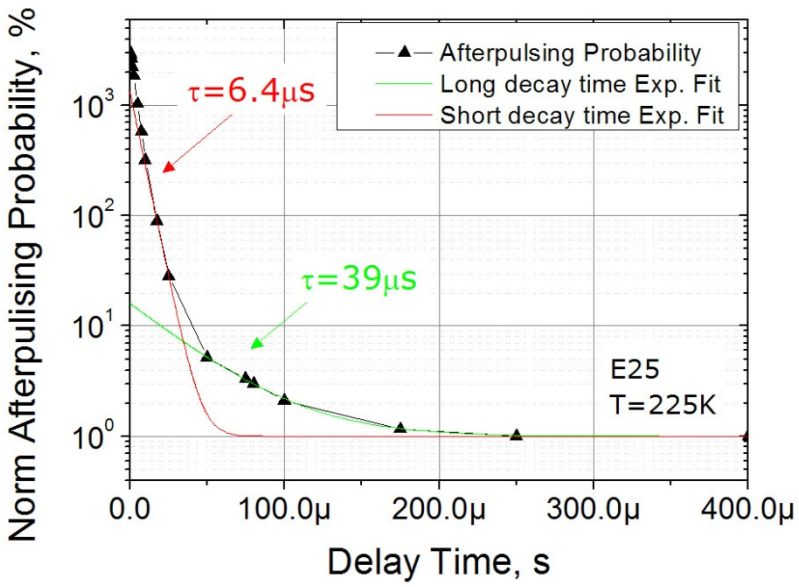

Figure 4.15. Normalised afterpulsing probability of a Princeton Lightwave device at 225 K with two exponentials fitted at each temperature. The short in red, 6.4 μs, and the longer decay in green, 39 μs.

After exponentials were fitted at each temperature, both the short and long exponentials were graphed in an Arrhenius plot to allow the extraction of the activation energy. The devices are named as before- C25 for the central device on the wafer, and E25 for edge device. The method used previously was also employed to allow a comparison between exponential decay times and the time taken for the afterpulsing probability to fall to 10 times the base DCR. In the following two figures these results are compared side by side.

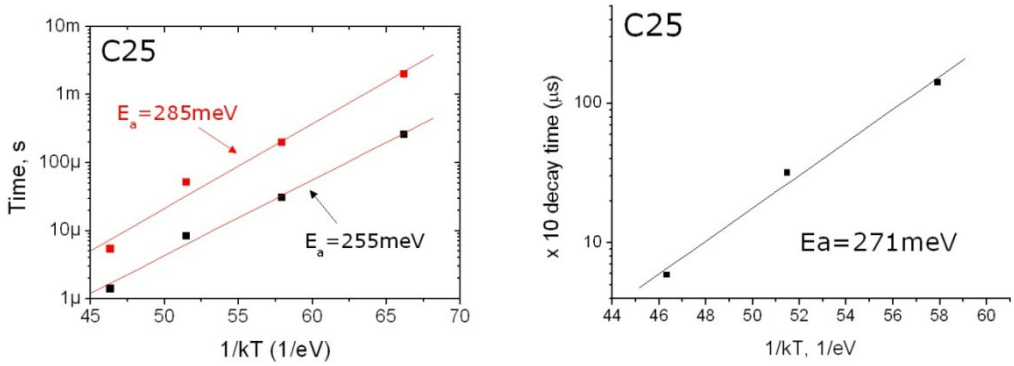

Figure 4.16. On the left is an Arrhenius plot of the two separate decay times extracted from the exponential fits. The black represents the short decay time, and the red shows the long decay time. On the right, is an Arrhenius plot using the method employed for all the previous measurements.

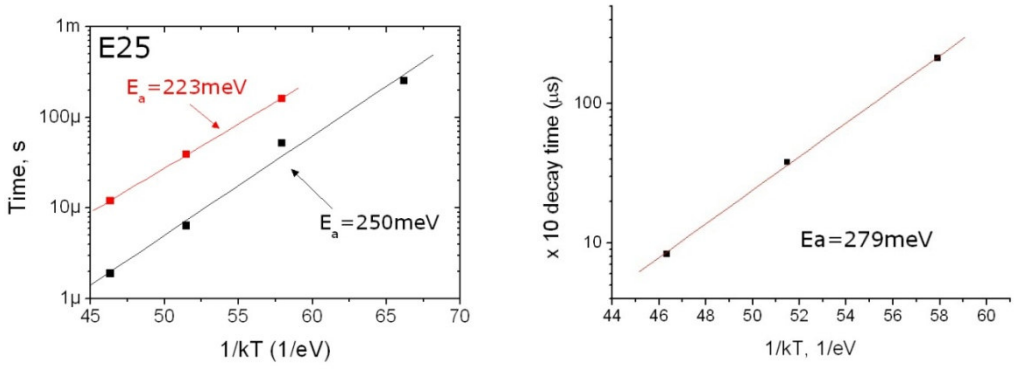

Figure 4.17. As in Figure 4.16 - on the left is an Arrhenius plot of the two separate decay times extracted from the exponentially fits. The black represents the short decay time, and the red shows the long decay time. On the right, is an Arrhenius plot using the method employed for all the previous measurements.

Reassuringly, as can be seen from Figures 4.16 and 4.17, whether the activation energy is calculated from the short or long decay, or indeed the "× 10" method, the answer is consistent. Moreover, the average activation energy found in both Princeton Lightwave Inc. devices is also in the 250 meV region as found previously in the SPAD 3Q device, the InP-only and the Epitaxx. The evidence amassed herein definitively points to a trap state within the InP multiplication region of about 250 meV either above the valence band or below the conduction band, since electron and hole traps are equally as effective at causing an afterpulse [9].

4.4 Comparison of Trap Activation Energy with Other Published Work

Using the DCR hold-off technique as described earlier, has yielded some results for Itzler *et al.* [11] where they found a trap activation energy of 24 meV. Whilst this is an order of magnitude lower than what was found by the Author (this may be due to the method used or the frequency at which the results were taken), other points raised in the paper were of interest. In [11] they postulate that there was a difference in activation energy between edge and central devices caused by their relative positions on the wafer. It was reported that this could suggest that both thermal and tunnelling mechanisms for de-trapping may influence the de-trapping time and that the activation energy of the traps may be sensitive to the internal electric field.

Another interesting point raised was that the de-trapping time would depend on the field within the InP multiplication region between gates, since they found no change in the activation energy at different levels of excess bias. The Author conducted a study in which a Fujitsu APD was analysed using the TCCCM at two different under-biases (V_{DC}) but with different gate amplitudes resulting in the same excess bias despite the difference in DC bias, i.e. the overall output voltage in both measurements was identical even though the DC bias was different. This result can be seen in Figure 4.18 and clearly shows no difference between the two measurements despite a 20 % (of V_{BD}) difference in DC under-bias.

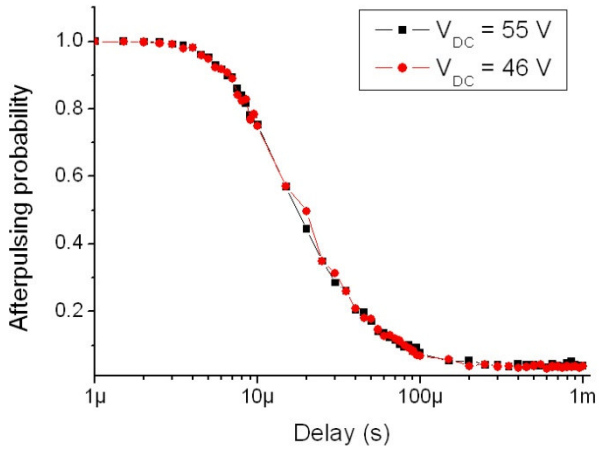

Figure 4.18. Afterpulsing probability of a Fujitsu APD measured using the TCCCM at different under-biases yet retaining the same overall excess bias. Both traces overlap perfectly showing that the underbias has no effect on the de-trapping time.

However, in a paper by Ribordy *et al.* [13] it was reported that a different DC under-bias did, in fact, lead to a difference in afterpulsing probability despite the same overall excess bias being kept constant as shown in Figure 4.19. The data suggests that the higher the amplitude of the gate voltage (hence a lower DC bias) the less severe the afterpulsing. According to their results, the detection efficiency was the same in all measurements (same overall excess bias). In theory then the DCR (the background count rate to which the afterpulsing probability decays) should also remain constant, but, as shown in Figure 4.19, all 4 different gate voltage decay to different DCRs.

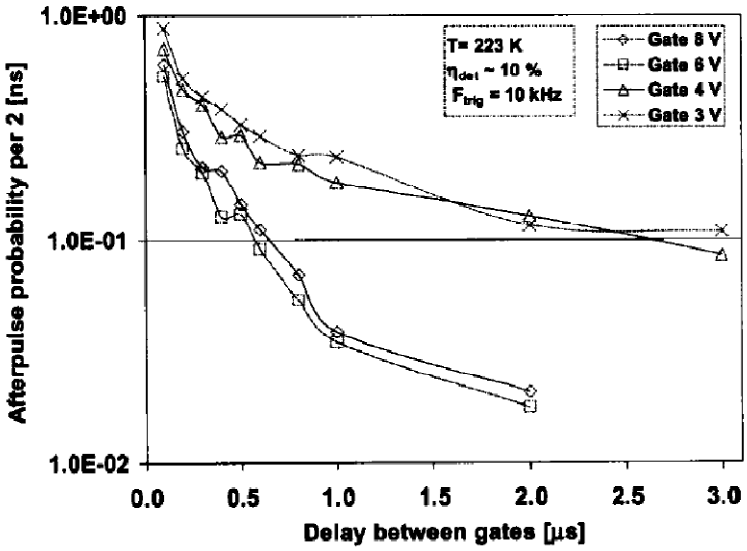

Figure 4.19. Afterpulsing probability of an InGaAs/InP SPAD measured using the hold-off method at 223 K [13]. The different traces relate to different gate voltages. The higher the amplitude of the gate voltage, the lower the DC bias on the SPAD.

What is even more perturbing is that 3 & 4 V gate measurements decay to the same background DCR and 6 & 8 V gate measurements do also. The reason behind this is not clear. It could be postulated that the gate amplitude and relative length may be a factor, since each square wave has a finite rise-time. In the case of our measurements this is limited by the AC gate generator to ~ 4 ns. Referring to Figure 4.20, it can be seen that whilst both gates start at the same time, and have the same rise-time, the low gate & high DC bias combination result in the SPAD experiencing a field above avalanche breakdown sooner and for a longer period of time than the high gate & low DC bias combination. This would indeed result in the same detection efficiency for both cases since the SPAD reaches the same overall excess bias under both conditions. The time during which the device experiences this bias, however, is different hence possibly resulting in a lower DCR rate for the low DC & high gate combination. Furthermore, if the time in which the AC-pulse gate amplitude reaches a maximum is governed by gradient of increase, this will, in turn, further reduce the time during which the high gate & low DC bias combination attains Geiger-mode operation. This does not, however, explain why the 3 & 4 V gate measurements decay to the same background DCR and 6 & 8 V gate measurements do also.

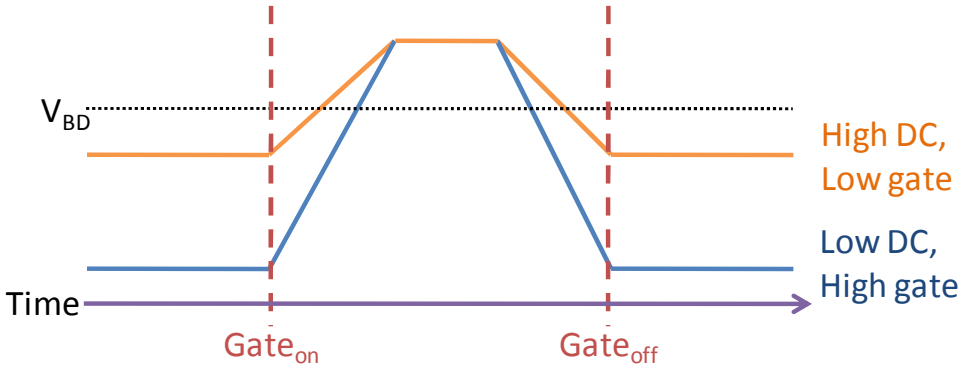

Figure 4.20. Comparison of low DC bias, high gate voltage (in blue), and high DC bias, low gate amplitude (in orange). If the rise time of the square pulse is the same for both gate voltages, then using a high gate amplitude will result in the SPAD experiencing fields above avalanche breakdown (black dotted line) for an effectively shorter period of time compared to the low amplitude gate.

It should also be noted that these afterpulsing measurement were conducted using the "hold-off" method, the Author has not yet attempted employed this technique with high and low gate values. The Author's measurements suggest that for identical gate duration, different gate voltages which result in the same overall excess bias should not decay to different DCRs.

In a paper by Liu *et al.* [14], the TCCCM was used to analyse an InGaAs/InP SPAD at various temperatures. After fitting exponentials to the data with up to four separate decay times per temperature, activation energies were calculated from an Arrhenius plot. Their results ranged from 340 to 370 meV from each fit of the various decay times. This is reassuring since they found similar activation energies from different decay times as was found with the analysis of the Princeton Lightwave Inc. devices.

Another research effort in Lincoln Laboratories at MIT have characterised their InP/InGaAsP detectors in-terms of afterpulsing. In [8] Jensen *et al.* used the TCCCM on a 1.06 μm SPAD in order to extract the activation energy of the dominant trap state. Their measurements at 6 different temperatures (ranging from 250 – 290 K, a smaller range than presented in this Thesis) yielded a trap activation energy of 110 meV. The device structure is slightly different in that the p-region is actually the substrate. Thus, a p-doped substrate (Zn doped) is used instead of a Zn diffusion which may account for the difference in E_a, since the concentration and position of the Zn atoms will be different.

More recently, in [10], Verghese *et al.* repeated these measurements on various structures. Interestingly, the structures were an InGaAs/InP SPAD, an InGaAsP/InP SPAD and an all InP dummy structure. These 3 traces can be seen in Figure 4.20. Reassuringly, their results agree with those measured by the Author insomuch that all three structures have very similar de-trapping times. Verghese *et al.* also state that their hypothesis is that the trap state lies in one of the InP layers.

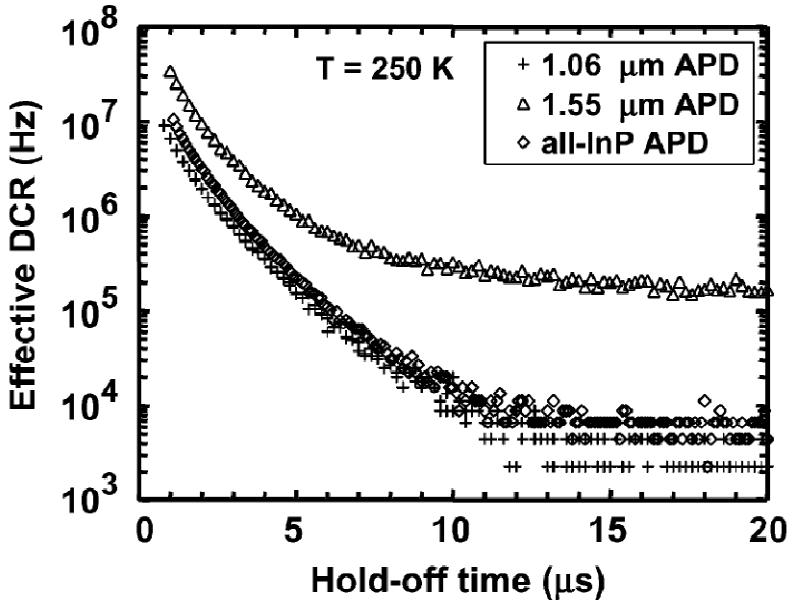

Figure 4.20. Afterpulsing measurements on 1.06 and 1.55 µm SPADs. The InP "dummy" device overlaps the 1.06 µm device results [10].

Further in [10], Verghese *et al.* performed deep level transient spectroscopy (DLTS) on a 3 µm thick InP layer (almost identical to the multiplication region). Verghese reported that a defect state ~ 0.42 eV below the conduction band edge from the DLTS measurements. In the same paper they measured a trap activation energy of 0.15 eV (slightly different from previous reported results). Their hypothesis is that these two values may relate to the same trap, the difference in energy may be due to the near-zero electric field through the device during the DLTS measurements, whereas the afterpulsing measurements must be conducted at an electric field at avalanche breakdown. They suggest that the high field causes barrier lowering thereby making the trap energy appear lower than its actual location within the bandgap. Alternatively, it may be that the concentration of trap level related to afterpulsing is too low for a DLTS system to measure and instead the 0.42 eV state relates to the DCR mechanism.

Deep levels in InP have been studied for many years and the literature has an abundant choice of different levels caused by various defects, impurities, dislocations and vacancies. W. A. Anderson and K. L. Jiao from the State University of New York at Buffalo wrote a comprehensive study on this subject [15]. This publication is a compilation of many papers detailing trap states within InP and their relative causes. Different methods of growth are covered from Liquid Phase Epitaxy (LPE) to MOCVD and various dopants/ impurities are also studied. Although there is a lot of useful information contained in this paper, it is very dependent on interpretation, especially if the value measured by DLTS is different to that measured using the afterpulsing technique. One of the most interesting is the trap levels caused by zinc diffusion as a p-type dopant in InP. The authors of [16] explain that a number of trap states were seen in bulk n-type InP caused by the Zn diffusion with electron traps at $E_c - 0.30$ eV, $E_c - 0.35$ eV, $E_c - 0.49$ eV, and $E_c - 0.59$ eV. Hole traps were found at $E_v + 0.27$ eV and $E_v + 0.64$ eV. It is possible that any of these values could be responsible for the traps within the InP, since there will be some Zn atoms that diffuse further into the multiplication region than the main diffusion front. For an accurate prediction of which trap state causes the trapping phenomenon, one would have to ascertain the difference in trap state between near-zero field DLTS and high-field afterpulsing measurements. Other trap energies presented are apparent due such problems as excess phosphorus, interstitials, electro-thermal stress, various contaminants in all growth methods (Fe in MOCVD) and general growth defects.

4.5 Conclusion

The afterpulsing phenomenon was explained in terms of its deleterious effects on the maximum permissible gating frequency and count rate. Methods of analysing afterpulsing in SPADs were described. The time correlated carrier counting method (TCCCM) was chosen to conduct the afterpulsing analysis since it provides a more sensitive and accurate measurement technique.

Various device structures were tested using the TCCCM in order to examine the afterpulsing phenomenon. A SPAD-3Q device was found to have a trap activation, E_a, of 275 meV. The Epitaxx EPM239AA, despite being grown under completely different conditions had an E_a = 257 meV. An all-InP device was also characterised to confirm that the main trap state involved in the afterpulsing mechanism is in the InP multiplication layer. The InP only device yielded an E_a = 247 meV verifying that the trap state in somewhere within the InP multiplication region. Finally, two Princeton Lightwave Inc. devices were tested for completeness. They both gave an $E_a \sim 250$ meV.

Although this research effort has been thorough, it is evident that a lot more work needs to be done in order to find the exact cause of the traps that are the origin of such a bottle-neck for near IR single-photon detection. With careful growth conditions it may be possible to reduce the number of trap states, but the authors of [9] point out that it may be possible to entirely replace the InP multiplication region with a different material. The base starting point for all InGaAs/InP SPAD was the InGaAs/InP APD. However, there are several requirements for APDs that are not essential for SPAD operation. It was therefore not possible to replace the multiplication region in APDs due to the requirement for having a low or high k (hole impact ionisation coefficient / electron impact ionisation coefficient) to increase device speed. In a SPAD, though, the k value is not important since the avalanche is self-sustaining and is quenched either passively or actively.

Until a suitable alternative is found, such as InGaAs fusion-bonded to an Si multiplication layer [17] [18], there are serious endeavours in using InGaAs/InP detectors in different ways to lessen the effects of afterpulsing. The next Chapter will detail one of these emerging methods.

4.6 References

[1] P.A. Hiskett, G. Bonfrate, G.S. Buller and P.D. Townsend, *Eighty kilometre transmission experiment using an InGaAs/InP SPAD-based quantum cryptography receiver operating at 1.55 μm,* Journal of Modern Optics, **48** (13), 1957 - 1966 (2001)

[2] P.A. Hiskett, G.S. Buller, Private communication.

[3] A. Lacaita, F. Zappa, S. Cova, and P. Lovati, *Single-photon detection beyond 1 μm: Performance of commercially available InGaAs/InP detectors*, Applied Optics, **35** (16), 2986 - 2996 (1996)

[4] C. Gobby, Z.L. Yuan, A.J. Shields, *Quantum key distribution over 122km of standard telecom fiber*, Applied Physics Letters, **84** (19), 3762 - 3764 (2004)

[5] D. Stucki, G. Ribordy, A. Stefanov, H. Zbinden, J.G. Rarity, T. Wall, *Photon counting for quantum key distribution with Peltier cooled InGaAs/InP APDs*, Journal of Modern Optics, **48** (13), 1967 - 1981 (2001)

[6] X. Jiang, M.A. Itzler, R. Ben-Michael, and K. Slomkowski, *InGaAsP–InP avalanche photodiodes for single-photon detection,* IEEE Journal of Selected Topics in Quantum Electronics, **13** (4), 895 - 905 (2007)

[7] S. Cova, A. Lacaita, and G. Ripamonti, *Trapping phenomena in avalanche photodiodes on nanosecond scale*, IEEE Electronics Device Letters, **12** (12), 685 - 687 (1991)

[8] K.E. Jensen, P.I. Hopman, E.K. Duerr, E.A. Dauler, J.P. Donnelly, S.H. Groves, L.J. Mahoney, K.A. McIntosh, K.M. Molvar, A. Napoleone, D.C. Oakley, S. Verghese, C.J. Vineis, and R.D. Younger, *Afterpulsing in Geiger-mode avalanche photodiodes for 1.06μm wavelength*, Applied Physics Letters, **88**, 133503 (2006)

[9] S. Cova, A. Tosi, A. Gulinatti, F. Zappa and M. Ghioni, *Avalanche Diodes and Circuits for Infrared Photon Counting and Timing: Retrospect and Prospect*, IEEE LEOS Newsletter, **Oct**, 25 - 28 (2006)

[10] S. Verghese, J.P. Donnelly, E.K. Duerr, K.A. McIntosh, D.C. Chapman, C.J. Vineis, G.M. Smith, J.E. Funk, K.E. Jensen, P.I. Hopman, D.C. Shaver, B.F.

Aull, J.C. Aversa, J.P. Frechette, J.B. Glettler, Z.L. Liau, J.M. Mahan, L.J. Mahoney, K.M. Molvar, F.J. O'Donnell, D.C. Oakley, E.J. Ouellette, M.J. Renzi, and B.M. Tyrrell, *Arrays of InP-based Avalanche Photodiodes for Photon Counting*, IEEE Journal of selected topics in Quantum Electronics, **13** (4), 870 - 886 (2007)

[11] M.A. Itzler, R. Ben-Michael, C.-F. Hsu, K. Slomkowski, A. Tosi, S. Cova, F. Zappa, and R. Ispasoiu, *Single-photon avalanche diodes (SPADs) for 1.5μm photon counting applications*, Journal of Modern Optics, **54**, 283 - 304 (2007)

[12] W.O. Oldham, R.R. Samuelson, P. Antognetti, *Triggering Phenomena in Avalanche Diodes*, IEEE Transactions on Electronic Devices, **19**, 1056 - 1060 (1972)

[13] G. Ribordy, N. Gisin, O. Guinnard, D. Stuck, M. Wegmuller, H. Zbinden, *Photon counting at telecom wavelengths with commercial InGaAs/InP avalanche photodiodes: Current performance*, Journal of Modern Optics, **51** (9), 1381 - 1398 (2004)

[14] M. Liu, C. Hu, X. Bai, X. Guo, J.C. Campbell, Z. Pan, and M.M. Tashima, *High-Performance InGaAs/InP Single-Photon Avalanche Photodiode*, IEEE Journal of Selected Topics in Quantum Electronics, **13** (4), 887 - 894 (2007)

[15] W.A. Anderson and K.L. Jiao, *Indium Phosphide and Related Materials: Processing, Technology, and Devices*, A. Katz, Ed. Artech House, Bostan, MA, 75 - 102

[16] S.R. McAfee, F. Capasso, D.V. Lang, A. Hutchison, and W.A. Bonner, *A study of deep level in bulk InP by transient spectroscopy*, Journal of Applied Physics, **52** (10), 6158 - 6165, (1981)

[17] Y. Kang, P. Mages, A.R. Clawson, P.K.L. Yu, M. Bitter, Z. Pan, A. Pauchard, S. Hummel, and Y.H. Lo, *Fused InGaAs–Si Avalanche Photodiodes With Low-Noise Performances*, IEEE Photonics Technology Letters, **14** (11), 1593 - 1595 (2002)

[18] A.R. Hawkins, W. Wu, P. Abraham, K. Streubel, and J.E. Bowers, *High gain-bandwidth-product Silicon heterointerface photodetector*, Applied Physics Letters, **70**, 303 – 305 (1996)

Chapter 5 - Methods for the Reduction of Afterpulsing in InGaAs/InP Single-Photon Avalanche Diodes

5.1 Introduction

In Chapter 4, the afterpulsing phenomenon seen in InGaAs/InP SPADs was described and its detrimental effects on device performance were reported. Whilst trap activation energies have been found and possible causes discussed, we have not yet made changes to the growth and fabrication processes to eradicate, or at least lessen, the trap concentration. Instead, a variety of novel techniques of electronically addressing the photon counting detector have been developed in order to lessen the afterpulsing effects. All of these methods rely on limiting the charge that flows through the SPAD per detection, or dark event, hence reducing the amount of traps states filled resulting in lower afterpulsing probabilities. Some of the methods have been specifically developed with applications like QKD in mind. The gating schemes for these methods involve periodic gating with short electrical pulses (typically ~ ns duration) and are more suited to QKD than other applications. Other schemes, such as the "sub-Geiger" method, investigated in this chapter, allow the device to operate in "free-running" mode making it better suited to TRPL and lidar. First, a short review of other reported means of afterpulsing reduction will be given, followed by an in-depth description of sub-Geiger mode operation and the results yielded.

5.2 Review of Afterpulsing-Reduction Methods

Other than introducing a prohibitively long dead time between detection periods to allow the release of trapped carriers, the main approach used to reduce the effects of the afterpulsing phenomenon is to limit the overall charge per event. An alternative approach of photo-ionisation of trapped states has also been reported and will be discussed later. Normal gated quenching is not ideal since the avalanche is not quenched until the gate is switched off, hence the amount of charge flow per event will increase as the gate length is increased. However, the use of an active quenching circuit (AQC) in conjunction with gating makes a significant difference to the severity of the afterpulsing as shown in Figure 5.1. An AQC, as explained in Chapter 2, is an electronic circuit which quenches the avalanche current shortly after (~ ns) it has been triggered, instead of at the end of the gate-on interval. Figure 5.1, a direct comparison

between gated and AQC gated operation for the same device, shows the significant advantage of the AQC.

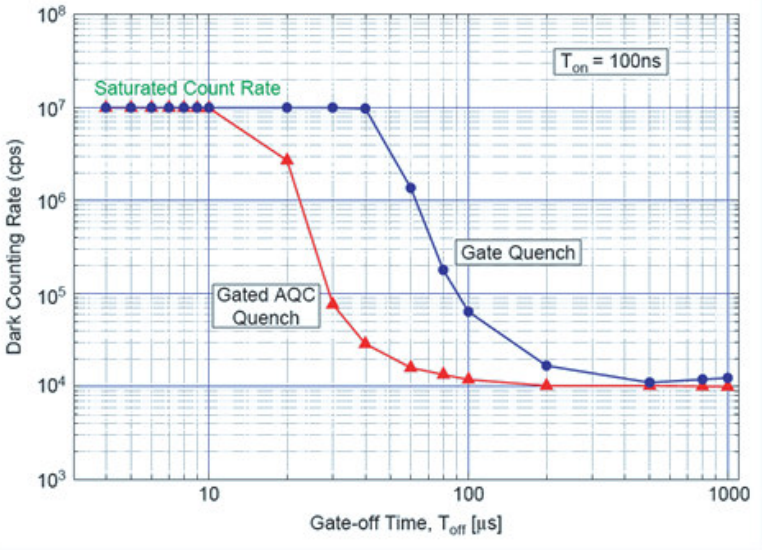

Figure 5.1. Afterpulsing probability comparison between standard gated mode of operation of an InGaAs/InP SPAD (where the gate-on period is 100 ns) and gated mode with AQC (where the avalanche is quenched within a few ns) [[1]].

Use of an AQC allows a reduction in afterpulsing probability of about 2 orders of magnitude at dead-times below 60 µs resulting in a device capable of exceeding the maximum count rate of a standard gated SPAD. A similar method was reported by Liu *et al.* in [2].

As explained in Chapter 2, QKD has placed a great demand upon detectors for fast and efficient single-photon detection at λ = 1550 nm. Using InGaAs/InP APDs in standard telecoms applications, data transfer rates in the Gb/s region are readily achievable. With standard gating, as described in the previous chapters, or even AQC gated operation, Gb/s data rates are completely out of the question for QKD using InGaAs/InP APDs in Geiger-mode. Tens of MHz gating frequencies have been reported in InGaAs/InP APDs in Geiger-mode by Voss *et al.* [3] for example. The authors of [2] used a short gate (< 1 ns) and a series of amplifiers, comparators and bandpass filters, to yield an SPDE of 14 % with only 0.2 % probability of a dark count per gate and 0.2 % afterpulsing probability at room temperature. Recently, there have been at least two separate initiatives using different gating methods to exploit InGaAs/InP SPADs as described below.

5.2.1 Sinusoidal Gating

Firstly, Namekata *et al.* [4] used the setup shown in Figure 5.2 with a sinusoidal gating scheme to operate an InGaAs/InP SPAD at 800 MHz at λ = 1550 nm. Gated passive quenching is utilised (GPQC in Figure 5.2), where the gate signal is a sine wave of frequency ω_g. If an avalanche is not triggered, the gate signal is outputted from the GPQC, but since the APD's resistance is much greater than R_O, the signal is heavily attenuated. This signal is then removed using a band elimination filter (BEF in Figure 5.2) centred at ω_g. The avalanche signal itself has many frequency components which pass through the BEF and can be detected. The gating at 800 MHz was accomplished at -35 ºC which is feasible due to the actual "gate on" time being much < 1 ns hence limiting the dark count probability.

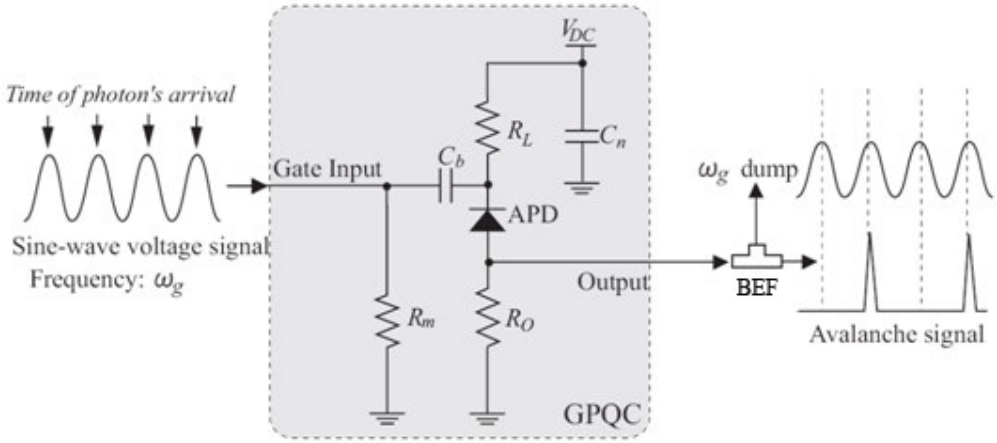

Figure 5.2. System schematic for a sinusoidally gated InGaAs/InP SPAD along with associated electronics where GPQC is the gated passive quenching circuit and BEF is a band elimination filter [4].

By limiting the charge passing through the device per avalanche event, Namekata *et al.* achieved 800 MHz gating, with 8.5 % SPDE, only 6 % afterpulsing probability with a dark count probability of 9.2×10^{-6} per gate. The maximum count rate achievable was estimated to be 6.5 Mcs^{-1} when the average incident photon number was 0.1. The gate itself was shorter than 500 ps, resulting in as few as 10^5 electrons passing through compared to ~ 10^7 - 10^8 electrons under normal gating conditions. Consequently, a discriminator level 2 ~ 3 orders of magnitude lower can be utilised compared to standard square-wave gating. This would not be possible in square-wave gating due the capacitive response of the SPAD, which would be of greater amplitude than the avalanche signal itself.

The following method, however, uses the capacitive response within the technique in order to discriminate the avalanche signal.

5.2.2 Self-Differencing Technique

Researchers at Toshiba, UK, have developed a high-speed gating technique which senses extremely weak avalanche pulses that are hidden within the SPAD's capacitive response. Figure 5.3 demonstrates how this works. When a gate is applied to the SPAD, Figure 5.3 (a), a positive peak (at the start of the gate) and a negative peak (at the end of the gate) are seen due to the charging and discharging of the SPAD's finite capacitance as shown in Figure 5.3 (b). No avalanche could be discriminated within this capacitive response, but when an identical (but shifted by one clock cycle) signal (Figure 5.3 (c)) is subtracted from the original, the result is as seen in Figure 5.3 (d). In response to an avalanche event a positive and negative peak are seen in the subtraction, which means a thresholding trigger could be positive or negative. This is useful in many TCSPC applications where CFD units often require a specific polarity input. It should be noted that the signal in Figure 5.3 (d) has been magnified 10 times, and is hence 10 times smaller in magnitude than the capacitive response of the diode. Under normal conditions, an avalanche would have to be 20 times stronger to be detected without removing the capacitive response. Unfortunately, numerical subtraction is not ideal due to the high rates at which these systems are operated. Instead, the authors of [5] have designed a circuit as set-out in Figure 5.3 (e) which takes the SPAD output, splits it into two equal signals, delays one by a clock-cycle, then subtracts one from the other by means of the differencer to give the output as in Figure 5.3 (f). This was reported to give a 21 dB suppression of the capacitive response.

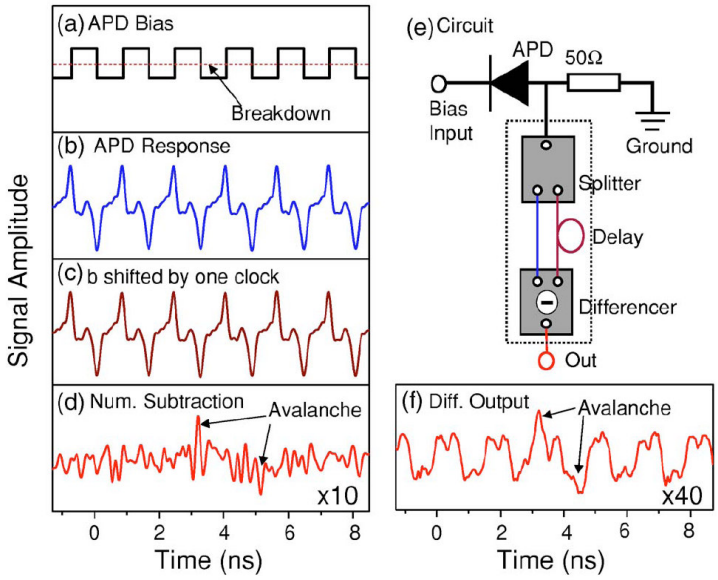

Figure 5.3. (a) SPAD bias gating, (b) APD capacitive response, (c) as (b) but shifted by one clock-cycle, (d) numerical subtraction of (b) and (c), (e) self-differencing circuit, (f) differencing circuit output [5].

With this system the Authors of [5] were able to gate the detector at 1.25 GHz, with an SPDE of 10.8 %, an afterpulsing probability of 6.16 % and a count rate that saturated at 100 MHz.

An effort to reproduce a similar system was briefly attempted by the Author, to test the method. Numerical subtraction was performed by an oscilloscope. The main problem encountered was the pulse-distortion introduced by the delay. This was due to the lower clock frequency used, which was ~ MHz. At low clock frequencies, 1 clock period is of a longer duration, therefore delaying a pulse by one clock period requires a longer delay cable which detrimentally alters the pulse shape due to the additional impedance of the cable. The concept was shown to work but without building a differencing circuit, no results in terms of SPDE, DCR and jitter could be reported. Figure 5.4 shows a demonstration of what was accomplished using a splitter, delay cable and an oscilloscope capable of performing subtraction. The black signal is the capacitive response of the SPAD. The red signal is the capacitive response of the previous clock-cycle delayed by one period. The blue is the result of the subtraction of red minus black. Within the black trace, it is possible to observe a small negative peak (indicated by the black arrow) which is "hidden" (undetectable with standard thresholding techniques) by the capacitive response of the SPAD. Coincident with the small black peak, there is a positive blue peak indicated by the blue arrow which shows the subtraction of the original signal from the delayed signal. The blue signal alone can

then be inputted into a photon counting card and the avalanches discriminated and counted.

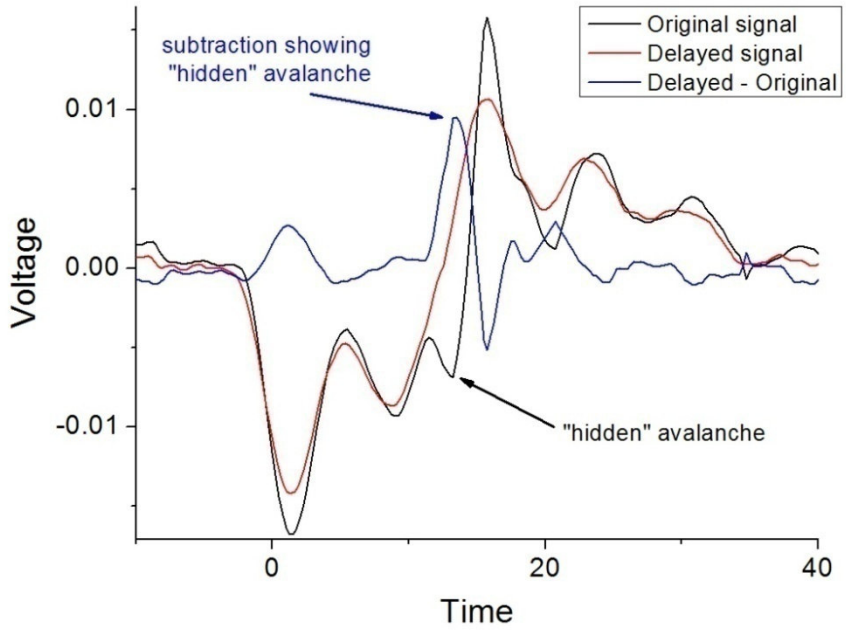

Figure 5.4. SPAD operation using the self-differencing method as seen on an oscilloscope and as described in the text. The black and red lines represent the SPAD's capacitive response for a certain clock period (black) and the previous period (red) delayed such that they can be numerically subtracted to give the blue trace showing a positive peak in response to a "hidden" avalanche.

Both methods discussed previously, sinusoidal gating and self-differencing, permit impressive gating frequencies and a reduction of the afterpulsing phenomenon. Since the gates are so short in both cases, these methods are more suited for use in a QKD system where the precise timing window of potential photon (or bit) arrivals is known. Unfortunately, for applications like TRPL where lifetimes may be in the 1-5 ns region, and ranging when distances to targets are unknown, such a gating system is not suitable. As mentioned previously, a "staring" detector in free-running mode would be far more desirable. The next section reports an attempt to utilise an InGaAs/InP SPAD in such a manner.

5.2.3 Sub-Geiger Single-Photon Detection

If a SPAD is operated at a voltage below that at which avalanche breakdown occurs, referred to sub-Geiger mode, it is possible to detect a single-photon from the multiplied response. This effect has been reported before using a Si APD below V_{BD} to lessen the effects of afterpulsing [6] although the technique then seemed to be

abandoned, perhaps due to better material quality and more complex fabrication methods that yielded Si SPADs with fewer trap states which permitted operation at, or close to, room temperature. One early example in the literature at the optical telecommunications wavelengths [7] makes use of a different InGaAs device structure, incorporating InAlAs as the material in which multiplication takes place. The structure can be seen in Figure 5.5. along with the operation concept.

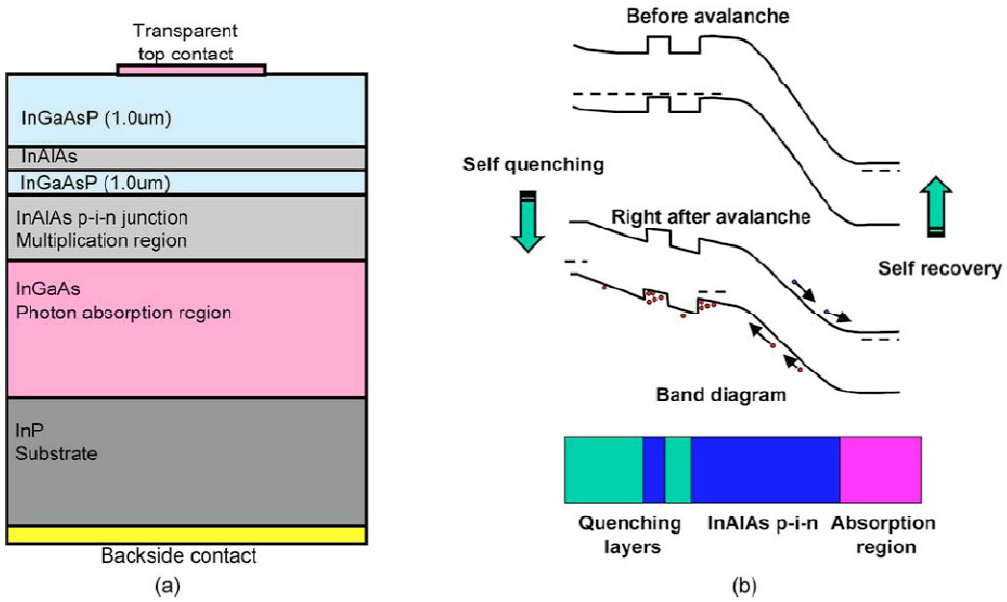

Figure 5.5. (a) InGaAs/InAlAs SPAD layer structure. (b) Operating concept demonstrating the self-quenching and self-recovery process [7].

Referring to Figure 5.5 (b) and according to [7], a photon is absorbed in the InGaAs and an electron-hole pair is created. The electron flows to the back contact and the hole triggers the avalanche process in the multiplication region. The avalanche multiplication results in many holes moving towards the cathode, which are referred to as "hot" holes due to the large amounts of kinetic energy they gain from the high electric field. These hot holes are "cooled" as they pass through the p-type InAlAs region which has a lower field and are subsequently stopped by energy barriers caused by the InGaAsP/InAlAs interfaces. The InGaAsP quaternary is engineered so that it has an 80 meV valence band offset compared to InAlAs which is sufficient to obstruct the passage of the cooled holes. The holes then collect at the InAlAs/InGaAsP interfaces and cause a rapid decrease in the electric field within the multiplication region due to the shielding effect of the amassed holes. The impact ionisation rate is thus perturbed by the drop in electric field hence quenching the output signal. Once the output has been quenched, the holes escape via thermal excitation and tunnelling, resetting the

device for the detection of a subsequent photon. The device is thus self-quenching and self-recovering. The self-quenching (the duration of the photon-induced pulse) is about 30 ns, and the reset an extra 300 ns (the time taken for the holes to tunnel through or thermally jump the barrier). Although this paper claims sub-Geiger mode operation, it is likely that this device is actually a Geiger mode device with self-quenching given the length of time taken for the quench and reset. Also, the output pulse seems to be of a large amplitude for sub-Geiger mode operation (80 mV compared to just ~ 5 mV for the sub-Geiger mode measurements detailed in Section 5.3). Significantly, the paper does not quote any values for DCR or SPDE.

5.2.4 Photo-Ionisation of Trapped Carriers

Whilst all of the aforementioned afterpulsing reduction methods rely on limiting the charge per event, there is one paper that reports the use of a sub-bandgap laser to clear the trap states of carriers. The approach is relatively simple, as shown in Figure 5.6.

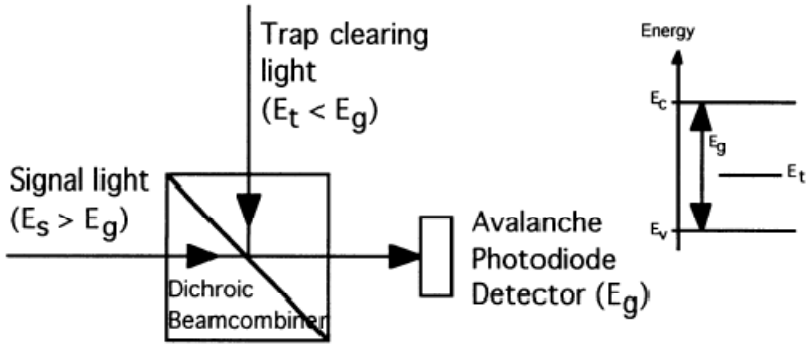

Figure 5.6. A trap-clearing light (λ ~ 1.95 μm) is coupled with the signal light and both are incident on the detector where the energy of the trap-clearing light is less than that of the bandgap, E_g [8]

Using a dichroic beamcombiner as shown in Figure 5.6, sub-bandgap light is coupled into the signal light and is incident upon the detector. The photo-ionisation of trapped carriers results in a depopulation of the trap-states in a shorter period of time than thermal/tunnelling depopulation. Since the publication of this paper [8] there have been several attempts, by numerous research efforts, to gain results using this method although none have been reported in the scientific literature.

5.3 Sub-Geiger Measurements with an InGaAs/InP SPAD

5.3.1 Sub-Geiger Mode Operation and Characterisation Method

For the following measurements, a Princeton Lightwave 25 μm diameter InGaAs/InP SPAD was used. The setup is shown in Figure 5.7. The SPAD is reverse biased by a constant DC voltage through a resistor R_S, which was initially 10 kΩ, and the output is measured across a 50 Ω resistance, usually an oscilloscope or the input of a photon counting card. The use of R_S was essential for the protection of the SPAD in case the operating voltage was increased to a point where self-sustaining avalanche breakdown may occur. When the SPAD is in stand-by, there is no current flowing in the circuit and the bias across the SPAD is V_{DC}. If an avalanche is triggered, current will flow through R_S thus reducing the voltage across the diode which quenches the avalanche and avoids damage being done to the diode. The selection of the resistance R_S, is significant because it will affect the time taken for the bias to recover to its operational level, hence limiting the maximum permissible count rate. The size of R_S also plays a key role in determining the maximum voltage that can be placed on the SPAD, affecting the maximum SPDE achievable. It will be shown later that there is a trade-off between these two factors. Four resistors were chosen for testing as R_S: 10 kΩ, 100 kΩ, 1MΩ, and 10MΩ.

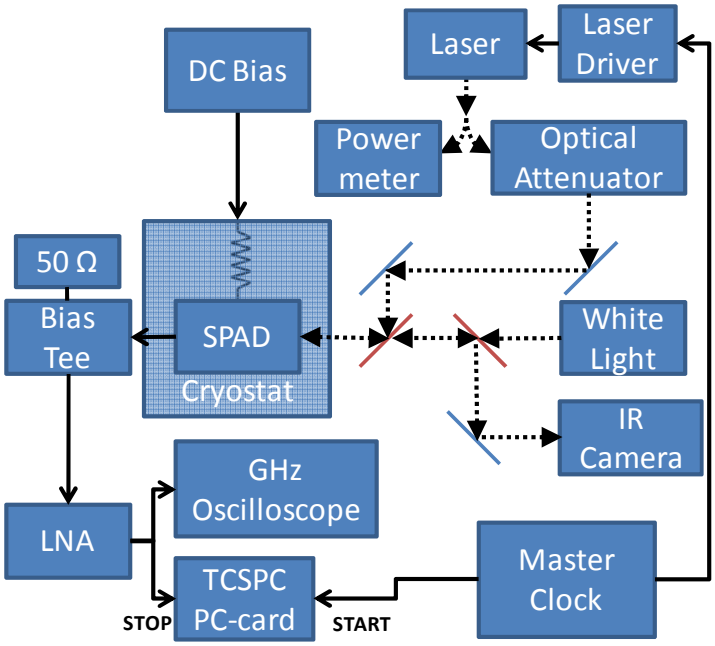

Figure 5.7. Schematic sub-Geiger mode setup showing electrical connections (solid lines) and optical paths (dotted lines). The blue slanted lines represent mirrors, whilst the red represent partially reflecting pellicle beam-splitters. LNA is a low-noise amplifier. The laser is a < 50 ps pulsed laser diode at λ = 1550 nm.

Figure 5.7 shows a schematic of the experimental setup. The master clock was set to a frequency of 1 MHz which served as the trigger for the laser driver for the SPDE measurements. When calculating the maximum count rate as detailed later, a 40 MHz clock was used. A λ = 1550 nm pulsed laser diode was coupled into a 50/50 fibre splitter. One arm of the splitter was used to monitor the laser power and the other fed into an optical attenuator to ensure that in a typical SPDE measurement, on average, less than one photon per pulse arrived at the SPAD. A dewar-cryostat housed the SPAD to enable temperature tuning of the detector between 77 K and 300 K. A white light channel was also present in the optical setup along with an infrared camera for alignment purposes. The DC voltage was applied through sub-miniature coaxial cable and was variable in 10 mV steps. This was necessary since the SPDE and DCR were very sensitive to the bias level as the SPAD was biased so close to breakdown. The output was sensed through the capacitive arm of a bias tee to alleviate any feedback to the SPAD which would perturb the bias level and hence the effective gain. The inductive arm of the bias tee was terminated with a 50 Ω shunt, again to stop reflections. Since the peak output voltage from the SPAD was so small ~ mV in amplitude (see Figure 5.8), a low noise amplifier was employed to enable compatibility with a Becker & Hickl SPC-600 photon counting card. This did, however, mean that the total current flowing through the device per event was greatly reduced: typically, in Geiger mode ~ 5×10^8 electrons pass through the device per event, whereas in sub-Geiger mode, the average is reduced to approximately 1×10^6 per event. Such a large reduction per event results in a significant reduction in the afterpulsing phenomenon, as shown later in the Chapter. The amplitude and duration of the output pulse with different values of R_S remained constant (for equivalent DC voltage biases), although the relative electrical noise in the output signal seemed to be slightly reduced as shown in Figure 5.9.

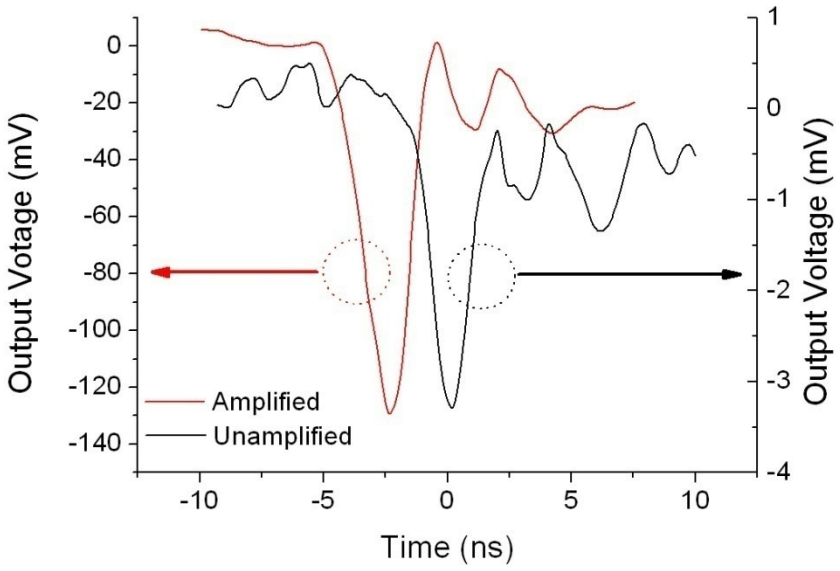

Figure 5.8. Sub-Geiger SPAD output with an R_S value of 10 kΩ. The raw output, across the 50 Ω load, is in black and relates to the right-hand y-axis, amplified signal is in red and relates to the left-hand y-axis. The outputs were shifted temporally for clarity. The number of electrons passing through the device in sub-Geiger mode per event is ~ 1 × 10^6.

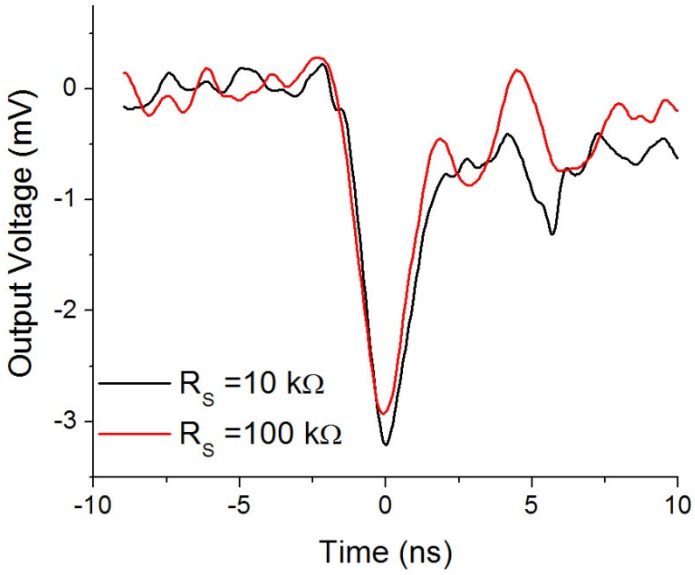

Figure 5.9. Comparison of output pulses of an InGaAs SPAD operated in sub-Geiger mode for two different values of R_S. The black trace shows the output pulse of the SPAD when R_S is 10 kΩ, and the red when R_S is 100 kΩ. Throughout a number of trials, the 100 kΩ measurements consistently appeared less affected by electrical noise.

It is interesting to examine how the gain of the SPAD in sub-Geiger mode changes with voltage to learn how precisely the DC bias must be controlled in order to keep the gain constant. The same is true for controlling the temperature as the breakdown voltage changes by 0.17 V/K [9]. Figure 5.10 demonstrates the change in gain as the DC bias is increased by 100 mV. In the measurements described herein it was possible to control the DC bias in 10mV steps, this accuracy is sufficient to keep the gain steady to within ~ 3 %. Also, the temperature stability is better than 0.1 K, therefore the breakdown voltage will vary by a maximum of ~ 20 mV, resulting in a maximum change in gain of ~ 6 %. In practice however, the use of thresholding circuitry, and in particular a CFD, means that voltage and temperature instabilities of such a magnitude will have little effect on measured device performance.

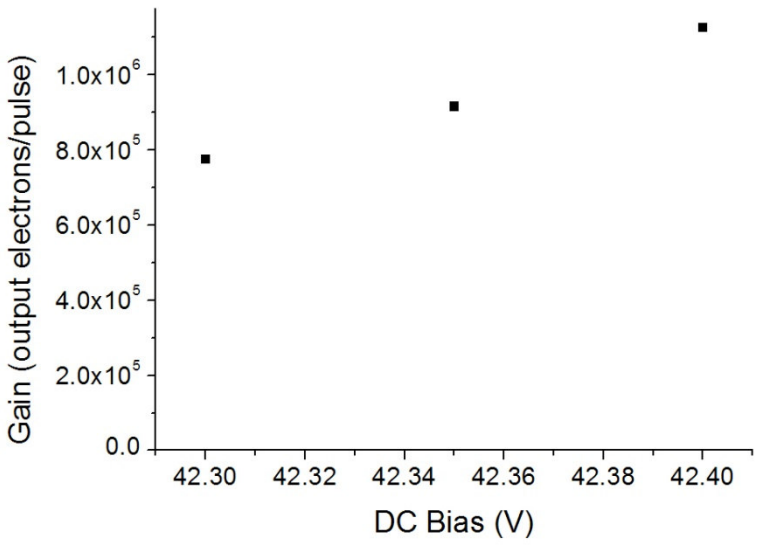

Figure 5.10. Gain vs. DC bias voltage for an InGaAs/InP SPAD operated in sub-Geiger mode at 270 K across an operational voltage range of 100 mV.

At each temperature an I-V characteristic was recorded so that an estimate of the operating voltage could be ascertained. Starting at the lower end of the range, a multi-photon pulse was directed at the SPAD and the output observed on the oscilloscope. The attenuation on the optical attenuator was then increased until no signal was seen on the oscilloscope. The voltage would then be increased slightly and the process repeated until a response was seen from an incident light level that was, on average, less than one photon per pulse. For an indication of the DC bias level used, an example IV characteristic with the middle operating point is shown in Figure 5.11. Measurements could then be recorded using the SPC-600 in 10 mV steps until the DCR became

prohibitively high for photon counting operation. At each DC voltage a histogram of photon-arrival times was recorded under dark conditions, followed by one with an attenuated laser pulse coincident in the timing window (50 ns). An example of these two traces can be seen in Figure 5.12.

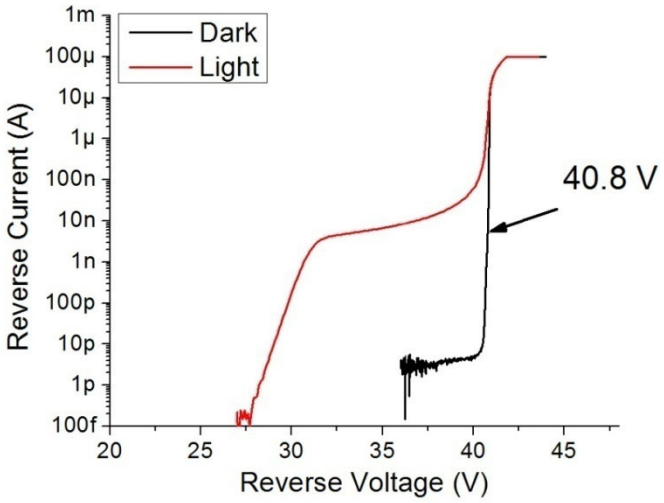

Figure 5.11. Example current-voltage characteristic of an InGaAs/InP SPAD at 250 K, showing dark current in black and photocurrent in red. The arrow addressing a point at 40.8 V signifies the mid-point of the range of DC-biases used to characterise the SPAD in sub-Geiger mode with a 10 kΩ resistor as R_S.

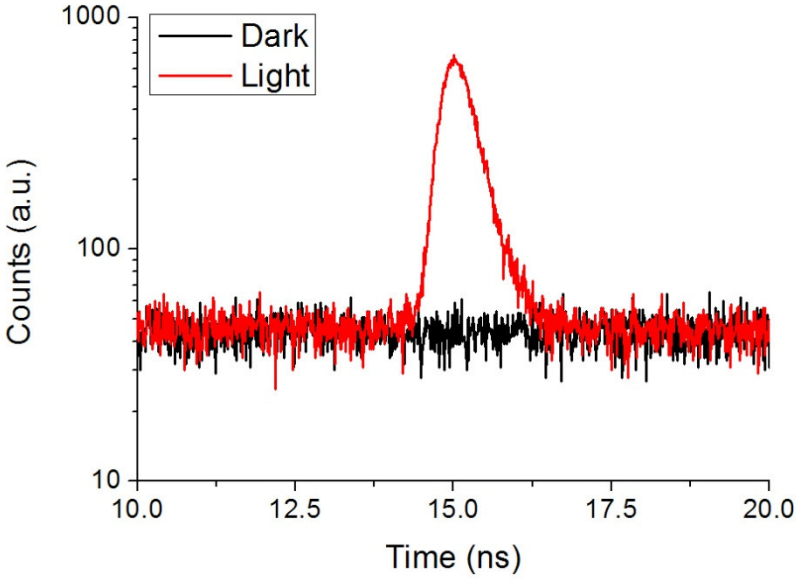

Figure 5.12. TCSPC histogram of an InGaAs/InP SPAD operated in sub-Geiger mode at 250 K, where R_S is 10 kΩ, showing the dark counts in black and the response to a heavily attenuated laser pulse in red.

Using the same methods set-out in Chapter 3, the SPDE, DCR and NEP of the SPAD could be calculated in sub-Geiger mode. The figures of merit were calculated at each discrete voltage and over a range of temperatures from 150 K to 290 K. We were also able to quantify the afterpulsing at each temperature as will be reported later in this Chapter.

5.3.2 Sub-Geiger Characterisation Results – SPDE, DCR & NEP

In Chapter 3, the figures of merit were reported as a function of reverse excess bias. For the sub-Geiger results, we quantified the DC bias by expressing it as a percentage of the breakdown voltage. The breakdown voltage was defined as the point at which the dark current reached 10 μA. The measurements span a DC bias that amounts to 99.5 % to 99.95 % of V_{BD}. This approach was adopted for a full characterisation of the device in sub-Geiger mode with as R_S of 10 kΩ. The results gained with the higher values of R_S will also be reported later as a comparison.

Firstly, the DCR is reported in Figure 5.13. Each temperature follows a similar gradient, apart from the 150 K measurements. At this low temperature, the overall number of counts recorded in a practical time period meant the measurements lacked statistical accuracy.

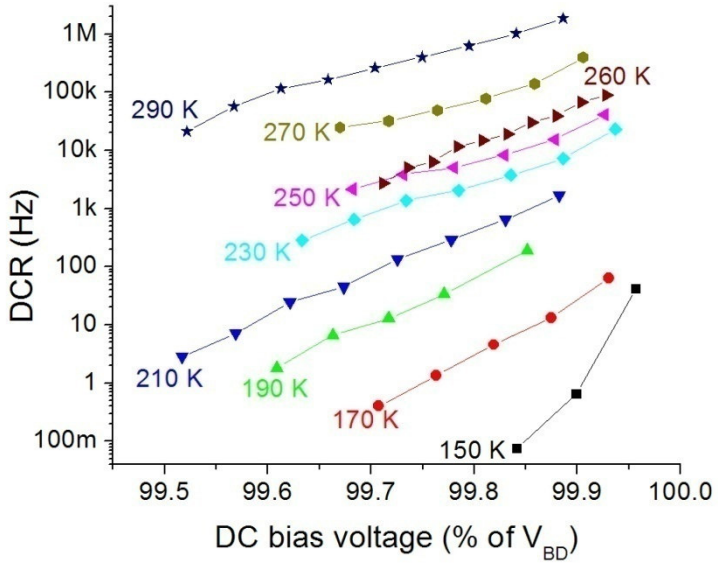

Figure 5.13. DCR of an InGaAs/InP SPAD operated in sub-Geiger mode at different temperatures plotted against DC bias as a percentage of the overall breakdown voltage (V_{BD}).

Already, a major advantage of working in sub-Geiger mode has been identified. The DCR is several orders of magnitude lower than the same device operated in Geiger mode. For example, at 250 K, the DCR in sub-Geiger mode spans a range from 2 kHz to 40 kHz. Referring to Chapter 3, Figure 3.17, the DCR in Geiger mode at 250 K spans the range 100 kHz to 650 kHz. However, it must be noted that these DCRs occur at much lower values of SPDE. The lower DCR did permit TCSPC operation at room temperature. To the best of the Author's knowledge, this is the first reported use of an InGaAs/InP SPAD in free-running mode at room temperature. The lower DCR can be attributed to the lower electric field within the device at sub-Geiger voltages as discussed later in this Chapter.

The SPDE as a function of bias is shown in Figure 5.14. Fewer temperatures are shown to aid clarity. At each temperature, the SPDE reached a maximum of about 1 %, apart from 230 K where 1.4 % was achieved. A major issue in measuring the SPDE was the time-correlated electrical noise present in the setup, which, if not discriminated properly, created an undulating background level as shown in Figure 5.15. Since the electrical output per event was so small, the noise could have an amplitude of 25 % of the actual output. Various tests were completed to find the most ideal discriminator level, and it was found that a level just above that of the maximum noise amplitude gave the best results.

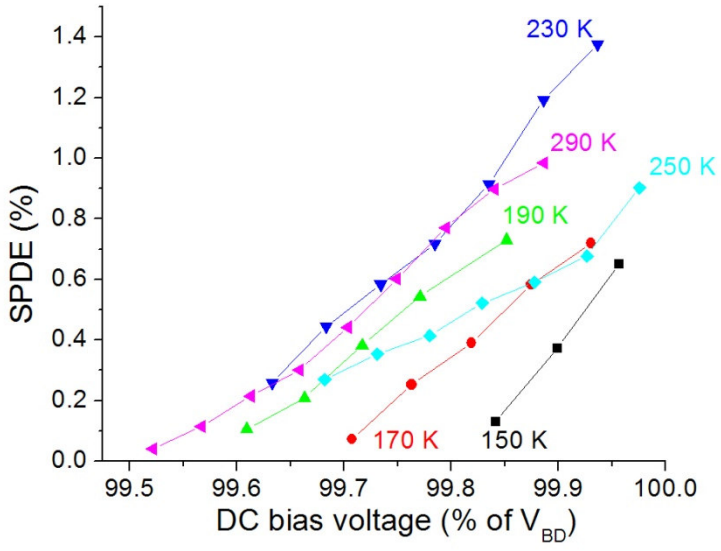

Figure 5.14. SPDE of an InGaAs/InP SPAD operated in sub-Geiger mode at different temperatures plotted against DC bias as a percentage of the overall breakdown voltage (V_{BD}) using an R_S of 10 kΩ.

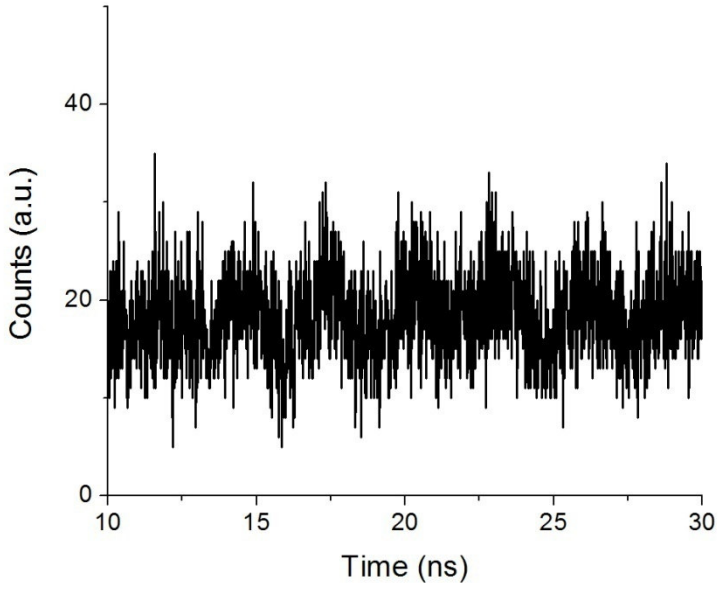

Figure 5.15. Electrical noise within the sub-Geiger output had to be carefully discriminated out. If a low voltage discriminator level was used, the time-correlated noise (possibly from radio-frequency pick-up), manifested itself in an undulating background level as shown in this MCA trace.

At temperatures below 150 K, the SPDE decreased dramatically. It is likely that this is due to the punch-through voltage and breakdown voltage being close together, hence the absorption region may not be as fully depleted at the voltages necessary for sub-Geiger operation compared to higher temperatures where the punch-through and breakdown voltages are further apart.

Although the SPDE is generally lower than in Geiger mode, the DCR is also much reduced. The only way to compare Geiger and sub-Geiger modes fully is to compare NEP and afterpulsing performance to determine which method is most sensitive and which is capable of a higher counting rate. In Figure 5.16 the NEP of sub-Geiger operation is reported at different temperatures in the same manner as DCR and SPDE. The performance is as expected – the overall NEP decreases as the temperature is lowered due to the reduction in DCR.

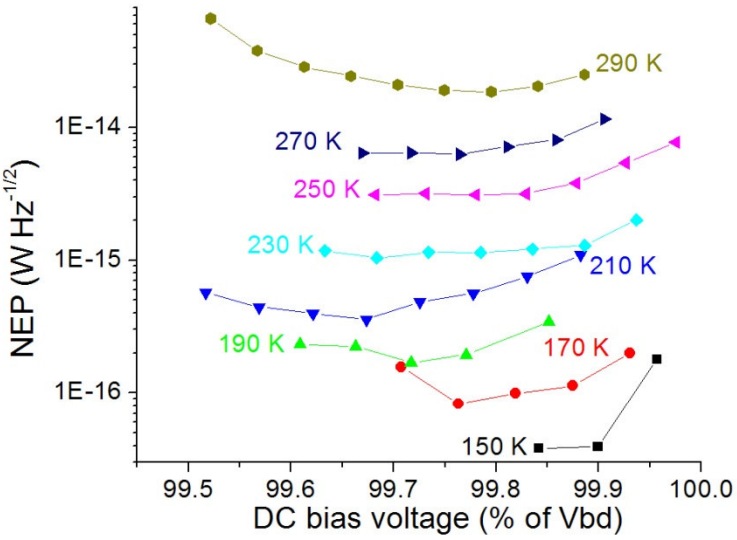

Figure 5.16. NEP of an InGaAs/InP SPAD operated in sub-Geiger mode at different temperatures plotted against DC bias as a percentage of the overall breakdown voltage (V_{BD}).

At each temperature there is a minimum NEP. These values were then compared with the minimum NEP achieved in Geiger mode from the results shown in Chapter 3. The comparison can be seen in Figure 5.17.

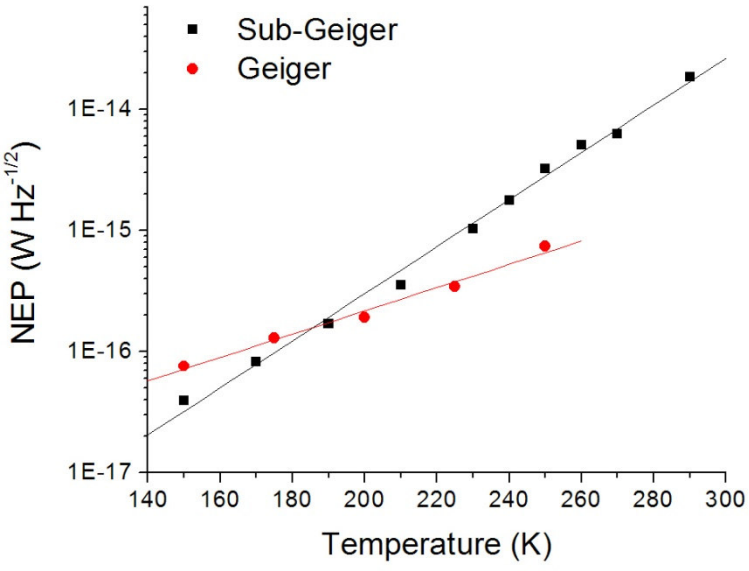

Figure 5.17. Lowest NEP of a Princeton Lightwave InGaAs/InP SPAD measured in Geiger mode (using 50 ns gate and shown in red) and sub-Geiger mode (ungated and shown in black) using an R_S of 10 kΩ.

At temperatures below 190 K, sub-Geiger mode operation results in a more sensitive device, despite the lower SPDE at all temperatures. This can be accounted for by the

significant difference in DCR between the two operating methods. Dark counts are caused by primary carriers generated within the InGaAs absorption region. This can be accomplished by numerous mechanisms. In [10] they are reported to be generation through defects (enhanced by high fields) and tunnelling (both direct tunnelling through defects and phonon-assisted tunnelling through defects). Since part of the contribution to the DCR is field-assisted, it is wise to assume that the lower the electric field within the InGaAs, then the lower the contribution to the DCR will be. In sub-Geiger mode the SPAD is biased slightly below breakdown, resulting in a lower field in the whole device (and hence the InGaAs absorber) which could explain the difference in DCR between the two operating methods. If we look at Figure 5.18, we see the dependence of calculated DCR on overbias according to [10]. Between 0 & 2 V overbias, the increase in DCR follows a trend greater than the exponential seen at higher bias levels. This could partially explain the large gap between the DCR in Geiger and sub-Geiger modes. During our characterisation steps in Geiger-mode, such a low voltage was not used, since most measurements started at about 5 % relative excess overbias. Another explanation for the higher DCR in Geiger-mode could be that of afterpulsing – without measuring the DCR at extremely low gate repetition rates, it is impossible to know if we are seeing a contribution to the phenomenon by the afterpulsing of dark counts alone, nevertheless, even if this is the case then the DCR measured at a given repetition rate represents the lower practical limit of the DCR at that repetition rate.

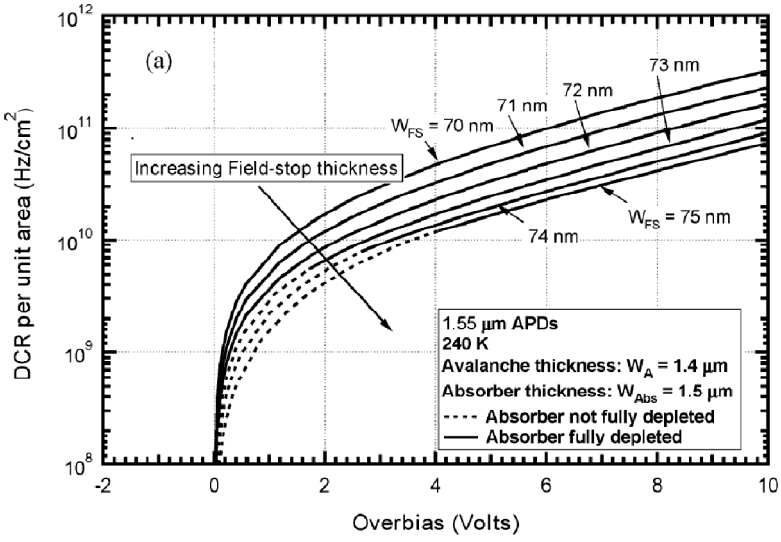

Figure 5.18. DCR dependence on overbias for an InGaAs/InP SPAD, showing a greater than exponential increase in DCR over the first 2 Volts, and a steady exponential increase thereafter [10].

Finally, the jitter was measured at all temperatures and the minimum was found to be ~ 800 ps. The average value it was ~ 1 ns throughout the temperature and voltage range. Increasing the bias did not appear to decrease the jitter in the same way that was observed in Geiger mode. The lower field throughout the device, although limiting the DCR in a beneficial way, limits the speed at which the carriers drift, hence contributing to the overall increased the overall jitter. It is important to note that ~ 1 ns timing jitter is comparable to the jitter presented by most InGaAs/InP SPADs at lower excess biases in Geiger-mode.

After full characterisation of the SPAD with an R_S of 10 kΩ, it was decided that an investigation into the effects of R_S would be conducted to examine device behaviour and will be detailed in the following section.

5.3.3 Sub-Geiger Characterisation Results – Varying R_S

Employing a 10 kΩ resistor as R_S was initially a precautionary step to protect the SPAD from damage due to over-biasing, since the resistor was sufficiently large to quench the avalanche if the SPAD was taken into a regime where a self-sustaining avalanche could occur. Using a low value of R_S should also result in a fast reset time due to the RC time constant increasing with higher values of R_S. However, there are advantages when using a higher value of R_S which leads to a trade-off between SPDE and maximum count rate since the reset time will depend on the R_SC product, where C is the sum of the device capacitance and the parasitic capacitance introduced by the addition of R_S (estimated to be ~ 3 - 4 pF in total), whereas an increased R_S can mean operation at higher reverse bias.

As with all analysis conducted within this Thesis on SPADs, the first characteristic studied was the I-V trace. Figure 5.19 shows the reverse current-voltage characteristic for an InGaAs/InP SPAD at 270 K using four different values of R_S as displayed. Only a 1.4 Volt range is displayed to demonstrate the I-V characteristic near avalanche breakdown.

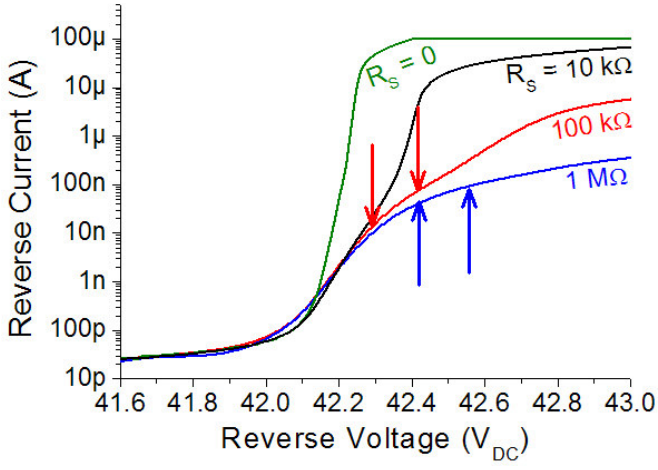

Figure 5.19. Reverse current-voltage characteristic of an InGaAs/InP SPAD at 270 K with four different values of R_S. As the value of R_S is increased, the current flowing through the device begins to tail-off near breakdown. The arrows signify the operating voltages used for the analysis of SPDE, DCR, NEP and jitter. The red arrows represent the minimum and maximum voltages used when R_S = 100 kΩ. The blue arrows represent the minimum and maximum operating voltages when R_S = 1 MΩ.

The effect of using a higher resistance for R_S on the operating voltage is shown in Figure 5.19. For example, with the 100 kΩ resistor, the operating voltages lie between the red arrows. When a 1 MΩ resistor was used as R_S, the SPAD could be biased with higher voltage before the DCR became prohibitively high for photon counting operation since some of the potential is dropped across R_S. Using a higher voltage results in a higher field within the device and hence a higher SPDE as shown in Figure 5.20. Since, at these values of R_S, the current does not necessarily reach 10 µA, the SPDE, DCR and NEP will be plotted as a function of DC bias.

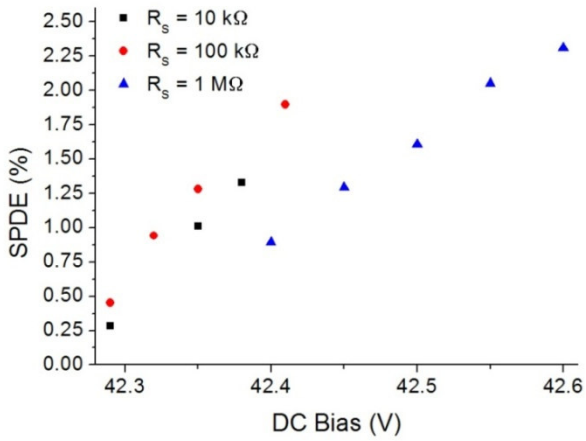

Figure 5.20. SPDE vs. DC bias of an InGaAs/InP SPAD operated in sub-Geiger mode at 270 K with three different values of R_S.

Figure 5.20 shows the one of possible advantages of using a higher value of R_S. For identical voltages, the SPDE when R_S = 100 kΩ instead of 10 kΩ increased by over 25 % mainly owing to the reduction in noise in the output signal meaning that a lower discriminator level could be used. When R_S was increased to 1 MΩ, although the SPDE at equivalent overall voltage was lower since the voltage across the diode was reduced, the capability of increasing the bias was realised. This enabled SPDE in excess of 2 % and as expected, the increase in SPDE with voltage is linear. Throughout the temperature range, the maximum SPDE when R_S = 100 kΩ was ~ 2.5 % and up to 3 % for R_S = 1 MΩ.

Comparing the DCR at 270 K, shown Figure 5.21, reveals that the DCR is reduced for a given DC bias with higher values of R_S for the same reason that the SPDE was reduced: proportionally more of the DC bias was dropped across the resistor rather than the diode.

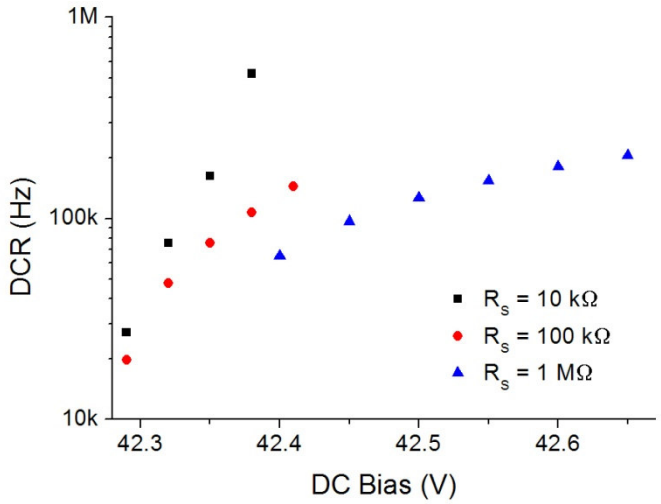

Figure 5.21. DCR vs. DC bias for an InGaAs SPAD operated in sub-Geiger mode at 270 K with three different values of R_S.

Appropriate selection of the resistor can lead to a combination of higher SPDEs and lower DCRs giving a reduced NEP, and hence improved sensitivity. The difference is shown in Figure 5.22. NEP values for R_S = 1 MΩ are not displayed since the points are coincident with those for R_S = 100 kΩ.

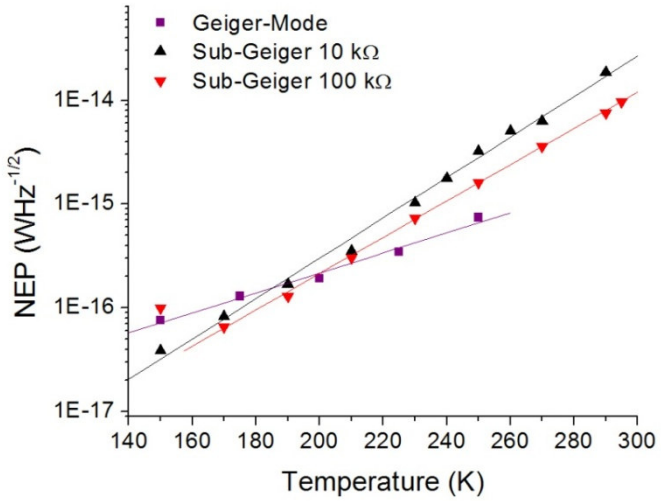

Figure 5.22. NEP vs. temperature for Geiger mode operation (purple points) and sub-Geiger for two different values of R_S (10 kΩ in black and 100 kΩ in red). At 150 K, the SPDE when R_S = 100 kΩ dropped dramatically causing the NEP to deteriorate.

It is interesting to note that the cross-over point between Geiger and sub-Geiger mode has now shifted to ~ 200 K.

Since it is possible to use higher DC voltages with larger values of R_S which results in a higher SPDE, it should also follow that a higher field will decrease the jitter observed. This is displayed in Figure 5.23 for MCA traces recorded at 270 K in terms of FWHM jitter. As expected, with increasing bias, the jitter decreases.

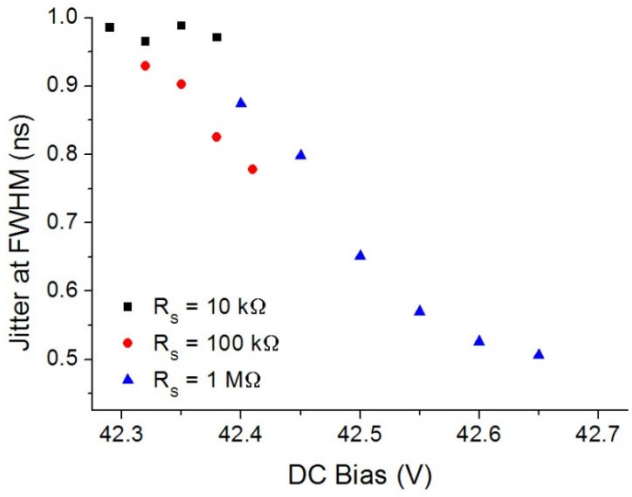

Figure 5.23. Jitter at FWHM recorded at 270 K of an InGaAs/InP SPAD operated in sub-Geiger with three different values of R_S. As the bias voltage is increased, the jitter decreases as expected.

From the results presented thus far, it would appear that there are many advantages of using a high value of R_S – higher SPDE, lower NEP, and lower jitter. However, the penalty is the maximum count rate that the detector is capable of achieving due to the recharging effect through the larger resistor. To investigate this effect, the photon-flux was increased and the count rate measured until a saturation point was reached and the count rate was maximised. The effect of R_S on the maximum count rate is shown in Figure 5.24 which utilised a 40 MHz driver to enable high count rates free of pulse pile-up effects. In both cases, the count rate increases to a saturation point then decreases due to the lower field across the device since there is insufficient time for the device to recover before the arrival of the next photon. When R_S = 100 kΩ the maximum count rate is ~ 4 Mc/s, however with R_S = 1 MΩ the count rate saturates at 400 kc/s.

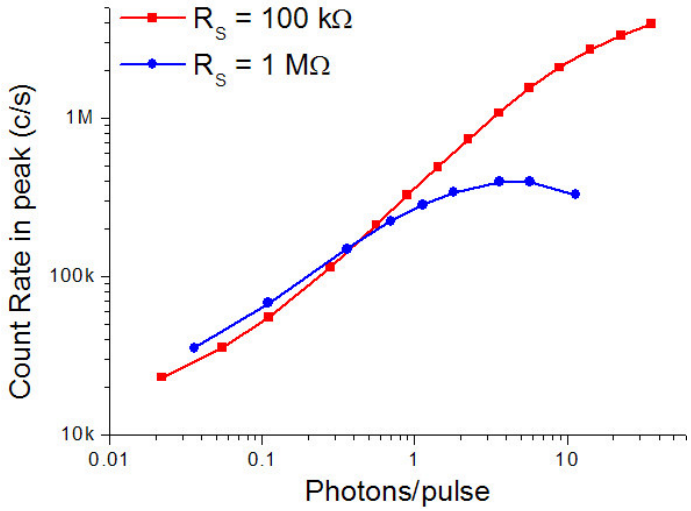

Figure 5.24. Photon counts per second vs. photons per pulse for an InGaAs/InP SPAD operated in sub-Geiger mode with two different values of R_S – 100 kΩ in red and 1 MΩ in blue at 270K. The decrease in count rate after the saturation (when R_S is 1 MΩ) point is caused by the lower field across the device since there is insufficient time for the device to recover before the arrival of the next photon.

As expected, with a larger R_S the maximum count rate is greatly affected. The count rate also has an effect on the measured FWHM jitter as demonstrated in Figure 5.25.

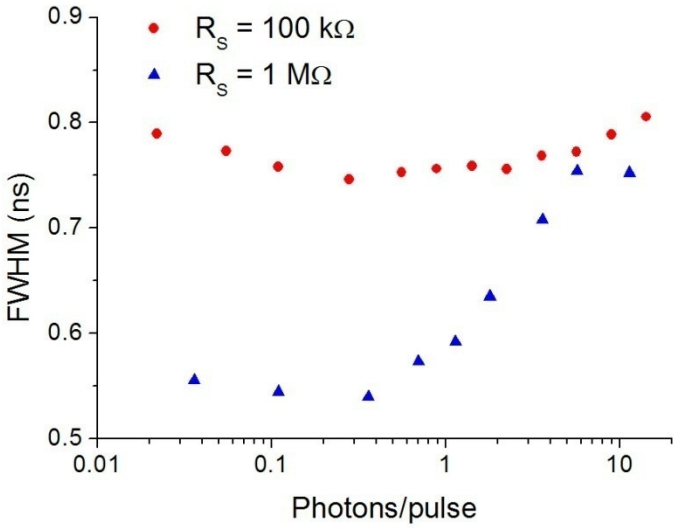

Figure 5.25. FWHM jitter vs. photons per pulse of an InGaAs/InP SPAD operated in sub-Geiger mode utilising two different values of R_S – 100 kΩ (shown in red) and 1 MΩ (blue) at 270 K.

Figure 5.25 shows a much stronger effect of photon flux on measured jitter when R_S = 1 MΩ compared to when R_S = 100 kΩ. This may be due to the recovery times involved with the larger resistor, if the device has not fully recovered before the next photon arrives, the field within the device will be lower, hence a higher jitter. In most applications, however, it is likely that the photon flux will be less than one photon per pulse, apart from perhaps in use as a single-photon counter in a TCSPC ranging of a highly reflective target.

As the count rate increases, the average current passing through the SPAD necessarily increases. Although the number of charge carriers per event is significantly lower than in Geiger mode, the fewer traps that are filled still contribute to afterpulsing. This is manifested in an increase in the DCR either side of the peak, i.e. a higher background count level. Therefore, it is also necessary to quantify this effect by calculating the DCR in the background to the side of the photon pulse signal from the laser. This is displayed in Figure 5.26 where the top three traces (filled symbols) show to the count rate in the peak relating to the left-hand y-axis and the bottom three traces (empty symbols) show the DCR measured at the associated count rate and relates to the right-hand y-axis. This is repeated at three different temperatures with an R_S of 100 kΩ.

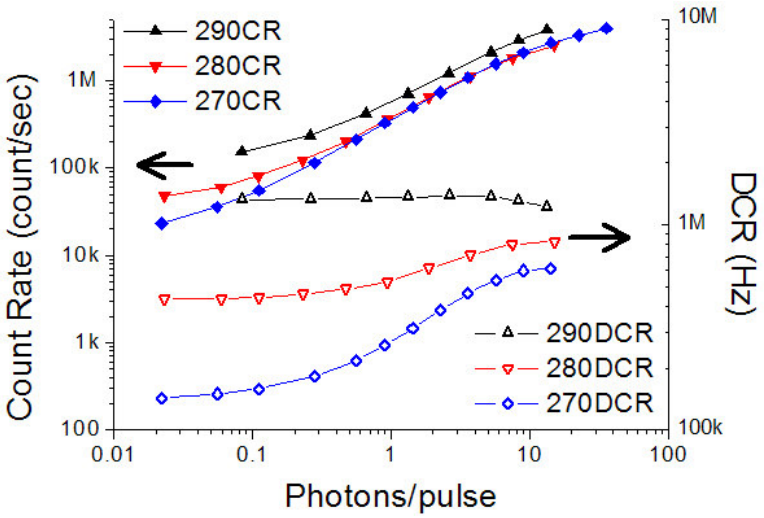

Figure 5.26. Count rate (filled symbols) and DCR (open symbols) vs. photons per pulse of an InGaAs/InP SPAD operated in sub-Geiger mode at three different temperatures with an R_S of 100 kΩ. The count rate is on the left-hand y-axis, and the DCR is on the right-hand y-axis.

In Figure 5.26, there are two effects on the DCR caused by the count rate. At 270 K and 280 K, the DCR increases until the count rate saturates, this is due to afterpulsing. The initial increase in DCR is more noticeable in the 270 K measurements compared to those at 280 K since the afterpulsing phenomenon is temperature dependent. At 290 K, there is almost no increase in the DCR, although it does decrease after the as the device nears its saturation count rate. As it approaches saturation, the device does not fully recover before the arrival of the next photon resulting in a lower field throughout the device, hence the DCR then decreases slightly. The effects of afterpulsing across the temperature range are studied in the following section.

5.3.4 Sub-Geiger Characterisation Results – Afterpulsing

Whilst NEP is one of the most important figures of merit for a single-photon detector, usually it does not take into account the effects of afterpulsing. Since in sub-Geiger mode the device is constantly DC-biased, it was not possible to perform the afterpulsing analysis using the TCCCM. Instead, the effect on the DCR was observed as the overall count rate was increased. This was accomplished by firstly measuring the DCR of the SPAD at a certain temperature and DC voltage. The photon flux arriving at the detector was then varied, starting at a low flux and increasing in steps until saturation. Practically, this was accomplished by decreasing the optical attenuation in 5 dB steps. The total count rate in the peak was then calculated to give an estimate of the count rate at which the detector was operating. Next, the "effective DCR" was calculated – this is the background count rate either side of the peak (see Figure 5.27 for

example) – the effects of afterpulsing will cause this to increase as the count rate is increased as demonstrated in the multiple-trace graph in Figure 5.28 measured at 250 K. If afterpulsing were not present, the effective DCR would equal the SPAD DCR measured at the beginning. These measurements were all conducted with R_S = 10 kΩ unless stated otherwise.

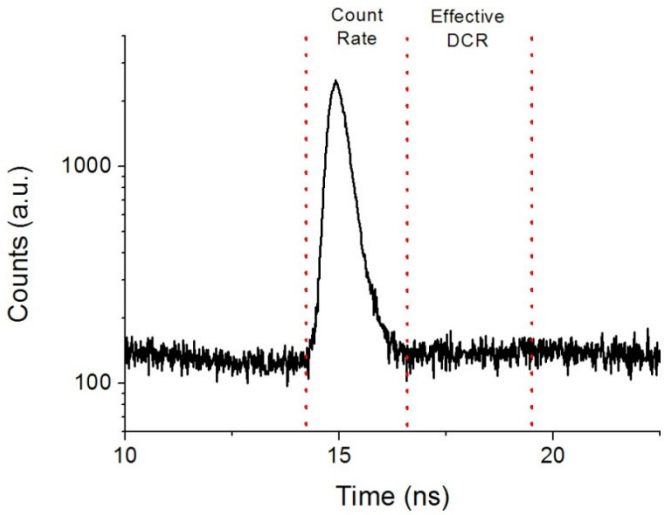

Figure 5.27. Photon-counting trace from an InGaAs/InP SPAD operated in sub-Geiger mode at 270 K. The count rate is calculated between the first two dotted red lines to give an estimate of the overall count rate. The "effective dark count rate" is based on the average count rate between the 2nd and 3rd red lines.

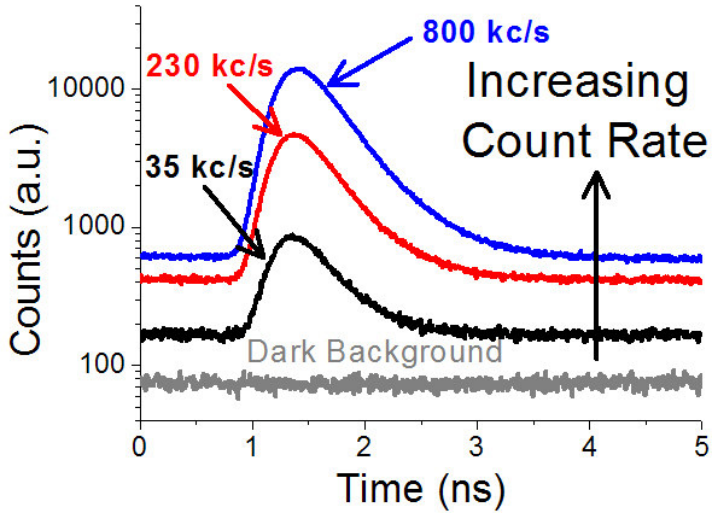

Figure 5.28. Multiple photon-counting traces of an InGaAs/InP SPAD operated in sub-Geiger mode at 250 K and the dark background count rate shown in gray. As the count rate increases, more charge flows through the device causing a higher "effective DCR" due to afterpulsing (in this case the value of R_S was 100 kΩ).

This method was used at each temperature to determine the effects of the afterpulsing phenomenon on sub-Geiger operation.

In Figure 5.29, the effective DCR is presented as a function of the overall count-rate in the peak. At 210 K the effective DCR increases from 1.4 kHz at ~ 9.4 kc/s to 13 kHz at 120 kc/s. At 270 K, the effective DCR increases from 60 kHz to 170 kHz over the same range. Quantitatively, the afterpulsing at 210 K increases by over twice as much at the lower temperature compared to that at 270 K. Qualitatively, it is clear that the gradient of the effective DCR with respect to count rate decreases as the temperature increases (more evident at high count rates), suggesting that the afterpulsing phenomenon decreases in severity as the temperature is increased as in the case of Geiger-mode operation shown earlier on in this Thesis.

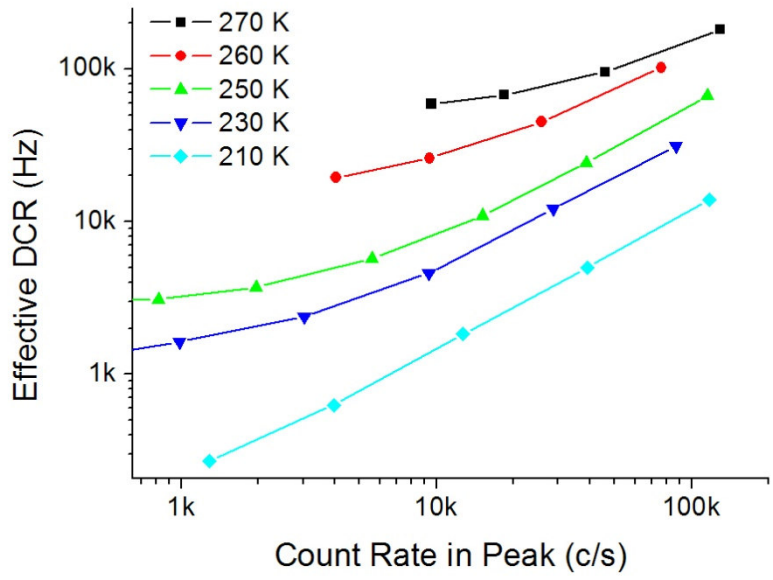

Figure 5.29. Effective DCR as a function of overall count rate of an InGaAs/InP SPAD operated in sub-Geiger mode at 5 different temperatures.

The most interesting result was achieved when the same experiment was conducted at 290 K. The trace for this temperature can be seen in Figure 5.30. It is clear from the background counts either side of the peak that there are no discernable effects of afterpulsing, even at a count rate of over 1 Mc/s shown in black in Figure 5.30.

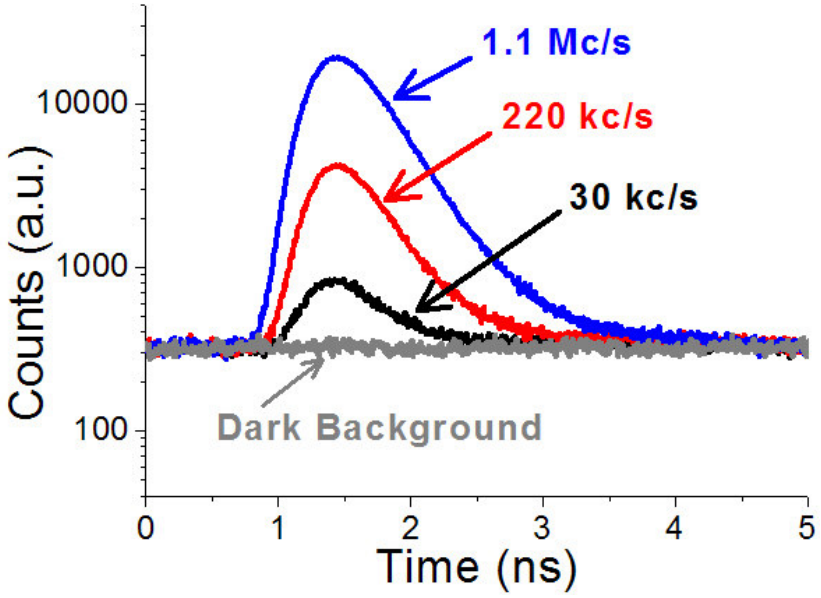

Figure 5.30. Multiple photon counting traces of an InGaAs/InP SPAD operated in sub-Geiger mode at various photon fluxes at 290 K with the dark background shown in gray and displayed on the same scale as Figure 5.28. As the count rate increases the effective dark count rate remains the same showing negligible signs of afterpulsing (in this case the value of R_S was 100 kΩ).

To complete the afterpulsing experiments, the same methodology was followed but at different DC biases to study the effect on the afterpulsing phenomenon. In Figure 5.31 the effective DCR is plotted against the count rate for 3 different DC biases. Naturally, the starting point for each voltage is different, since the higher the bias, the higher the DCR. It is interesting to note, though, that the increase in effective DCR with respect to count rate follows the same gradient at high count rates despite the difference in DC bias. This is to be expected, though, due to the very small fractional change in charge per event at the different voltages.

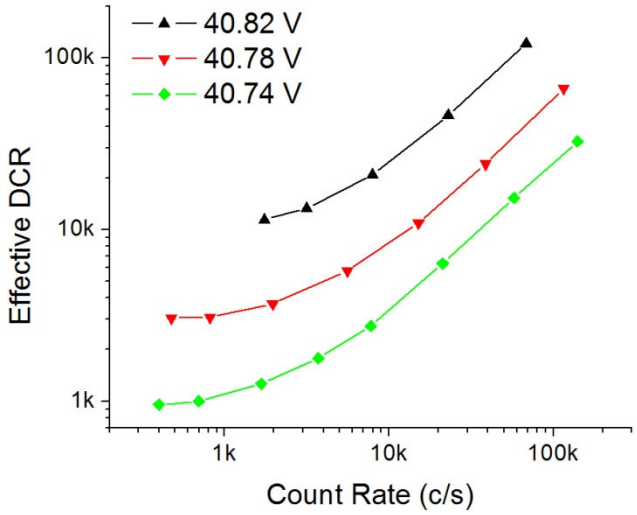

Figure 5.20. Effective DCR as a function of count rate of an InGaAs/InP SPAD operated in sub-Geiger at 250 K at different DC biases. Although the starting points are different due to differing DCRs, they all follow the same gradient at high count rates.

It is difficult to compare and contrast the afterpulsing phenomenon between Geiger and sub-Geiger modes due to the differing methods of characterisation. It is clear that the effects of afterpulsing are far less of an issue in sub-Geiger mode particularly at high temperatures, due to the reduced number of electrons required for the sensing/recording of an event.

5.4 Conclusions

Novel gating techniques such as sinusoidal gating and ultra-short gates have been reported by other research groups and their benefits are- reduced afterpulsing probabilities, good detection efficiency, low dark counts and low jitter. However, these methods, including the self-differencing technique, are mainly suited to QKD due to the periodic and repetitive nature of the gating process, where the gate-on period may ~ 500 ps or less. Also, many of these techniques involve sophisticated electronic circuits (some of which are capable of ~ GHz operation) and components with very sensitive delays in order to extract avalanche signals that would otherwise be hidden by the capacitive response of the SPAD.

Sub-Geiger operation with an InGaAs/InAlAs SPAD was reported recently by the authors of [7], along with the self-quenching and self-resetting process even though it

appears that the use of the term "sub-Geiger" may not be entirely correct. The avalanche dynamics and pulse size seem consistent with Geiger mode operation, although the feedback within the device causes the avalanche to be self-quenched and subsequently resets the detector to its quiescent state. Unfortunately at this time, no results were published in-terms of SPDE, DCR, NEP, jitter and afterpulsing.

A Princeton Lightwave Inc. InGaAs/InP SPAD was operated between 99.5 and 99.95 % of its breakdown voltage at temperatures between 150 and 290 K initially with an R_S of 10 kΩ. The DCR was found to be ~ 2 orders of magnitude lower than in Geiger mode, although it should be pointed out that this is not at equivalent values of SPDE. The reduced DCR was attributed to the lower field in the device, hence limiting the field-assisted tunnelling in the InGaAs which is one of the main causes of dark counts. The SPDE reached ~ 1 % at all temperatures, which is comparable to that of the SSPD used in Chapter 6 operating at 4 K at λ = 1550 nm. The NEP at temperatures less than 190 K was lower than that of the same device operated in Geiger mode, resulting in a more sensitive device, despite the lower SPDE.

An investigation into varying R_S was performed. With a larger R_S it was found that the electrical noise within the ouput signal was reduced enabling the use of a lower discriminator value. Using a 100 kΩ resistor as R_S yielded SPDEs 25 % higher than an R_S of 10 kΩ. The NEP was shown to improve with the increasing of R_S to 100 kΩ. When an R_S of 1 MΩ was employed, an SPDE of up to 3 % was achievable although the NEP was approximately the same as with a 100 kΩ resistor. Since it was possible to use a higher DC voltage through a higher R_S, the increased electric field lead to a decreased jitter at FWHM down to ~ 500 ps although this deteriorated with increasing count rate, possibly because the device had not fully recovered before the next event hence resulting in a lower field throughout the device. The penalty of using a higher value R_S results in a lower maximum count rate as the reset time depended on the R_SC time constant of the circuit - With an R_S of 100 kΩ, a maximum count rate of ~ 4 Mc/s, whereas only 400 kc/s was reached with an R_S of 1 MΩ.

It was found that the gain changed by about 30 % over a 100 mV voltage range. It was estimated that a voltage instability of ~ 20 mV would result in a small change (~ 6%) in the gain and the effect of this would be less noticeable on device performance due the use of a CFD since they are designed to cope with differing pulse heights. Temperature change of 0.1 K results in a shift in V_{BD} of ~ 20 mV and is therefore equivalent in effect to the voltage instability as mentioned previously. More experiments are currently

ongoing to determine the maximum deviation in both voltage and/or temperature before the performance of the device is severely degraded. It is worth noting, though, that some thermoelectric Peltier coolers have temperature stability of better than 0.1 K.

Finally the afterpulsing effects were studied in sub-Geiger mode by increasing the photon flux arriving at the SPAD. As the photon flux increased, the effective DCR also increased due to the afterpulsing phenomenon. As the temperature was increased, the relative change in effective DCR with respect to the count rate of the SPAD decreased, showing a lessening of the deleterious effects caused by afterpulsing. Finally, at 290 K it was shown that, for the first time, an InGaAs/InP SPAD was operated in sub-Geiger mode, un-gated free-running with negligible effects of afterpulsing present.

5.5 Acknowledgements

I would like to express my thanks to Mark Itzler for the InGaAs/InP SPAD which was used for the work within this Chapter and for his valuable advice and discussion on sub-Geiger operation.

5.6 References

[1] S. Cova, A. Tosi, A. Gulinatti, F. Zappa and M. Ghioni, *Avalanche Diodes and Circuits for Infrared Photon Counting and Timing: Retrospect and Prospect*, IEEE LEOS Newsletter, Oct, 25 - 28 (2006)

[2] M. Liu, C. Hu, J.C. Campbell, Z. Pan, and M.M. Tashima, *Reduce Afterpulsing of Single Photon Avalanche Diodes Using Passive Quenching with Active Reset*, IEEE Journal of Quantum Electronics, **44** (5), 430 - 434 (2008)

[3] P.L. Voss, K.G. Köprülü, S-K. Choi, S. Dugan, P. Kumar, *14 MHz rate photon counting with room temperature InGaAs/InP avalanche photodiodes*, Journal of Modern Optics, **51** (9), 1369 - 1379 (2004)

[4] N. Namekata, S. Sasamori, and S. Inoue, *800 MHz Single-photon detection at 1550-nm using an InGaAs/InP avalanche photodiode operated with a sine wave gating*, Optics Express, **14** (21), 10043 - 10049 (2006).

[5] Z.L. Yuan, B.E. Kardynal, A.W. Sharpe, and A.J. Shields, *High speed single photon detection in the infrared*, Applied Physics Letters, **91**, 041114 (2007)

[6] R.G.W. Brown, and M. Daniels, *Characterization of silicon avalanche photodiodes for photon correlation measurements. 3: Sub-Geiger operation*, Applied Optics, **28** (21), 4616 - 4621 (1989)

[7] K. Zhao, A. Zhang, Y. Lo, and W. Farr, *InGaAs single photon avalanche detector with ultralow excess noise*, Applied Physics Letter, **91**, 081107 (2007)

[8] M.A. Krainak, *Photoionization of Trapped Carriers in Avalanche Photodiodes to Reduce Afterpulsing During Geiger-Mode Photon Counting*, Conference on Lasers & Electro-Optics, (2005)

[9] S. Pellegrini, R.E. Warburton, L.J.J. Tan, J.S. Ng, A.B. Krysa, K. Groom, J.P.R. David, S. Cova, M.J. Robertson, and G.S. Buller, *Design and Performance of an InGaAs–InP Single-Photon Avalanche Diode Detector*, IEEE Journal of Quantum Electronics, **42** (4), 397 - 403 (2006)

[10] S. Verghese, J.P. Donnelly, E.K. Duerr, K.A. McIntosh, D.C. Chapman, C.J. Vineis, G.M. Smith, J.E. Funk, K.E. Jensen, P.I. Hopman, D.C. Shaver, B.F. Aull, J.C. Aversa, J.P. Frechette, J.B. Glettler, Z.L. Liau, J.M. Mahan, L.J. Mahoney, K.M. Molvar, F.J. O'Donnell, D.C. Oakley, E.J. Ouellette, M.J. Renzi, and B.M. Tyrrell, *Arrays of InP-based Avalanche Photodiodes for Photon Counting*, IEEE Journal of selected topics in Quantum Electronics, **13** (4), 870 - 886 (2007)

Chapter 6 - Time-of-Flight Ranging with SPADs and a NbN SSPD

6.1 Introduction to Laser Ranging Systems

Radar (Radio detection and ranging) has been in use since the 1930's and has proved invaluable to many groups including military, sea & air travel, and weather-forecasting. However, for high resolution distance measurements or measurements on isolated objects, radio and ultrasonic wave systems cannot be used since the waves cannot adequately be focussed. LIDAR (Light Detection and Ranging) or LADAR (Laser Detection and Ranging), however, provides a similar technique using light (visible and infrared) capable of high-resolution distance measurements and is now a well-established technique for both distance metrology and remote sensing. A number of optical methods have been developed to measure distance based on triangulation, interferometry or time-of-flight [1] [2].

Laser ranging systems are used in many applications: from military reconnaissance, to handheld "measuring tapes" for builders and surveyors. To avoid costly errors in manufacturing environments and to maintain highly uniform components, it is often necessary to rapidly obtain three-dimensional depth profiles for the characterisation of small volume batches. Most systems [3] rely on physical contact through the use of co-ordinate measuring machines (CMM). This method is both time consuming and operator intensive since a single probe is used to take many readings - again, LIDAR can be used in this situation as a non-contact and non-invasive way of analysing parts.

Lidar can be divided into four subsections: amplitude modulation & frequency modulation (both interferometry techniques), active triangulation and time-of-flight. There will now follow a brief review of these ranging methods.

6.1.1 Amplitude Modulation

Amplitude modulation (AM) correlates the phase shift between the transmitted and received signal of amplitude modulated light beams. The intensity of the laser beam directed towards a target is amplitude modulated, normally by varying the drive current of the laser [4]. The optical receiver measures the difference in the phase between the transmitted and received laser signals. The simplest case is that when the transmitted signal is modulated by a sinusoidal wave, with an associated amplitude and angular frequency. The received signal has a phase difference and amplitude dependent upon the distance to the target and its reflectance as shown in Figure 6.1 (dashed line).

The transit time of the laser can be calculated from the phase difference between the two signals and the range can thus be determined [5].

Single-frequency (homodyne) AM LADARs have two main limitations. If the modulation frequency is increased (which potentially increases the measurement accuracy), the unambiguous range (L_u in Figure 6.1) decreases which may result in aliasing or incorrect detection of a return.

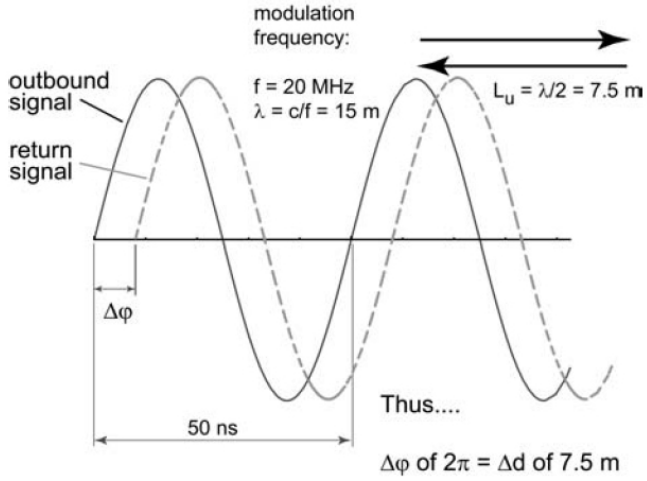

Figure 6.1. AM LADAR showing modulation frequency and associated unambiguous range, L_u of λ/2 or 7.5 m [6].

If the source is modulated as in Figure 6.1, then a phase shift Δφ, between the outgoing and incoming signal can be expressed in terms of the roundtrip distance:

$$\Delta\varphi = 2\pi fT = 2\pi f\frac{L}{c} \qquad \text{Equation 6.1}$$

where f is the modulation frequency, and c is the speed of light. The range, R, is half the total round-trip distance, L:

$$R = \frac{\Delta\varphi c}{4\pi f} \qquad \text{Equation 6.2}$$

To improve the accuracy and range, since L_u may be small due to the high frequencies used, the phase shift may be measured at an intermediate frequency using a heterodyne method that will maintain the phase shift and distance relationship. The accuracy can also be improved by averaging repetitive range measurements over a predefined acquisition time.

Performance of such transceiver systems has shown millimetre resolution in the 1 – 20 m range window with uncooperative targets. For cooperative targets (retro-reflecting corner-cubes) and high-frequency modulation, resolution has been reported in ~ 10's of μm [1]. For long distance measurements, a resolution of 15 m at a distance of 16 km in fog was reported in [7] using retro-reflectors.

6.1.2 Frequency Modulation

Frequency Modulation (FM) techniques are of particular interest due to the high dynamic range capabilities and high resolution affordable, particularly at short range. FM works by generating range dependent beat frequencies caused by mixing the return signal with a reference signal in order to measure range distances. In the case of a diode laser, the frequency is modulated directly [8], whereas with a gas laser an acousto-optic modulator is used [9]. Part of the transmitted laser beam is split from the incident beam, which is then mixed with the received signal. A beat frequency is produced upon detection which is equal to the optical frequency difference. The beat frequency is measured electronically and is used to calculate the range of the target. See Figure 6.2 for principle of FM lidar setup.

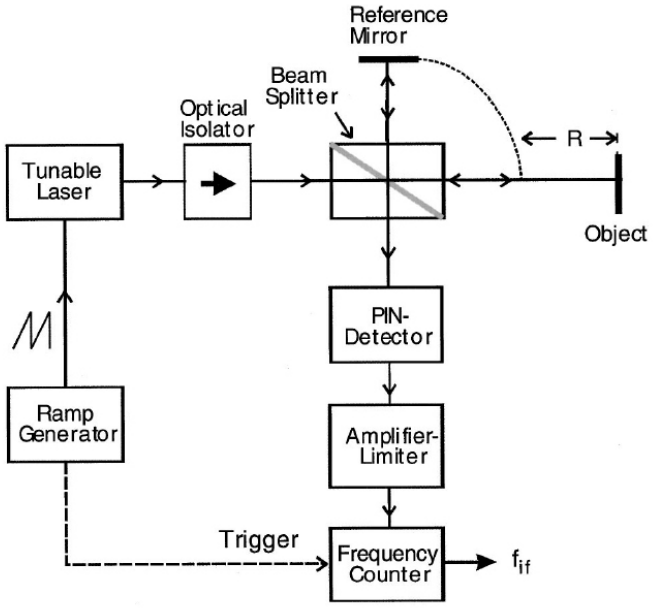

Figure 6.2. FM lidar principle setup employing a tuneable diode laser as the source [1].

In Figure 6.2, the laser has a saw-tooth bias current applied to its modulation section. The laser output goes through an optical isolator to stop reflections from affecting the laser frequency. The beam is then incident upon the reference mirror and object. The

reflections from both surfaces are combined in the detector. Since the detector measures power (square of amplitude), the AC component of the electrical output oscillates at the same frequency as the frequency difference between the two signals f_{if} as in Figure 6.3.

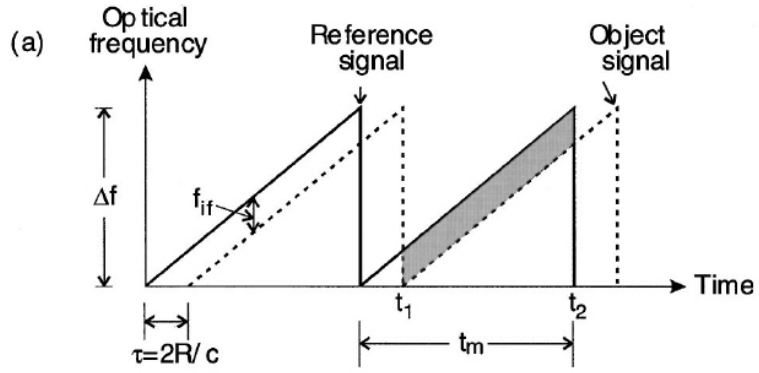

Figure 6.3. Reference & object signals from FM ladar in Figure 6.2. where t_m is the ramp period (typically 0.1 – 1 ms) [1].

f_{if} is measured with a frequency counter and related to the range "R" as follows:

$$f_{if} = \Delta f \tau / t_m = 2\,\Delta f R / c t_m \qquad \text{Equation 6.3}$$

Since t_m is in the order of 0.1 – 1 ms, no special high speed electronics are required despite a system capable of millimetre distance measurements.

Laser ranging is of great interest to defence organisations such as the U.S. Army Research Laboratory (ARL). W. Ruff *et al.* [10] reported that they had developed a number of ladars based on Frequency Modulation (FM) using Continuous Wave (CW) lasers. An avalanche photodiode (APD) was employed as the optical receiver along with a diode laser source. The technique used Radio Frequency (RF) chirping in order to modulate the intensity of the diode laser. The system collected high quality images under a variety of conditions.

The ARL also investigated a ladar system incorporating a 4-dimensional image of intensity and the three spatial co-ordinates. This method of defence laser radar is similar to that discussed by Augere *et al.* [11].

Coherent lidar has also been used to measure range and velocity [12], and this has been further enhanced by the use of optical frequency combs [13] capable of range resolutions down to 60 μm.

6.1.3 Active Triangulation

Active triangulation systems work by projecting a large spot or a line at some angle onto the object to be measured. The image of the projected spot or line is then viewed at some arbitrary angle and then imaged back to a detector [14]. Using a trigonometric relationship, the distance to the object can then be calculated since the position of the projected spot on the object and the spot on the sensor are related, see Figure 6.4. For a complete description of the theory of active triangulation and the derivations of the distance relationship between the projected spot on the object and the spot on the sensor, the reader should refer to [14] and [15].

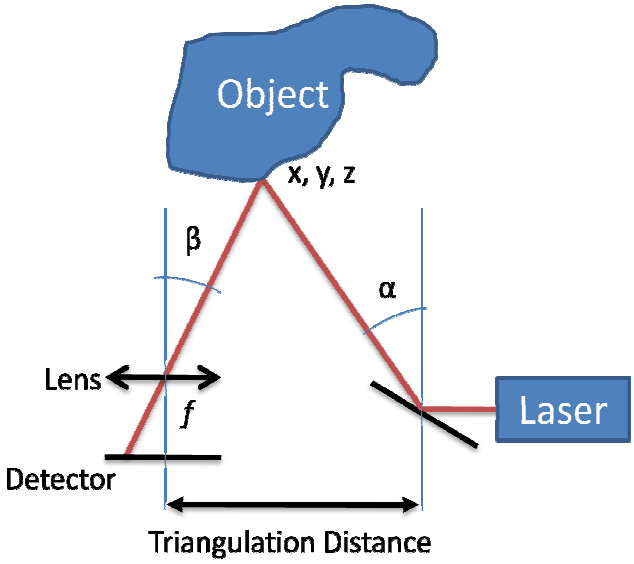

Figure 6.4. Laser triangulation, in this case with scanning to form depth profile of object after [16].

6.1.4 Time-of-Flight

Time-of-flight (TOF) laser radar is based on the transmission of a short pulse towards a target. The measured round trip distance of the transmitted and reflected laser beams determines the transit time and therefore the time-of-flight. The accuracy of range resolution is dependent upon the acquisition time used to collect the data, therefore increasing the integration time results in greater accuracy in the range resolution since each repetition is a measurement of the distance. This is particularly important for long distance applications. TOF ranging with a microchip laser and a single APD to measure the start & stop events has reported ± 0.5 mm over a range of 10 – 250 m by averaging 20 individual measurements, whereas single-shot performance showed an accuracy ~ ± 5 mm [17].

Commercially, companies like Canesta and SwissRanger sell short range (~ 10's of m) 2D/3D time of flight rangers/cameras based on CCD's with range accuracy in the region of 1 cm [18].

Other research efforts are working towards 2D imagers using SPADs and SPAD arrays. The European Framework Six project "Megaframe", for example, aims to make a 128 × 128 pixel imager based on TCSPC using CMOS SPADs capable of a million frames per second [19].

6.2 Time-Correlated Single-Photon Counting (TCSPC) Laser Ranging and Imaging

Although all of the ranging methods explained previously have been tested and have characteristics important to specific applications they mostly rely on high laser power especially for long distance applications. This raises the issues of eye-safety and covertness from unwanted detection. For these reasons, TOF ranging using single-photon detectors has become an increasingly appealing alternative due to its high sensitivity and capabilities of low average power operation. Work within Heriot-Watt University (HWU) in this field will be discussed in this chapter.

6.2.1 Research Efforts out-with HWU in TCSPC Laser Ranging and Imaging

Although the Photon Counting Group at Heriot-Watt University were one of the first groups to pioneer TCSPC laser ranging and imaging as explained in the next section, other research groups have adopted methods to exploit ranging and imaging with low light levels.

Researchers at Lincoln Laboratories (Massachusetts Institute of Technology) have been at the forefront of 3-dimensional imaging with photon-counting APD arrays [20]. The Authors of [21] demonstrated high-resolution (3 cm depth accuracy) 3-dimensional imaging ladar using a microchip laser and an array of Si SPADs (4×4) and its ability to gather high-resolution 3-dimensional images. For this example, a 532 nm laser pulsed at 1 kHz was used. The concept of operation is shown in Figure 6.5.

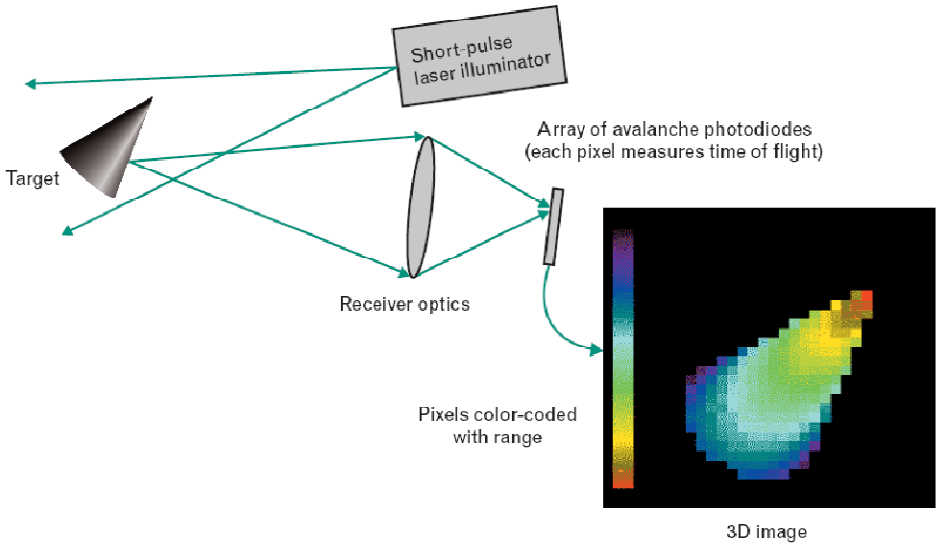

Figure 6.5. Concept of operation of three-dimensional ladar whereby a three-dimensional image is produced from a single laser pulse. A short pulse flood-illuminates the scene and the returns are collected by a two-dimensional array of APDs. The range of each point is calculated by the TOF method [22].

These systems record angle-angle-range data for each point enabling the data to be post-processed to observe the target from different rotations as shown in Figure 6.6 which reveals more information on the relative shapes, sizes, and positions of features on the van.

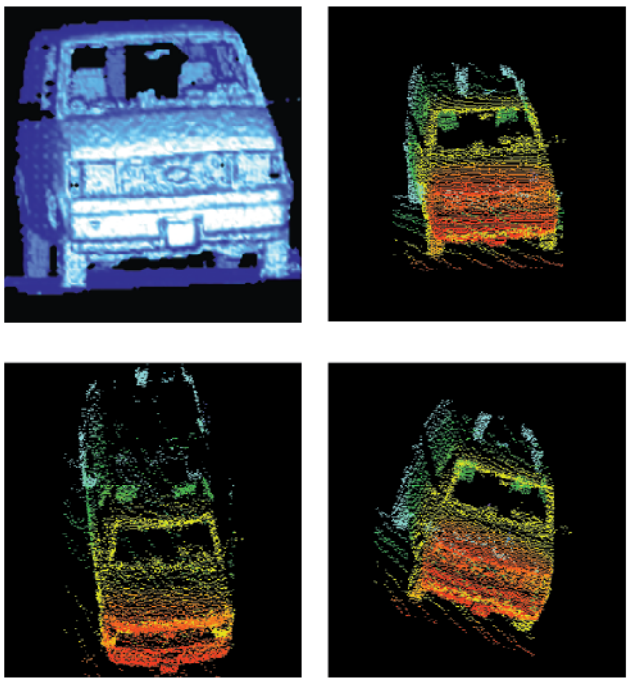

Figure 6.6. 128 x 128 pixel image of a Chevrolet van recorded from a distance of 60 m with the ladar looking at the front/right-hand side of the van. Top-left shows the three-dimensional rendered image and the other three are point clouds, computer-rotated to view the van from different angles [22].

TCSPC has also been used to construct three-dimensional images using and single-photon counting microchannel plates with crossed delay lines [23].

More recent work has seen the move towards eye-safe wavelengths (1550 nm) although only a few papers mention photon counting lidar at 1550 nm in the scientific literature [24] [25]. The Authors of [24] reported light signals scattered from clouds at a height of 2 km with a 1.54 μm photon counting lidar system. Verghese *et al.* report that their arrays of photon counting detectors could be employed in flash lidar but have not yet published any results on this work.

6.2.2 Previous Work at HWU on TCSPC Laser Ranging and Imaging

Since the mid 1990's, the Photon Counting Group at Heriot-Watt University has successfully demonstrated several novel techniques in laser ranging and imaging using TCSPC [26] [27] [28]. These techniques will be explained more fully in the following pages but include such features as using a constant reference peak within the photon counting histogram to alleviate time-walk issues, fast single-photon detectors in order to achieve ~ μm resolution, and specialised data-processing methods to extract small, or overlapping, return signals from multiple uncooperative targets.

A basic TCSPC setup for laser depth measurements is shown in Figure 6.5 below [28]. A pulsed laser is aimed at a target, each pulse is synchronised to provide a start signal for the Time to Amplitude Converter (TAC). The pulse passes through a beam splitter and encounters the reference surface (at a known distance) which only partially obscures the beam. The pulse then reaches the target where it is scattered. A fraction of the pulse will then return through the beam splitter and triggers the SPAD signalling the stop for the TAC. Since the repetition rate of the laser is ~ MHz, a probability histogram showing the time of photon arrival events can be quickly compiled (Figure 6.6), depending on the atmospheric conditions between source and target, and target reflectance.

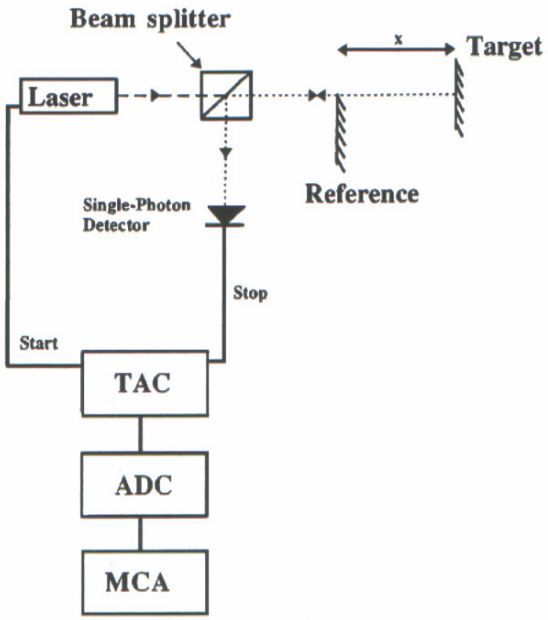

Figure 6.5. Basic TCSPC ranging setup where TAC is a time to amplitude converter, ADC is an analogue to digital converter, and MCA is a multi-channel analyser [28].

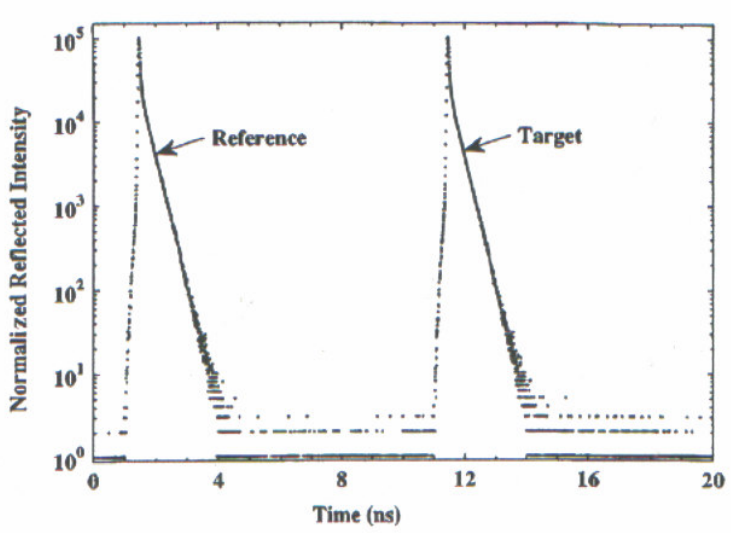

Figure 6.6. Histogram output from photon-counting card showing the reference and target peaks [28].

In Figure 6.6, the function of the reference peak is to minimise the effects of time-walk, as mentioned previously, caused by a drift in the timing electronics as components heat up/cool down. The reference peak enables the relative distance between it and the target to be calculated. Since the length of the reference arm is known, the total distance to the target can then be computed.

After this successful preliminary experiment, the setup was modified and one year later a similar method was used for depth imaging. This was accomplished by scanning the laser beam over an object and taking many depth measurements, in this way an image of the object can be built up and eventually a full 3D model can be made. Figure 6.7 demonstrates two examples of range images.

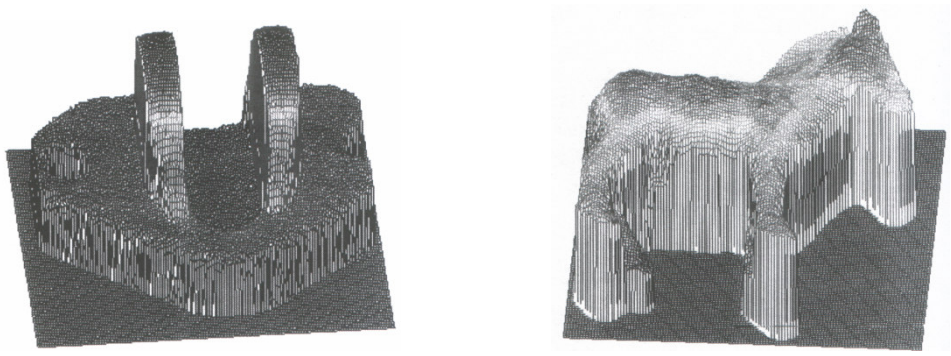

Figure 6.7. Range images of (a) metal lock and (b) a toy zebra [29].

In real life, these objects are a few cm in size. This precision depth measurement method can also be used for larger objects. In theory therefore, this system would be well-suited to profiling machine produced parts in factories to ensure quality control, from small parts as shown to large structures like aerospace components [28].

The work detailed herein is a continuation of this work, consisting of a multi-wavelength TOF ranging system using TCSPC.

6.3 Multi-Wavelength TOF Laser Ranging

Over the past 5 years, a multi-wavelength laser ranging system has been developed for detecting and analysing distributed targets. A distributed target is any object that has more than one surface, i.e. has a depth, like a bottle or box. If an object at long distance is targeted with a laser beam it is possible to receive laser returns from multiple surfaces. This is due to the divergence of the laser beam - in the multi-wavelength system for example, the beam diameter is about 20 cm at a distance of 330 m from the laser aperture.

6.3.1 System Setup

The system setup is shown in Figure 6.8.

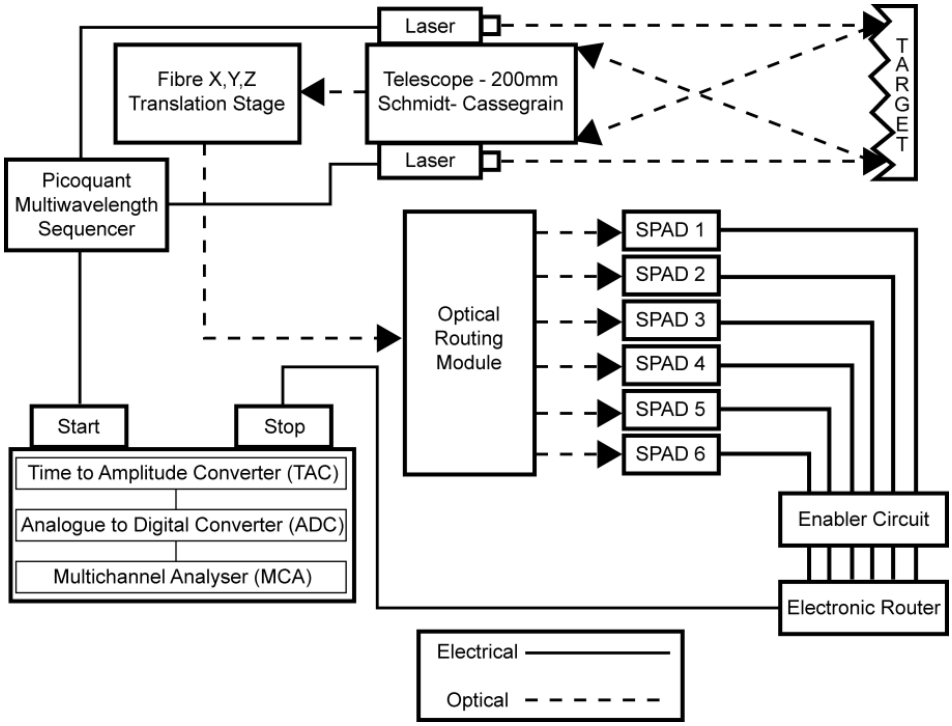

Figure 6.8. Multi-wavelength photon counting time of flight system schematic [30] built previously by colleagues but used by the Author for the measurements in Section 6.3.2.

The telescope is a standard Meade reflecting telescope with a 200 mm objective lens. It has been largely modified for the ranging project. Around the telescope's casing, a mounting ring was constructed for housing the lasers, evenly spaced, positioned at 12, 2, 4, 6, 8 and 10 O'clock. Each laser is aligned using three fine screws, one for each axis (x, y, and z) which allows precise adjustments to the beam's path. The six laser wavelengths used were: 630 nm, 686 nm, 780 nm, 845 nm, 911 nm and 975 nm which were chosen to have a good wavelength coverage within the operational range of silicon SPADs. Six discrete wavelengths were used to enable the recognition of a target from its spectral signature. Later in this chapter, use of this system with a 1550 nm pulsed laser and a NbN SSPD will be detailed.

The lasers were driven by a Picoquant multiwavelength sequencer. The repetition rate was usually set to 20 MHz - each laser fires independently, one after the other, such that each individual laser's repetition rate is 1/6 of that of the driver. The sequencer also has an output 'sync', an electrical pulse synchronised with the sequencer. The synchronisation pulse provides the trigger for the TAC representing the start signal (dependent on which photon-counting card was used). The TAC produces an output pulse proportional to the time difference between the start and stop events. The stop signal is provided by the SPAD as will be explained in due course.

A fibre is positioned at the image plane of the telescope to collect the scattered laser returns from the target. The fibre position can be optimised since it is adjustable in the same way as the lasers. When the telescope is being used for approximate alignment with the target, a 45º mirror can be placed in front of the fibre. This focuses the image on a small camera, sensitive in this spectral region, which is linked to a monitor so that the target can be viewed on-screen.

The collection fibre leads to the routing module. The telescope collects all forms of incoming light, all that we are interested in, however, is photons of the 6 wavelengths that were emitted. For this reason a routing module was designed (Figure 6.9)

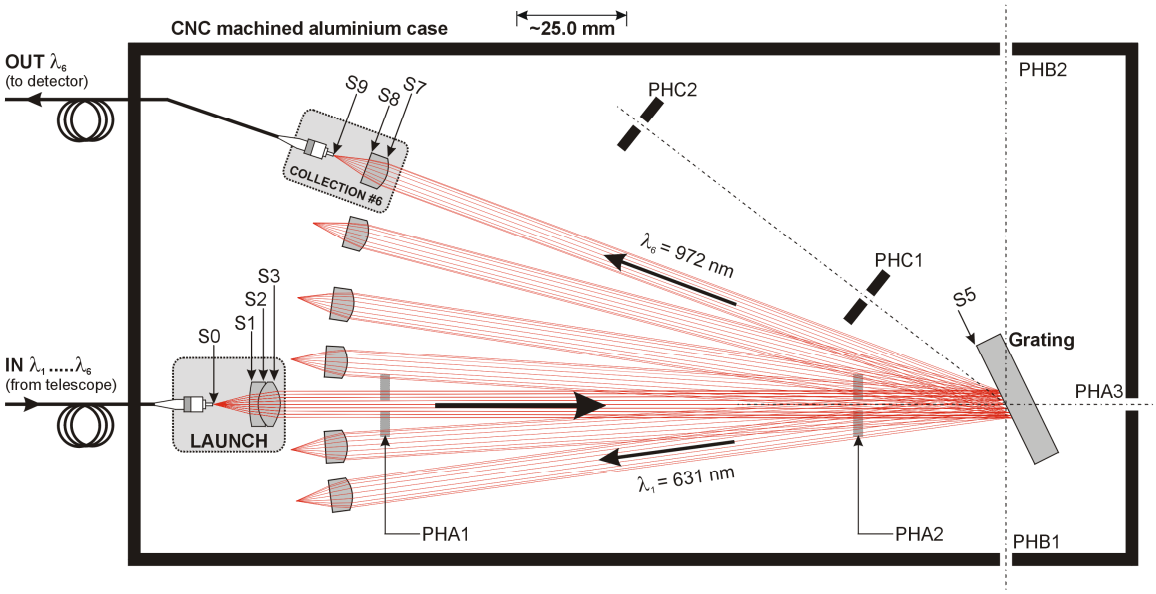

Figure 6.9. Optical routing module [30].

The incoming light from the fibre is incident upon a diffraction grating. Six lenses focus the separated wavelengths into fibres. An example of this is shown in the part named "collector #6" in Figure 6.9 above. Each output fibre is then connected to a SPAD. The photons detected by the SPAD provide the stop signal for the TAC. The signal from the TAC is digitised by the Analogue to Digital Converter (ADC). The Multichannel Analyser (MCA) makes it possible to view all 6 histograms on-screen at once. The TAC, ADC and MCA are all part of the Becker & Hickl SPC-600 card for any standard windows based PC.

6.3.2 System Operation with Improved Detector

The system's depth resolution (i.e. if we have two reflecting surfaces, what is the minimum resolvable separation) was tested using standard Perkin-Elmer SPADs. Shortly after, one of the SPADs was improved by Prof. Sergio Cova (Politecnico di

Milano). This modification involved the addition of a timing circuit although no modification was made to the original board. This new timing circuit facilitates the sensing of the avalanche rise current by extracting a short pulse with a fast rise-time through a pulse pickup linear network which is connected to the high voltage terminal of the detector. The improved output timing circuitry resulted in a faster device response (narrower FWHM) as well as jitter and peak-position being independent of count-rate, unlike the original Perkin-Elmer device [31] [32]. Figure 6.10 shows the response times of both SPADs.

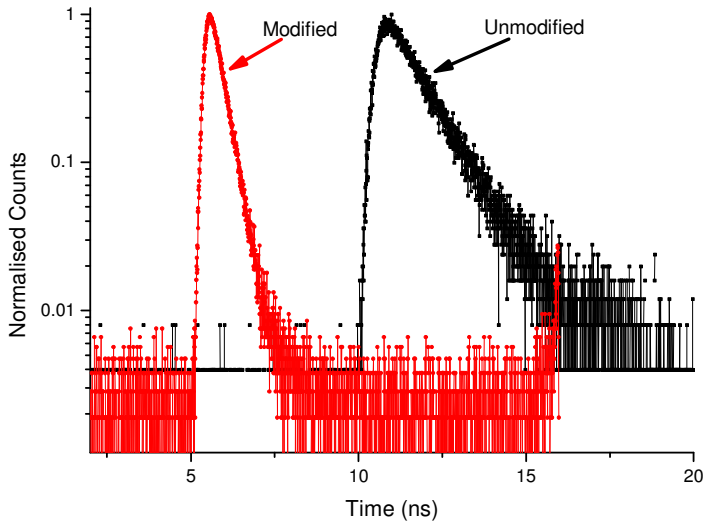

Figure 6.10. Time response of unmodified and modified SPADs

This has implications in any photon-counting area, and its effects on the ranging system will now be summarised.

6.3.2.1 Experimental procedure

To simulate two reflecting surfaces, two identical air-filled corner-cubes (retro-reflecting) were placed in kinematic mounts on an optical rail at a distance of 330 m from the transceiver equipment as shown in Figure 6.11. We were therefore able to vary the distance between 'surfaces', from a maximum of 70 cm to a minimum of 1.7 cm.

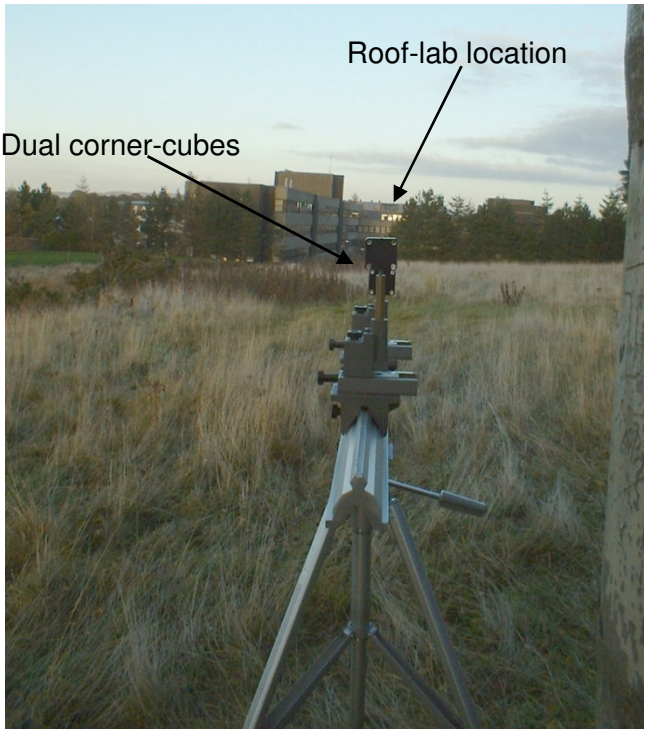

Figure 6.11. Photograph showing corner-cubes and location of roof-lab 330 m away.

At each separation a histogram was recorded for analysis using three different integration, or collection, times (1, 10 & 30 s) and with both SPADs (Unmodified & Modified) using only one wavelength (630 nm).

6.3.2.2 Results

The most time-intensive element of the ranging experiment is the data analysis. For the most part, a Mathcad program was used to calculate peak separations (written by Dr. Sara Pellegrini). It is a fairly simple approach which finds the centroids of the peaks within histogram and simply calculates the distance between them, hence giving the separation of the corner-cubes. The peak centroid is calculated using the following method. In Figure 6.12, if the area under the curve is normalised to unity, the peak shows the empirical probability that a single event will be measured at a specific value of x_i, i.e. the peak is a probability distribution for x_i. The mean is then defined as:

$$x_{mean} = \frac{\sum_i y_i x_i}{N} \qquad \text{Equation 6.4}$$

where y_i is the total number of counts in bin i. N is the total number of counts within the area of the peak:

$$N = \sum_i y_i \qquad \text{Equation 6.5}$$

The calculated mean is the centroid of the peak and represents the position of the peak on the x-axis.

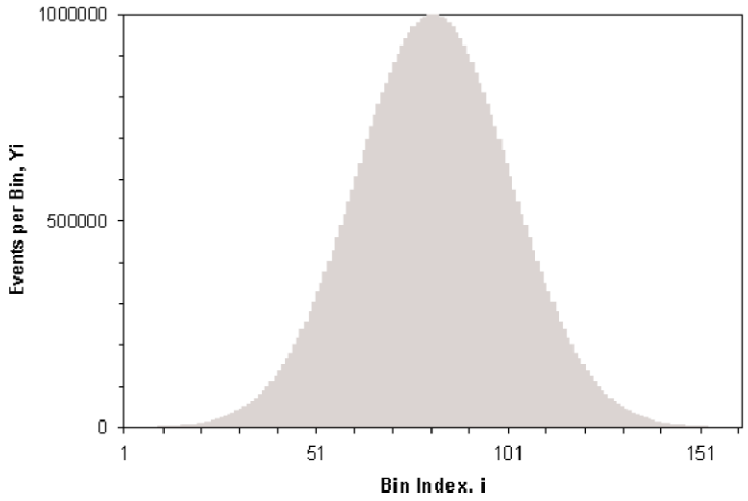

Figure 6.12. Gaussian curve shown in binned histogram data [33]

Another method using curve-fitting has been tested but this requires *a-priori* knowledge and is thus less suitable. We also work in conjunction with a group in the Electrical Engineering dept. who are working on computer algorithms with the aim of real-time result-processing. A complete explanation of the algorithms is out with the scope of this thesis although a brief summary follows. For peak separations that overlap, we used a previously developed algorithm based on reversible jump Markov chain Monte Carlo techniques (RJMCMC) [34]. This technique determines an estimate of the number of scattering surfaces, their positions, and the amplitudes of the returned signals from a distributed target. The RJMCMC approach is an extension of the basic MCMC algorithm designed to allow jumps between different solutions with different numbers of surface scatterers. Therefore, it is possible to consider the number of peaks as an unknown. In these experiments the only *a-priori* information that we include is the instrumental response of the detector. We initialized RJMCMC with ten uniformly distributed peaks to represent our lack of knowledge about the actual distribution of the target return. We are able to extract the positions and amplitudes of the returned signals from appropriate prior distributions as explained in [35]. A fuller description of this data analysis approach can be found in [36].

Firstly, a comparison of the signal to noise ratio (SNR) for both SPADs will be given as shown in Figure 6.13. The SNR is given by:

$$SNR = \frac{signal}{(signal + noise)^{\frac{1}{2}}} \qquad \text{Equation 6.6}$$

When the count rate becomes high and the noise becomes negligible we have:

$$SNR = \frac{signal}{(signal)^{\frac{1}{2}}} \qquad \text{Equation 6.7}$$

Or more simply:

$$SNR = (signal)^{\frac{1}{2}} \qquad \text{Equation 6.8}$$

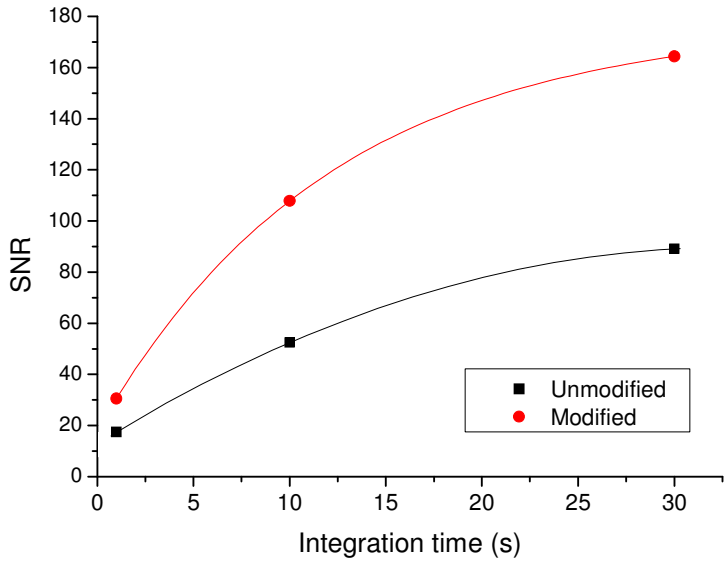

Figure 6.13. Comparison of SNR as a function of integration time for both SPADs.

The benefits of the modified SPAD are instantly apparent, the SNR of the modified SPAD is twice that of the unmodified. Since an integration time of 30 s gives the best SNR, the results presented will use this collection time. It should be noted that this is for ease of manual data-processing. A computational method like that described previously would be capable of far higher accuracy even from an integration time of 1s.

Figure 6.14 shows the separation calculated by the Mathcad program plotted as a function of the actual separation of the corner cubes. The black line shows the theoretical results (i.e. where the gradient is 1).

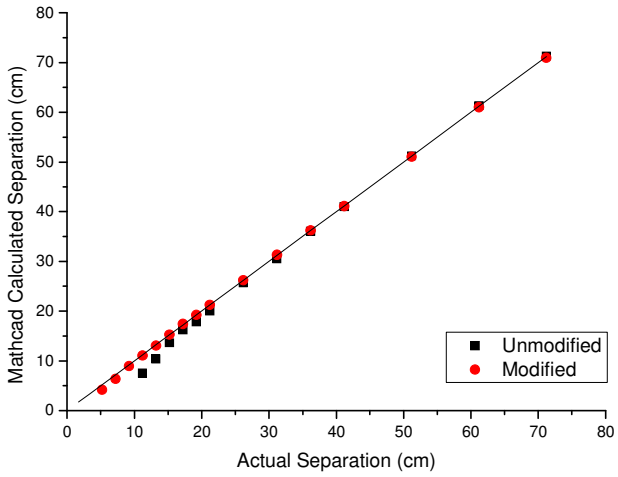

Figure 6.14. Calculated separation vs. actual separation for both SPADs

The accuracy of the unmodified SPAD decreases steadily as the corner-cube separation is reduced. In fact, it was not possible to identify two peaks in the histogram below 11.2 cm with the unmodified SPAD, whereas, the peaks were clearly separated even when the separation was as low as 5.2 cm when using the modified SPAD.

A typical return from the two corner-cubes can be seen in Figure 6.15 in which the separation is 70 cm. The higher SNR of the modified SPAD is clear along with its sharper response.

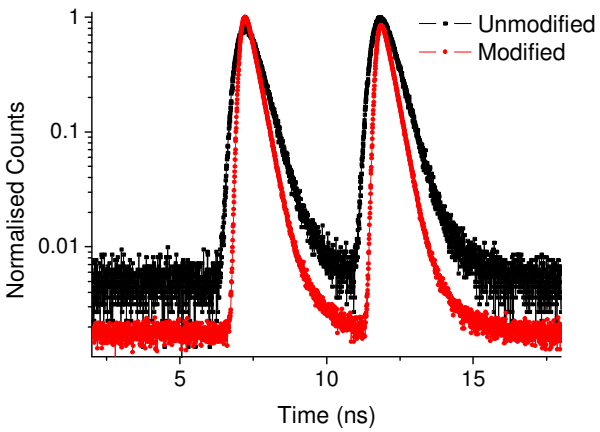

Figure 6.15. Corner-cube returns (70 cm separation) as seen within the TAC window of an SPC600 photon counting card for both SPADs.

As the separation of the corner-cubes is decreased, the peaks begin to merge. Clearly, if a SPAD with a faster response time is used the peaks will not merge as quickly as that with a slower SPAD. Figure 6.16 illustrates this point.

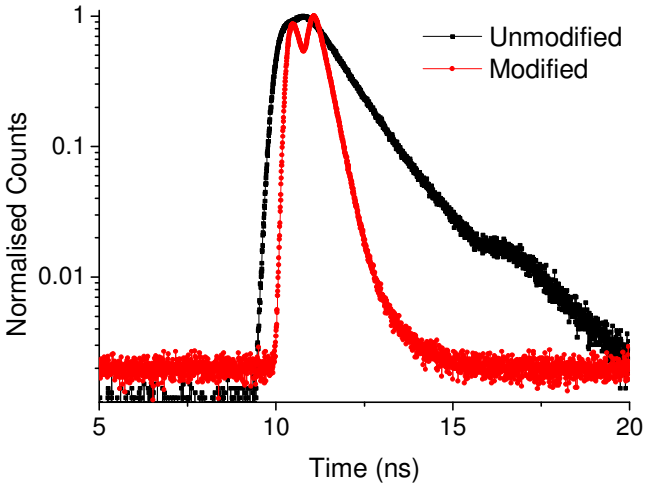

Figure 6.16. Corner-cube returns (9.2 cm separation) as seen within the TAC window of an SPC600 photon counting card for both SPADs.

If we look more closely at lower separations (Figure 6.17) the advantages of the modified SPAD are clear. The lower jitter and higher SNR result in a far higher accuracy of separation calculation and enable precise separation calculation to as low as about 5 cm with modest result-processing methods.

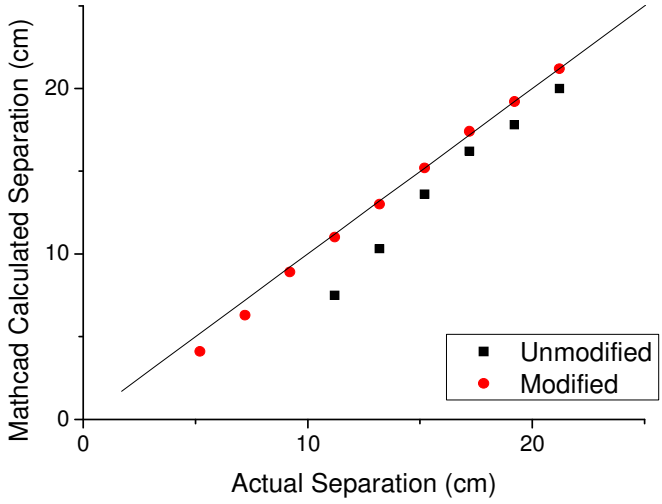

Figure 6.17. Calculated separation vs. actual separation for both SPADs.

As mentioned previously, we work in conjunction with a group from the Electrical Engineering dept. who have written algorithms to find peaks within the histogram that were explained earlier in this chapter. Figure 6.18 shows what can be achieved using these methods. The integration time used for these results is 1 second yet the accuracy is extremely high.

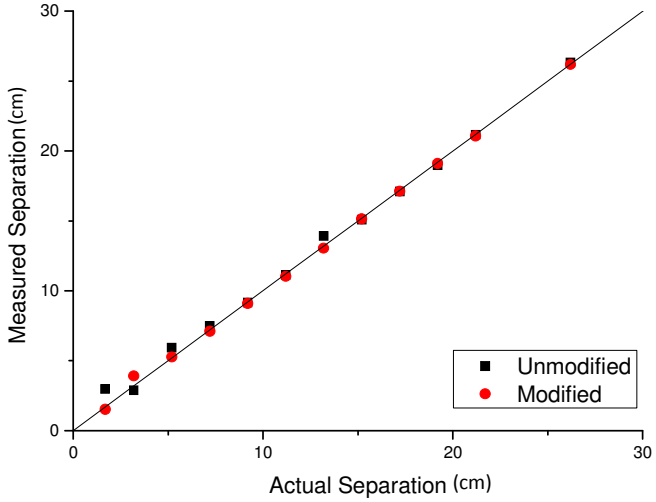

Figure 6.18. Calculated separation using dedicated computer algorithm on data acquired in 1 s vs. actual separation.

The main advantage of such a technique is that it uses peak-hunting and curve-fitting processes. This means that even when only one peak can be seen by eye, the program can find more peaks.

6.4 1550 nm Ranging with a NbN Superconducting Single-Photon Detector

The advantage of using a faster (narrower FWHM) detector has already been made apparent. For this reason, an experiment in collaboration with NIST (Boulder, Colorado, USA) was performed in order to take advantage of a fast superconducting single-photon detector (SSPD). Not only do these detectors have an extremely low jitter (~ 70 ps at FWHM), they are also sensitive in the infrared ($\lambda > 2000$ nm). This meant that we were able to conduct the same experiment as reported previously at 1550 nm instead of 636 nm.

The advantages of working at the longer wavelength of 1550 nm are numerous. Firstly, at 1550 nm, the solar background radiation is greatly reduced as in Figure 6.19 which results in a higher SNR leading to lower acquisition times. 1550 nm is also an eye-safe wavelength, but more importantly is more covert against unwanted detection making it more suited to military applications. Finally, since 1550 nm is an optical telecommunications wavelength, there is an abundance of lasers and filters that can be chosen to improve throughput of the system, with reduced background levels.

Unfortunately, at the time of writing this Thesis, no ranging at 1550 nm had been performed using InGaAs/InP SPADs. This was mainly due to the limitations on count rate and the need to electronically gate the detector limiting the useful window within which a range return could be observed. However, since sub-Geiger mode enables free-running operation, there are plans to implement its use in TOF ranging.

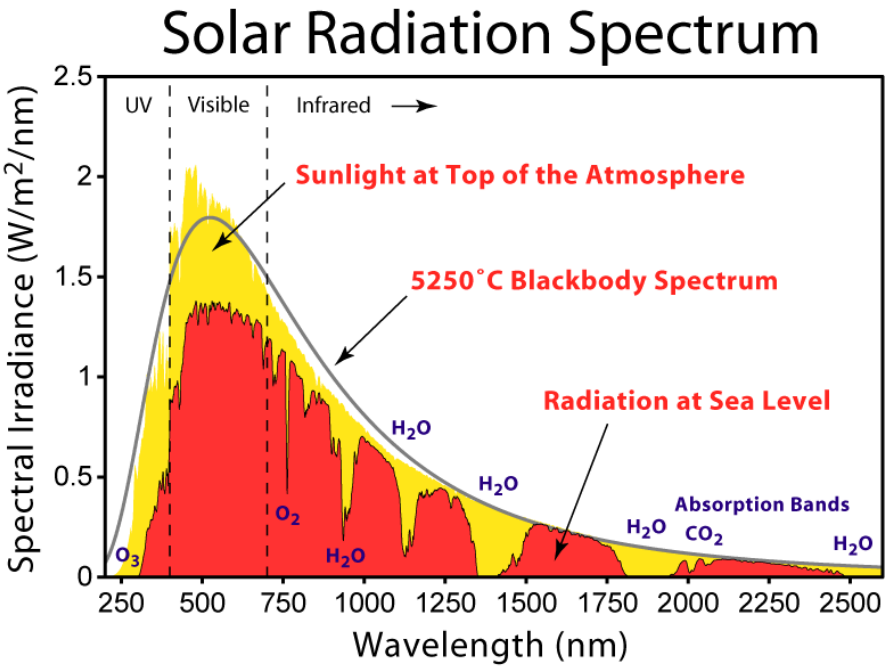

Figure 6.19. Solar radiation levels at top of atmosphere and at sea level showing absorption bands [37].

The system schematic is demonstrated in Figure 6.20. The transceiver comprises a standard 200 mm diameter aperture telescope, as previously shown in this chapter, with a 1550 nm wavelength pulsed laser diode (pulse duration FWHM < 50 ps). Instead of the optical routing module, an in-line bandpass interference filter (FWHM ~ 15 nm) centred at a wavelength of 1550 nm was used to reduce the background light at the detector since only 1 wavelength was in use. All the measurements were taken during ambient daylight conditions with an average laser power of ~ 5 μW [38]. A pulse-

pattern generator (operated at 40 MHz) was used to clock the laser driver and synchronise the signal for data acquisition. The pulse-pattern generator was chosen since its clock output was determined to have a higher stability than that of the Sepia driver used previously. This decreased the overall system jitter to about 70 ps at FWHM.

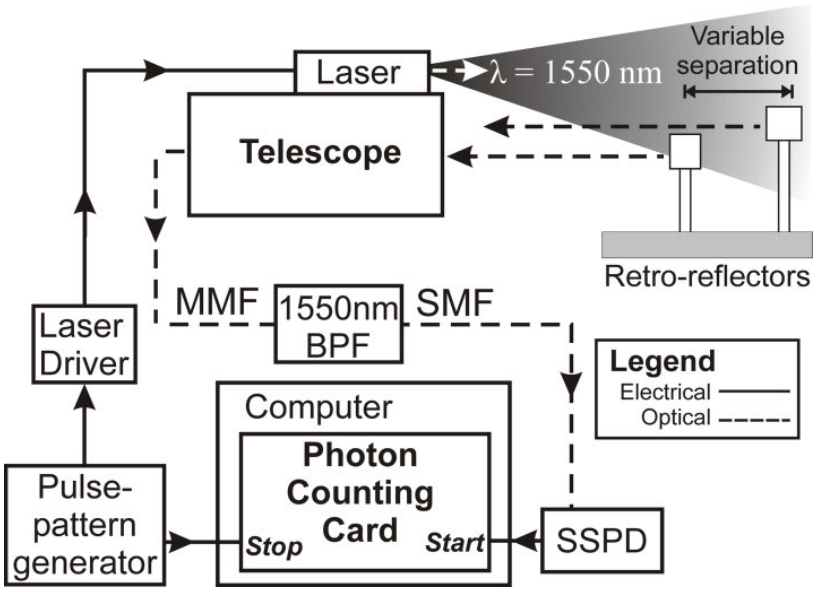

Figure 6.20. System schematic where MMF is multimode fibre, SMF is single mode fibre and BPF is an in-line band pass filter centred at 1550nm. The pulse pattern generator provides the synchronisation signal for the laser and provides a (delayed) electrical trigger signal to stop the timing sequence. A photon event returned from the target starts the timing sequence and the time difference between start and stop is recorded on a PC-based data acquisition card.

The SSPD is a 100 nm wide niobium nitride wire patterned in a meander line covering a 10 μm x 10 μm area [39], a full explanation of the operation of the detector can be found in Chapter 2. The SSPD is fibre-packaged and mounted in a closed-cycle Gifford-McMahon cryocooler [40] operating at a temperature of 3 K. The detector is mounted on a stage with passive temperature stabilisation and the fibre coupling is not affected by cryocooler vibrations. The detector is coupled via a single-mode telecommunications fibre (~ 9 μm core diameter to the rest of the optical ranging system. This type of detector offers several important advantages: single-photon sensitivity at infrared wavelengths (~1 % detection efficiency at λ ~ 1550 nm inclusive of fibre coupling losses), coupled with low timing jitter (<70 ps), short recovery time (< 10 ns) and low dark counts (<100 counts per second). The main contribution to the

background count level in the measurement is from ambient light, however, this is reduced by spectral, spatial and temporal filtering [30]. Operation at 1550 nm wavelength, allows these filtering techniques to be applied with much greater efficacy, as the solar background is much reduced at this wavelength, making the system considerably more robust against changes in the ambient light level.

The method used was identical to the short wavelength measurements where the optics of the laser diode were configured so that both corner cubes were illuminated at the range of 330 m, and the photon returns were collected by the telescope.

6.4.1 Results using NbN SSPD

The separation of the corner cubes was varied from 500 mm down to zero separation. Histograms of photon returns were recorded for 1, 10 and 30 seconds at each separation to investigate the effects of SNR on depth resolution accuracy. Examples of these histograms can be seen in Figure 6.21 where three different separations are displayed.

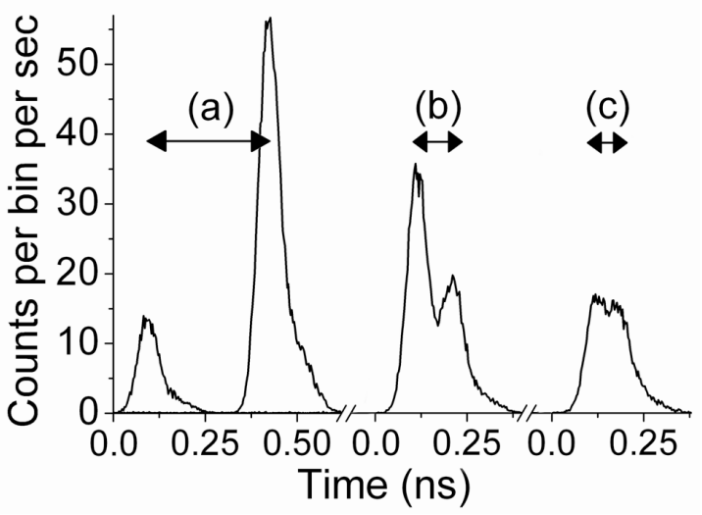

Figure 6.21. Three separate examples of the time responses of the system where the target consisted of two corner cube retro-reflectors separated by (a) 50 mm; (b), 15 mm; and (c) 10 mm. The acquisition time was 30 s in each case with a bin-width of 3.073 ps. The heights of each trace are slightly different due to variations in optical alignment between the three measurements.

Already, the advantage of the narrower FWHM system response is apparent. Referring back to Figure 6.16, it was difficult to extract the separation value using the centroid method from data representing a separation of 92 mm. With the SSPD, even a separation of 10 mm can be analysed using the centroid technique. An acquisition time

of 30 seconds was used in each case. In these examples, the 4096 channels, or bins, of the photon-counting card were divided over 12.5 ns, giving a bin-width of 3.073 ps. Photon returns were recorded at a rate of ~ 1000 per second (dependent on the optical alignment). The detector response has a Gaussian profile with a FWHM of 68 ps [40]. In Figure 6.21, the instrument response of each surface return is 70 ps FWHM. The slight shoulder on the right hand-side of each individual surface return is due to the asymmetric shape of the laser output pulse.

To analyse these results, the same methods were used as in the previous work - centroid and RJMCMC. Since these techniques have been described previously, the results are displayed in Figure 6.22.

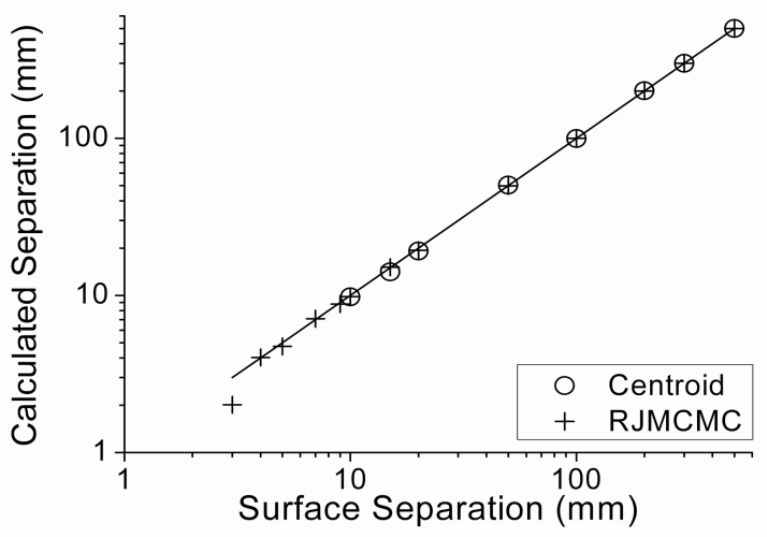

Figure 6.22. Calculated separation vs. surface separation. An acquisition time of 30 s was required for each data point. Photon returns were recorded at a rate of ~1000 per second. The black line represents the case of perfect agreement.

At large separations, both processes perform well. For surface separations of less than 10 mm the target returns were sufficiently close to render the centroid method wholly unreliable. However, it is clear that using the RJMCMC algorithms (with no *a priori* knowledge other than the instrument response function) enables a much lower separation to be resolved, 4 mm being the minimum reliably demonstrated with these measurements.

6.4.2 System Losses at 1550 nm wavelength

It should be noted that the system was not designed for use at 1550 nm. The coatings in the telescope are far from ideal for such long wavelengths. Below is an explanation of the output power of the laser and the losses involved.

The time-of-flight telescope ranging system was originally designed for operation with non-cooperative targets illuminated by lasers of wavelengths within the visible region. Subsequently, the losses at wavelengths of 1550 nm are greater than previously experienced. A guide of the losses involved can be summarised as follows.

The laser is mounted around the circumference of the telescope aperture and directed towards the retro-reflectors at a distance of 330 m. Due to the divergence of the laser beam, the actual beam size at this distance is in the region of 20 cm by 10 cm and oval in shape. The diameter of each retro-reflector is 1" (2.54 cm), hence the fraction of light captured by each retro-reflector is relatively small (a few percent).

The light reflected by the retro-reflectors then travels back along the axis of incidence. The divergence of the retro-reflectors is 1 mrad, hence the size of the reflected spot arriving back at the telescope mainly intercepts the laser itself, and the outer casing of the telescope. Only a minute fraction of the returning beam is actually collected by the telescope. We have previously measured the loss caused by the above factors which is in the order of 5×10^{-5}. Whilst this is a very low fraction, it must be re-iterated that the telescope system is not designed for retro-reflection, but scatter from non-cooperative targets. The telescope itself introduces a loss factor of around 0.1 since the optical coatings are designed to work at visible wavelengths with an efficiency of around 50 %. The losses for changing from multimode fibre at the telescope output to single mode fibre input to the SSPD are estimated to be ~ 0.01.

The band-pass filter is housed in a U-bracket with fibre connectors either side and micro lenses to collimate the input light from the fibre and re-focus the light into the output fibre. The losses caused by this process are estimated to cause a decrease in power by a factor of 0.3. Finally, the detection efficiency of the detector, inclusive of fibre coupling losses, is 1 %.

Multiplying these factors together we have a total loss, by which we must multiply the outgoing power, of 10^{-11}.

The outgoing power is ~ 5 μW, which is 1×10^6 photons per pulse or 4×10^{14} photons per second. The average rate of photons we detect per second is 1000 (not including dark/background counts). If we multiply the outgoing number of photons by the losses involved, we arrive at a rate of approximately 1000 photons s^{-1} as demonstrated in the measurements. Careful re-design of telescope and reflective optics could give 100-1000 factor improvement, resulting in nanowatt operation. What we can conclude from this is that 5 μW is clearly not a lower limit on the source power required for identification of surface separation and that on a non-cooperative targets with improved optics for this wavelength it may be possible to greatly reduce the outgoing power required.

6.5 Conclusions

In this Chapter a brief review has been given of various laser ranging techniques and systems for absolute distance measurement. Each system reviewed herein has its advantages whilst some have their own niche application, but where low powers are required, photon counting offers a unique opportunity to perform high accuracy depth/distance measurements with low light levels and fast acquisition times. This can also be extended for military applications where target identification is required. The multi-wavelength system offers high covertness against unwanted detection, information about the depth of a distributed (multiple reflections) target, and information on the spectral response thanks to the multi-wavelength operation.

With a commercial "off-the-shelf" SPAD, a reasonable surface-to-surface separation of just over 10 cm was resolvable using a simple centroid approach to find the distance between return peaks. After some modifications to its circuitry, a separation of 5.2 cm was resolvable with the same detector. With advanced RJMCMC algorithms the minimum resolvable separation was reduced to 1.7 cm.

The use of a faster (narrower FWHM) detector has been demonstrated and, in the case of the SSPD, shown to give a surface to surface depth resolution of 4 mm when using the RJMCMC analysis. Even with the centroid method, a separation of 10 mm was measured. Most of the jitter measured with the SSPD was the laser pulse width itself, there are plans to use a faster laser and hence the prospect for sub-millimetre depth resolution at considerable (> 300 m) stand-off distances. In terms of covertness of operation, the use of a 1550 nm laser decreased the likelihood of unwanted detection of the system, which is especially important for military applications. The solar

background levels at 1550 nm were also much reduced, lending itself to lower power operation. It has been demonstrated that although an average power of 5 μW was used herein, this is by no means the lower limit. Careful redesign of key optical components could result in nanowatt outgoing optical power levels.

Whilst many of the systems could be extended to perform scanning to resolve 3D scenes, this is out-with the scope of this Thesis, although work on a scanning time-of-flight photon-counting system is currently underway at Heriot-Watt.

6.6 Acknowledgements

I would like to express my thanks to Dr. Aongus McCarthy for his help during the measurements with the NbN SSPD and for braving the cold Scottish weather at 3 am. I would also like to thank Dr. Sae Woo Nam and Dr. Robert Hadfield for visiting Heriot-Watt with an SSPD from NIST and working with us on this experiment.

6.7 References

[1] M-C. Amann, T. Bosch, R. Myllyla and M. Rioux, *Laser ranging: a critical review of usual techniques for distance measurement*, Optical Engineering, **40** (1), 10 - 19 (2001)

[2] T. Bosch and M. Lescure, *Selected Papers on Laser Distance Measurement*, SPIE Milestone Series, Vol. MS 115, SPIE Optical Engineering Press, Bellingham, WA (1995)

[3] A.D. Marshall, R.R. Martin, and D. Hutber, *Automatic Inspection of Mechanical parts using geometric models and Laser Rangefinder data*, Image and Vision Computing, **9** (6), 385 - 405 (1991)

[4] D. Nitzan, A. E. Brain and R. O. Duda, *Measurement and use of registered reflectance and range data in scene analysis*, Proceedings of the IEEE, **65** (2), 206 - 220, (1977)

[5] Y. D. Chen and J. Ni, *Dynamic Calibration and Compensation of a 3-D Laser Radar Scanning System*, IEEE Transactions on Robotics and Automation, **9** (3), C652 - C658 (1993)

[6] W.C. Stone and M. Juberts, *Towards the ultimate construction site sensor,* NIST internal paper

[7] M. Bashkansky, H.R. Burrisb, E.E. Funkc, R. Mahond and C.I. Moorea, *RF phase-coded random-modulation LIDAR*, Optics Communications, **231** (1 - 6), 93 - 98 (2004)

[8] A.R. Slotwinski, F.E. Goodwin, and D.L. Simonson, *Utilizing AlGaAs laser diodes as a source for frequency modulated continuous wave (FMCW) coherent laser radars*, Proceedings SPIE, **1043**, 245 - 251 (1989)

[9] M. Herbert and E. Krotkov, *3D measurements from imaging laser radars: how good are they?*, Image and Vision Computing, **10**, 170 - 178 (1992)

[10] W. Ruff, K. Aliberti, J. Damman, M. Giza, P. Shen and B. Stann, *Performance of an FM/CW prototype LADAR using a 32-element linear self-mixing detector array*, Laser Radar Technology and applications 8, **5086**, 58 - 69 (2003)

[11] B. Augere and P.J. Cariou, *All-fibre 1.5μm CW coherent laser anemometer for in-flight measurements*, Laser Radar Technology and applications 8, **5086**, 121 - 128 (2003)

[12] C.J. Karlsson, F.Å.A. Olsson, D. Letalick and M. Harris, *All-fiber multifunction continuous-wave coherent laser radar at 1.55 mm for range, speed, vibration, and wind measurements*, Applied Optics, **39** (21), 3716 (2000)

[13] W.C. Swann and N.R. Newbury, *Frequency-resolved coherent lidar using a femtosecond fiber laser*, Optics Letters, **31** (6), 826 - 828 (2006)

[14] P.J. Besl, *Active, optical range imaging sensors,* Machine Vision and Applications, **1** (2), 127 - 152 (1988)

[15] Z. Ji and M.C. Leu, *Design of Optical Triangulation Devices*, Optics and Laser Technology, **21**, 335 - 338 (1989)

[16] http://www.impactstudiostv.com/laser_scan_site/htm/technology.htm (date accessed 01/08)

[17] V. Delaye, and P. Labeye, *High-resolution eye safe time of flight laser range finding*, Laser Radar Technology and Application Conference, **4035**, 216 - 225 (2000)

[18] http://www.mesa-imaging.ch/pdf/SR4000_Data_Sheet_rev1.1.pdf (date accessed 01/08)

[19] http://www.megaframe.eu/Contents/Publications/OtherPUBLIC/D2_1-v1_0public.pdf (date accessed 11/08)

[20] B. Aull, *3D imaging with Geiger-mode avalanche photodiodes*, Optics and Photonics News, May issue, 42 - 46 (2005)

[21] M.A. Albota, R.M. Heinrichs, D.G. Kocher, D.G. Fouche, B.E. Player, M.E. O'Brien, B.F. Aull, J.J. Zayhowski, J. Mooney, B.C. Willard, and R.R. Carlson, *Three-dimensional imaging laser radar with a photon-counting avalanche photodiode array and microchip laser*, Applied Optics, **41** (36), 7671 - 7678 (2002)

[22] M.A. Albota, B.F. Aull, D.G. Fouche, R.M. Heinrichs, D.G. Kocher, R.M. Marino, J.G. Mooney, N.R. Newbury, M.E. O'Brien, B.E. Player, B.C. Willard, and J.J. Zayhowski, *Three-Dimensional Imaging Laser Radars with Geiger-Mode Avalanche Photodiode Arrays*, Lincoln Laboratory Journal, **13** (2), 351 - 370 (2002)

[23] C. Ho, K.L. Albright, A.W. Bird, J. Bradley, D.E. Casperson, M. Hindman, W.C. Priedhorsky, R. Scarlett, R.C. Smith, J. Thieler and S.K. Wilson, *Demonstration of literal three-dimensional imaging,* Applied Optics **38** (9), 1833 - 1840 (1999)

[24] T. Maruyama, F. Narusawa, M. Kudo, M. Tanaka, Y. Saito, and A. Nomura, *Development of a near-infrared photon-counting system using an InGaAs avalanche photodiode*, Optical Engineering, **41** (2), 395 - 402 (2002)

[25] S. Verghese, J.P. Donnelly, E.K. Duerr, K.A. McIntosh, D.C. Chapman, C.J. Vineis, G.M. Smith, J.E. Funk, K.E. Jensen, P.I. Hopman, D.C. Shaver, B.F. Aull, J.C. Aversa, J.P. Frechette, J.B. Glettler, Z.L. Liau, J.M. Mahan, L.J.

Mahoney, K.M. Molvar, F.J. O'Donnell, D.C. Oakley, E.J. Ouellette, M.J. Renzi, and B.M. Tyrrell, *Arrays of InP-based Avalanche Photodiodes for Photon Counting*, IEEE Journal of selected topics in Quantum Electronics, **13** (4), 870 - 886 (2007)

[26] A.M. Wallace, G.S. Buller, A.C. Walker, J.S. Massa, and M. Umasuthan, *As easy as tcspc? Depth imaging and 3D metrology based on time-correlated single- photon counting*, Image Processing Europe, 232 - 235 (1998)

[27] A.M. Wallace, G.S. Buller, and A.C. Walker, *3D imaging and ranging by time-correlated single-photon counting*, Computing & Control Engineering Journal **12** (4), 157 - 168 (2001)

[28] J.S. Massa, A.M. Wallace, G.S. Buller, S.J. Fancey, and A.C. Walker, *Laser depth measurement based on time-correlated single-photon counting*, Optics Letters, **22** (8), 543 - 545 (1997)

[29] M. Umasuthan, A.M. Wallace, J.S. Massa, G.S. Buller, A.C. Walker, *Processing time-correlated single-photon counting data to acquire range images*, IEE Proceedings Vision, Image Signal processing, **145** (4), 237 - 243 (1998)

[30] G.S. Buller, R.D. Harkins, A. McCarthy, P.A. Hiskett, G.R. MacKinnon, G.R. Smith, R. Sung and A.M. Wallace, *A multiple wavelength time-of-flight sensor based on TCSPC,* Review of Scientific Instruments, **76** (8), 083112 (2005)

[31] I. Rech, I. Labanca, M. Ghioni, and S. Cova, *Modified single photon counting modules for optimal timing performance*, Review of Scientific Instruments, **77**, 033104 (2006)

[32] S.Cova, M.Ghioni, F.Zappa, *Circuit for high precision detection of the time of arrival of photons falling on single photon avalanche diodes*, US patent No. 6,384,663 B2, date May 7, 2002 (priority date March 9, 2000) European patent application n. 01200851.2-2217, filed March 6, 2001, Italian Patent MI2000 A 000467, filed March 9, 2000

[33] D.A. Gedcke, *How Histogramming and Counting Statistics Affect Peak Position Precision*, **AN58**, Ortec Application notes

[34] S. Richardson and P.J. Green, *On Bayesian analysis of mixtures with an unknown number of components*, Journal of the Royal Statistical Society: Series B, **59**, 731 - 792 (1997)

[35] S. Hernandez-Marin, A.M. Wallace and G.J. Gibson, *Markov chain Monte Carlo algorithms for 3D ranging and imaging*, IAPR Conf. on Machine Vision Applications (Tsukuba, May 2005)

[36] A.M. Wallace, R.C.W. Sung, G.S. Buller, R.D. Harkins, R.E. Warburton and R.A. Lamb, *Detecting and characterising return in a multi-spectral pulsed LaDAR system,* IEE Proceedings – Vision, Image and Signal Processing, **153** (2), 160 - 172 (2006)

[37] Robert A. Rohde, from http://en.wikipedia.org/wiki/Solar_radiation (date accessed 06/08)

[38] R.E. Warburton, A. McCarthy, A.M. Wallace, S. Hernandez–Marin, R.H. Hadfield, S.W. Nam, G.S. Buller, *Subcentimeter depth resolution using a single–photon counting time–of–flight laser ranging system at 1550 nm wavelength*, Optics Letters, **32** (15), 2266 - 2268 (2007)

[39] A. Verevkin, J. Zhang, R. Sobolewski, A. Lipatov, O. Gkhunev, G. Chulkova, A. Korneev, K. Simrov., G.N. Gol'tsman and A. Semenov, *Detection efficiency of large-active are NbN single-photon superconducting detectors in the ultraviolet to near-infrared*, Applied Physics Letters, **80** (25), 705 - 707 (2002)

[40] R.H. Hadfield, M.J. Steven, S.G. Gruber, A.J. Miller, R.E. Schwall, R.P. Mirin, and S.W. Nam, *Single photon source characterization with a superconducting single photon detector*, Optics Express, **13** (26), 10846 - 10853 (2005)

Chapter 7 - Conclusions & Future Work

Due to the significant increase in interest in single-photon counting over the past few years, the demand for highly efficient and low noise detectors has presented itself for numerous applications. As explained in the review of single-photon detectors, Si SPADs are currently the highest performance devices for the visible wavelength range with SPDE up to 70 %, low DCRs, capable of high maximum count rate (~ Mcs^{-1}), and room temperature operation.

Many emerging technologies are aimed at extending photon counting into the infrared – devices that rely on the capture of a photon by a quantum dot, bolometers and superconducting nanowires. Whilst these devices offer excellent performance in many of the key characterisation parameters, most of them must be operated at temperatures of 4 K or below. This temperature requirement may be acceptable in a laboratory environment, but in optical data network systems or field-based instruments their integration may be somewhat more difficult. InGaAs/InP SPADs offer the opportunity to work at temperatures reachable by two-stage thermo-electric peltier coolers.

In this Thesis, InGaAs/InP SPADs have been described and previous work on their electric field modelling and growth was presented. The custom made SPADs fabricated in conjunction with the University of Sheffield have been fully characterised in terms of the key figures of merit for single photon detectors. Two different designs were compared – SPAD 1Q and SPAD 3Q. SPAD 1Q had a graded region consisting of one InGaAsP quaternary with an exactly intermediate bandgap between the InGaAs and InP layers. Secondly, SPAD-3Q which had a graded region composed of three sublayers of stepped bandgap. It was noted that the DCR of SPAD 1Q was far lower than that of SPAD 3Q, which is desirable. However, the same was also true of the SPDE, especially at low temperatures. This was due to the larger valence band discontinuity faced by a primary hole (photo-generated or otherwise) when entering the multiplication region. At low temperatures, the hole has less thermal energy and is thus further inhibited. In SPAD 3Q, however, the stepped barrier results in a higher probability of the primary hole entering the multiplication region. Whilst this results in a higher DCR at low temperatures compared to SPAD 1Q, there is also a significant increase in SPDE. Overall, this results in SPAD 3Q having a lower NEP than SPAD 1Q and is hence a more sensitive device. SPAD 3Q presented a SPDE of ~ 10 % which was comparable

to the best linear multiplication APD (from a rigorous selection program) operated in Geiger mode – Epitaxx EPM 239AA.

Photon arrival timing jitter was measured for SPAD 3Q devices of varying active area diameter (10, 20 & 40 μm). It was found that doubling the active window diameter approximately doubled the photon timing jitter. This is mainly due to the time taken for the avalanche to spread across the entire active area. This process increases the jitter of the device as the active area increases. Overall, the jitter decreased with increasing excess bias with the fastest being ~ 200 ps.

In parallel with the custom-made SPADs, Princeton Lightwave Inc. SPADs were also characterised. They yielded excellent SPDE of ~ 30 % and sub 100 ps jitter. The reasons for the significantly higher performance are numerous, but are likely to relate to the growth and post-growth fabrication.

The afterpulsing phenomenon was described and methods of its characterisation discussed. The time-correlated carrier counting method (TCCCM) was chosen as the most sensitive method to fully investigate the afterpulsing phenomenon. Studies on SPAD 3Q, an Epitaxx APD and a test structure (InP only device) all yielded activation energies of ~ 250 meV. This pointed to the InP multiplication region as the source of the trapping. Two Princeton Lightwave Inc. InGaAs/InP SPADs were tested in the same manner and also gave activation energies in the region of ~ 250 meV. The exact cause of this trap level has not been identified, although there are reported hole and electron traps in InP caused by Zn diffusion at energy levels close to that found in this Thesis.

Methods of reducing the afterpulsing probability as reported in the literature were described. Most of these involved using short gates (< 1 ns) to limit the current passing through the device since the afterpulsing probability is directly linked to the amount of charge that passes through the device per event. One method relied on using a sub-bandgap laser to photo-ionise trapped carriers. The short gate methods are suitable for applications that require fast, repetitive gating such as QKD.

The Author, however, was more interested in looking at ways in which a SPAD could be used with longer gates, or not gated at all. For this reason, sub-Geiger mode was investigated. In sub-Geiger mode, the device is DC biased *below* breakdown such that it is always ready to detect a photon (the actual DC bias ranged from 99.5 % of the breakdown voltage to 99.95 % when an R_S of 10 kΩ was used). Below breakdown, the

device acts more like a linear multiplication device and has a gain of typically 10^6. The lower voltage applied to the device, and the smaller amplitude of the output greatly limited the charge passing through the SPAD, hence reducing the afterpulsing probability. With an R_S of 10 kΩ the SPDE was ~ 1 % at all temperatures. The DCR, however, was significantly lower which meant that at temperatures less than 190 K, working in sub-Geiger mode results in a more sensitive device compared to the same device in Geiger mode. This method resulted in an InGaAs/InP SPAD being used in free-running sub-Geiger mode at room temperature (290 K) with negligible effects of afterpulsing, which, to the best of the Author's knowledge, has never been accomplished before.

The effects of R_S on sub-Geiger operation were studied and it was found that using an R_S of 100 kΩ led to an increased SPDE since the output pulse suffered less from the effects of electrical noise. Using an R_S of 1 MΩ led to detection efficiencies greater than 2.5 % since a higher bias could be placed upon the device before a prohibitively high DCR was observed. The higher bias also resulted in a lower photon-timing jitter at FWHM, down to ~ 500 ps. The penalty of increasing R_S is that this affects the reset time of the device due to the R_SC time constant. With an R_S of 100 kΩ, a maximum count rate of over 4 Mc/s was achievable, yet when an R_S of 1 MΩ was used, the count rate saturated at ~ 400 kc/s.

Finally, time-of-flight laser ranging using time-correlated single-photon counting was investigated. A brief review of alternative ranging methods was presented followed by work conducted by the Author on a multi-wavelength photon counting ranging system. The depth resolution of the system was measured at $\lambda = 630$ nm, firstly with a standard Si SPAD, and secondly with a modified Si SPAD (lower jitter). The depth resolution improved with the reduced jitter of the modified SPAD. Subsequently, a superconducting NbN nanowire single photon detector was employed as the detector in the same system. Since these detectors are sensitive to $\lambda > 2$ μm, a 1550 nm wavelength laser was used as the source. The superconducting detector's lower jitter resulted in a surface to surface depth resolution of 4 mm being measured at a stand-off distance of 330 m.

Future work on InGaAs/InP SPADs will include more work in sub-Geiger mode to fully exploit this novel technique. A possibility for investigation is that of using a Ge SPAD in sub-Geiger mode: at room temperature Ge absorbs at 1550 nm but when cooled (which was necessary to reduce the DCR to a manageable level) the cut-off is a little

below 1500 nm. Therefore, in sub-Geiger mode, it may be possible to only cool the device slightly, such that it still absorbs at 1550 nm whilst limiting the DCR enough for photon counting operation. Alternatively, Ge SPADs may present a higher SPDE for a wavelength of 1310 nm than an InGaAs/InP if sub-Geiger mode does not reduce the DCR significantly at higher temperatures for 1550 nm wavelength operation.

Recently, a new project with the European Space Agency and the University of Sheffield has started in which we have modelled (two-dimensional electric field profiling) new SPAD designs in narrower-gap semiconductors, such as InAs, for use in single-photon counting operation at $\lambda > 2$ μm for gas detection in the atmosphere measured from a satellite. The samples are currently being grown by the University of Sheffield and will soon be tested at Heriot-Watt University.

Other future work on long wavelength single-photon detectors will include work with Ge fusion bonded to Si. We have already demonstrated that the bonding process works (in conjunction with the Scottish Microelectronics Centre, part of Edinburgh University) and provides an excellent ohmic contact between the two bonded wafers. The next steps involve designing a suitable device structure so that absorption takes place in the Ge and multiplication takes place in the Si. This structure would take advantage of Ge's narrow-gap for long wavelength photons and Si's multiplication properties (relatively few trapping centres).

Research into TOF laser ranging is ongoing. Currently, a scanning TOF is being developed using a similar technique to that reported in this Thesis. The scanning is accomplished using galvanometer driven mirrors to project a laser beam on to a scene, the scene is then reconstructed using software. This process could also be adopted for longer wavelengths and may include the use of an InGaAs/InP SPAD operated in sub-Geiger mode as the detector.